Resolving the gas distribution and kinematics in the inner regions of protoplanetary disks

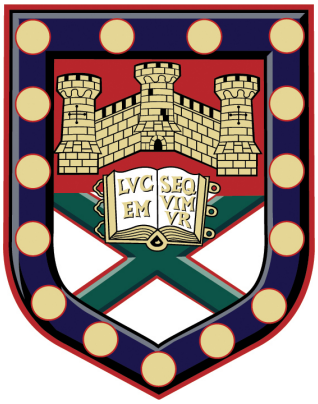

Submitted by Edward Hone to the University of Exeter as a thesis for the degree of Doctor of Philosophy in Physics, September 2019.

Abstract

Star formation can be characterised by the presence of accretion disks and outflows that originate from the inner regions of these disks. Despite playing a crucial role in the star formation process, the mechanism by which jets are formed is unknown. The jets appear to originate from the very inner regions of protoplanetary disks, making it difficult to observe the jet-launching region by conventional means. In order to achieve the high-angular resolution required to observe the inner disk it is necessary to observe with optical interferometry. In this thesis I aim to answer the question of how astrophysical jets and winds are launched from the inner regions of circumstellar disks by observing with spectrally dispersed interferometry in the near-infrared wavelength regime.

In this thesis I present near-infrared, K-band VLTI/AMBER and VLT/CRIRES observations of the Herbig B[e] star MWC297. I interpret velocity-resolved images across the Brγ line, as well as the derived two-dimensional photocentre displacement vectors, and fit kinematic models to our visibility and phase data in order to constrain the gas velocity field on sub-AU scales. The velocity-resolved channel maps and moment maps reveal the motion of the Brγ-emitting gas in six velocity channels, marking the first time that kinematic effects in the sub-AU inner regions of a protoplanetary disk could be directly imaged. The Brγ photocentre shifts trace a rotation-dominated velocity field, where the blue- and red-shifted emissions are displaced along a position angle of $24^\circ \pm 3^\circ$ and the approaching part of the disk is offset west of the star. The visibility drop in the line as well as the strong non-zero phase signals are modeled using a disk-wind model with a poloidal velocity of $\sim$20kms^{-1}. Simulations show that adding a poloidal velocity component causes the perceived system axis to shift, offering a powerful new diagnostic for the detection of non-Keplerian velocity fields.

In addition to the K-band data, I present analysis of AMBER spectro-interferometric data for MWC297 in the H-band, spectrally and spatially resolving multiple different Brackett series lines. I use the differential phase data to construct photocentre displacement vectors for each of the Brackett series lines, which show that all the lines in the H-band trace a similar velocity field. I construct a global kinematic model for the whole H-band, with the results showing that the H-band Brackett series lines originate from a compact disk wind region, with a poloidal velocity of $\sim$220kms^{-1}.

I also present AMBER and CHARA interferometry data along with CRIRES spectroscopy data ($R = 100\,000$) of the Herbig Be star MWC147. The continuum emission is fitted with an inclined Gaussian and a ring with a radius of 0.60 mas (0.39 au), which is well within the expected dust sublimation radius of 1.52 au. No significant change is detected in the measured visibilities across the Brγ line, indicating that the line-emitting gas is located in the same region as the continuum-emitting disk. The differential phase data is used to construct photocentre displacement vectors across the Brγ line, revealing a velocity profile consistent

with a rotating disk. The AMBER spectro-interferometry data is fitted with a kinematic model of a disk in Keplerian rotation, where both the line-emitting and continuum-emitting components of the disk originate from the same compact region close to the central star. The presence of line-emitting gas in the same region as the K-band continuum supports the interpretation that the K-band continuum traces an optically thick gas disk.

I present spectro-interferometric observations of the Brγ emission from the the T Tauri star CW Tau. I construct photocentre shifts from the GRAVITY differential phase data, which indicate motion along a PA of 120.5° which is close to the previously observed jet axis for this object. This suggests that the velocity field traced by the Brγ emission of CW Tau traces a high-velocity outflow close to the radius where the disk is truncated by the stellar magnetic field.

Each of the individual studies in this work introduces a new insight into the jet-launching region of young stellar objects. I use observations with high-spatial and high-spectral resolution to place strong physical constraints on the morphology and velocity fields of the jet-launching regions in young stars. The technical achievements presented in this thesis demonstrate the effectiveness of spectro-interferometry as a tool for studying the dynamic physical processes associated with star formation.

Contents

List of Figures

List of Tables

Declaration

All of the work presented in this thesis was undertaken as a candidate for a research degree at the University of Exeter. Contributions by other authors have been clearly indicated when used. All original authors of illustrations have been credited. Where the work of other authors is quoted, the source has been attributed. Aside from these external contributions, this thesis is entirely my own original work.
Chapter 6 contains work published in Hone et al. (2017). Chapter 8 contains work published in Hone et al. (2019). Chapters 7 and 9 contain work soon to be published in individual papers with myself as the first author.

Acknowledgements

I would like to acknowledge the support of my supervisor Stefan Kraus, and thank him for fostering my ambition and encouraging me to keep raising the bar in the pursuit of scientific excellence. Thank you to my research colleagues and friends at the University of Exeter, Matt Willson, Jacques Kluska, Alex Kreplin, Claire Davies, Aaron Labdon and Sebastian Zarrilli.

I acknowledge support from a Marie Sklodowska-Curie CIG grant (Ref. 618910) and an ERC Starting Grant (Grant Agreement No. 639889). I wish to thank the College of Engineering, Mathematics and Physics at the University of Exeter for providing me the opportunity to study for this PhD. I thank Larisa Tambovtseva and Vladimir Grinin for helpful discussions regarding the modeling of disk winds, and Karl-Heinz Hofmann and Gerd Weigelt for the collaboration on image reconstruction. I count myself very blessed to have been able to visit Cerro Paranal to use the VLTI, and would like to thank ESO for making this unforgettable opportunity posssible.

I would like to thank my parents, who have been a constant source of support and inspiration throughout my life and particularly the last four years. Thank you to my brother Joe for blazing this trail for me, and to Tom, Nick and Sam who walked it with me. I would finally like to thank my wonderful fiancée Charlotte, who has consistently gone above and beyond in her support of me throughout the duration of my PhD. This achievement would simply not have been possible without her.

Chapter 1

Introduction

Throughout the history of science, the greatest motivation for scientists has surely been the question of our origins, whether that be the origins of life or the origins of our world. In attempting to answer this question, scientists have made discoveries ranging from the mundane to the extraordinary, leading to a greater understanding of our place within the larger cosmos. The night sky has been the subject of the most culturally significant tales and mythology for millenia, with every civilisation around the world prescribing meaning to the shapes and motions of the stars, planets and even the dust lanes in the Milky Way. In some ancient societies this superstition was accepted along with a basic scientific approach to measuring the motions of the stars, as they allowed people to measure the periodic changes in the seasons and were a useful predictive tool for agricultural purposes. Throughout the early history of astronomy, all models of the universe placed the Earth at the centre, with the Sun, Moon, and other known celestial objects orbiting the Earth inside a celestial sphere. This view was unchallenged until the early 1500s when Nicolaus Copernicus published his *Commentariolus* and later, in 1543, *De revolutionibus orbium coelestium (On the revolutions of the holy spheres)*, in which he laid out the fundamental aspects of his heliocentric model of the universe. In this model several postulates were laid out, including that:

- the Earth is at the centre of the lunar sphere (i.e. the Moon orbits the Earth)
- all the spheres rotate around the Sun
- the stars are stationary and their motion is caused by the rotation of the Earth.

This theory successfully predicted observations such as the retrograde motions of the planets as well as the seasonal migration of the Sun, offering a much simpler explanation

Figure 1.0.1: Image of HH24 jet taken by the Hubble Space Telescope. This image was taken from the Hubble Legacy Archive (available at `http://hla.stsci.edu/`).

than had previously been put forward.

In 1610 Galileo Galilei first used a telescope to scientifically observe the night sky, effectively giving birth to modern observational astronomy. Galileo observed Jupiter and detected what appeared to be three fixed stars, so faint as to be almost invisible, that extended from the centre of Jupiter along the same axis. Galileo continued to observe Jupiter and the tiny stars on subsequent nights, and observed that they moved along the same axis towards and away from Jupiter, even disappearing at times behind the planet. Galileo concluded that the objects were orbiting Jupiter, and had discovered three of the four most massive Jovian moons, discovering the fourth a few days later. The discovery of celestial objects orbiting one another was another point in favour of the Copernican model of the universe, demonstrating how observations and theory combine to expand our collective understanding of astrophysics.

The history of the Universe is recorded in the lives of stars but many unanswered questions remain regarding their formation and evolution. It is not possible to observe the star formation process from start to finish as it can take millions of years (depending on

the mass of the stars). By observing objects that are at different stages of star formation, glimpses can be gained of the mechanisms that are are work and a greater understanding of the underlying physics can be built.

Observations of star forming regions have revealed the presence of spectacular jets launched from a significant fraction of young stars (such as is shown for HH24 in Figure 1.0.1), indicating that the star formation process is associated with outflow as well as the infall of matter during gravitational collapse (Frank et al., 2014). These jets extend to large distances and influence the surrounding interstellar medium (Reipurth, 1997), but the mechanism by which they are launched and accelerated is unknown. Answering the question of how these jets are formed presents a major technical challenge, as the launching region is far too compact to be resolved with convential astronomical observations.

In this thesis I aim to answer the question of how the astrophysical jets from young stars are formed. To do this I use spectrally-dispersed interferometry at near-infrared wavelengths to spatially and spectrally resolve the jet-launching region around several young stellar objects, ranging in mass and luminosity. I focus mainly on the Brγ line in the near-infrared K-band, which has been shown in models to predominantly trace hot gas that is being launched at the base of protostellar jets (Tambovtseva et al., 2016). The differential visibilities and phases measured with the VLT Interferometer and its instruments AMBER and GRAVITY are interpreted with a suite of analysis tools. These range from modelling the wavelength dependent size of the jet-launching region to model-independent photocentre shifts which trace to the wavelength dependent location of the line-emitting gas. With this information I construct kinematic models to find the best physical description of the jet/wind-launching region in each of the target objects. With the results obtained for different objects I attempt to provide insights into how jets are launched from young stars along with the role that they play in the star formation process.

Chapter 2

Star formation

2.1 General paradigm

The formation of stars is one of the richest areas of research in the fields of observational and theoretical astrophysics. Studying the formation of stars within our galaxy helps us to understand how our own solar system formed, granting us the opportunity to address the fundamental questions about our origins. Whilst the finer details of the star formation process are not yet fully understood, the fundamental processes are outlined in the seminal work of Shu et al. (1987).

Star formation begins in giant molecular clouds (GMCs) in the interstellar medium, largely comprised of remnants of supernovae and planetary nebulae comprised primarily of molecular hydrogen (H_2), Helium and simple molecules such as CN and HCO^+ (Bergin et al., 1997). Whilst Helium makes up a significant proportion of the ISM, it is inert and does not play a role in the star formation process. These molecular clouds have masses of up to $\sim 10^7 M_\odot$ and range in size up to a few hundred parsecs (Murray, 2011). Self-gravitational collapse occurs within the GMCs and as the cloud collapses filamentary structures are formed, such as those shown in the simulations of Bate et al. (2003). As the cloud further contracts the Jeans instability (Jeans, 1902) gives rise to fragmentation within the molecular cloud, leading to the formation of smaller clouds until individual protostellar cores remain.

During the collapse from GMCs to protostellar cores the conservation of angular momentum, along with the small density pertubations present in the initial cloud, causes the cloud and subsequent cores to rotate faster as they collapse. Bodenheimer (1995) suggested that the origin of the angular momentum could be a combination of galactic differential rotation, random interstellar cloud motion, fragmentation along with interac-

tions with the galactic magnetic field. In the centre of the individual protostellar cores the rotating gas and dust settles to form a protoplanetary disk which orbits a central protostar which is held in hydrostatic equilibrium. As the system evolves, the disk and surrounding envelope act as mass reservoirs feeding accreting material onto the central young stellar object (YSO), which eventually achieves temperatures and pressures high enough to ignite nuclear fusion, becoming a main sequence star.

2.1.1 Giant molecular clouds

Star formation is a constant ongoing process within the Milky Way, with the majority taking place within giant molecular cloud complexes (GMCs). In contrast to the rest of the interstellar medium (ISM), which is mainly comprised of ionised gas and cosmic rays, GMCs are composed mainly of molecular Hydrogen (H_2) and simple molecules such as CN and HCO^+ (Bergin et al., 1997). Estimates of GMC lifetimes based on observations suggest they exist for timescales on the order of 10^7 years before they are dispersed by a combination of shear, becoming unbound and stellar feedback (Blitz and Shu, 1980; Kawamura et al., 2009; Miura et al., 2012; Dobbs and Pringle, 2013).
Turbulence within the cloud is induced via interactions with local objects (such as other molecular clouds and supernova shockwaves), which leads to perturbations in the cloud density that go on to cause gravitational instabilities, such as the Jeans instability (Jeans, 1902). This instability can be shown by considering a stable cloud, where the thermal energy of the cloud is given by,

$$E_{\text{thermal}} = \frac{M}{m} \times \frac{3}{2} k_B T, \tag{2.1.1}$$

where we assume that the cloud is an ideal gas and M is the mass of the cloud, m is the mass of constituent molecules and T is the temperature. This can be related to the gravitational potential energy of the cloud,

$$U_{\text{grav}} = -\alpha \frac{GM^2}{R}, \tag{2.1.2}$$

(where R is the cloud radius and α is a scalar that varies based on the radial density profile of the cloud) via the virial theorem,

$$E = -\frac{1}{2} U. \tag{2.1.3}$$

Assuming a stable cloud of density ρ, where mass M is given by $M = \frac{4}{3}\pi R^3 \rho$, this expression can be rearranged to give us the Jeans radius R_J,

$$R_J = (\frac{9k_BT}{4\alpha Gm\pi\rho})^{\frac{1}{2}}, \tag{2.1.4}$$

which is the minimum radius for a stable cloud of density ρ and the Jeans Mass M_J,

$$M_J = (\frac{3}{4\pi\rho})^{\frac{1}{2}} \times (\frac{3k_BT}{\alpha Gm})^{\frac{3}{2}}, \tag{2.1.5}$$

the maximum Mass for a stable cloud of density ρ. We can see that $M_J \propto \rho^{-\frac{1}{2}}$, so as the cloud collapses and the density increases, the Jeans Mass M_J decreases. This means that the cloud becomes unstable as it collapses under self gravity and fragments into smaller clouds until the fragmentation is stopped when the temperature starts to rise, which causes the Jeans Mass to rise again ($M_J \propto T^{\frac{3}{2}}$). The result of the fragmentation is a cluster of protostellar cores, each of which goes on to form its own star systems.

2.1.2 Protostellar cores

The individual protostellar cores continue to undergo adiabatic gravitational collapse until the density has increased to the point that the cloud is optically thick. When it reaches this point, the cloud can reabsorb its own thermal radiation which leads to the formation of a hydrostatic core, with a radius of $\sim$ 4au (Larson, 1969). This leads to a period of rapid heating where the increased thermal pressure is able to offset the gravitational collapse. Outside of the core, material continues to collapse and the mass continues to increase until the temperature reaches $\sim$2000K, causing the molecular hydrogen to dissociate into its optically thin atomic form. The atomic Hydrogen is no longer able to provide the thermal pressure to support the core leading to a second rapid collapse or the core to form a protostar.

The gravitational contraction acts as an energy source for the young protostar, with $\sim$50% of the energy going to internally heating the protostar and the other $\sim$50% radiated out as photons. This process, known as the Kelvin-Helmholtz mechanism, occurs over a timescale τ_{KH} that is defined as,

$$\tau_{KH} \propto \frac{M^2}{RL}, \tag{2.1.6}$$

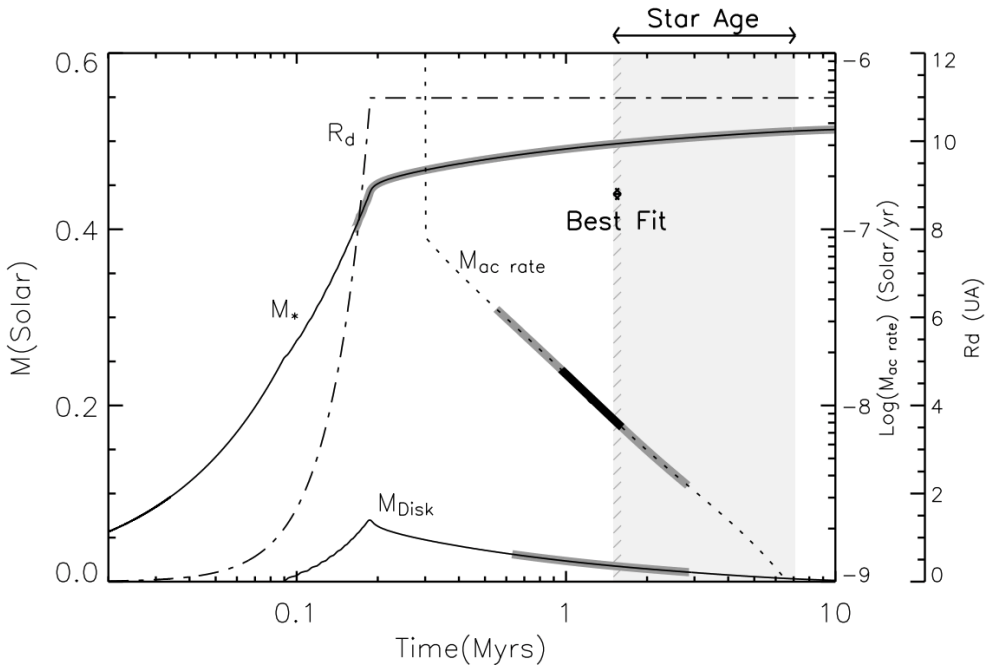

Figure 2.2.1: Figure from Hueso and Guillot (2005) showing the evolution of the stellar mass ($M_\star$, solid line), disk mass ($M_{\rm Disk}$, solid line), mass accretion rate ($M_{\rm ac\ rate}$, dotted line) and centrifugal radius ($R_{\rm d}$, dotted-dashed line) with time.

where $\frac{M^2}{R}$ is the gravitational binding energy and L is the stellar luminosity. The gravitational heating causes the core of the protostar to heat up to temperatures exceeding $\sim 10^7$K. At these temperatures the nuclear fusion mechanisms begin to occur in the stellar core, causing a pressure that offsets the gravitational collapse leading to a new state of hydrostatic and thermal equilibrium. At this point the young star has reached the main sequence.

2.2 Protoplanetary disks

The majority of molecular clouds that have been observed exhibit some rotation (Goodman et al., 1993) which is consistent with the effects of the turbulence discussed above in Section 2.1.1. Whilst the rotational velocity of the cloud is low, the total angular momentum of the cloud is far greater than can be contained within the stars that will eventually form from the cloud, even if all the stars are rotating at their critical velocity. This discrepancy shows the need for a mechanism that allows protostellar material to shed its angular momentum before it eventually forms a star. During the lifetime of a GMC it is suggested that large scale magnetic fields can remove some of the angular momentum via

magnetic braking (Mouschovias, 1977, 1991). However, even the angular momentum of the hydrostatic core is too great to be contained within a single star and magnetic braking cannot play a role here as the magnetic field is decoupled from the gas in the later stages of star formation (Larson, 2003). The formation of binary or higher-order star systems helps to mitigate this problem (as well as accounting for the high numbers of binary stars observed) but the angular momentum problem is still an obstacle that must be overcome for each individual star.

The main mechanisms by which young stellar objects shed angular momentum is via their protoplanetary disks. These disks can form as the centrifugal force associated with the rotation counteracts the gravitational collapse, but this only occurs in the radial direction, normal to the rotation axis (Terebey et al., 1984). The disk system reaches orbital and hydrostatic equilibrium, with the centrifugal force balancing the gravitational collapse in the radial direction and the gravitational force towards the disk mid plane being countered by pressure (Yorke et al., 1995). Viscous stresses and gravitational torques within the disk transport angular momentum radially outwards away from the star, the result of which is that the majority of the circumstellar material falls towards the star whilst a small amount moves outwards and absorbs the angular momentum (Lynden-Bell and Pringle, 1974; Dullemond et al., 2007). As matter is transported from the outer envelope onto the disk the disk spreads out before it is eventually stopped by processes such as photoevaporation or interactions with local stars (Scally and Clarke, 2001), achieving an outer radius on the order of 100au (Adams et al., 1987,9; Beckwith et al., 1990; Nakamoto and Nakagawa, 1994; Hueso and Guillot, 2005). The disk undergoes a period of collapse, lasting for $\sim 2 \times 10^5$yr, during which there is rapid accretion from the disk ($10^{-5} - 10^{-6} M_{\odot}\text{yr}^{-1}$; Hueso and Guillot, 2005) onto the central star, before falling to the much lower level of $10^{-7} - 10^{-9} M_{\odot}\text{yr}^{-1}$ once the collapse has finished (see Figure 2.2.1). Observations of FUor and EXOr stars suggest that accretion is episodic in nature and does not drop off steadily (Audard et al., 2014).

The source of the viscosity that leads to the mass infall is still an open question, as the intrinsic viscosity of the circumstellar matter is not sufficient to explain the accretion rates that are observed. Turbulence and the effects of magnetic fields within the disk can however act in the same way as viscosity, particularly the magnetorotational instability (MRI) which can drive turbulence in disks and can help to transport angular momentum outwards (Balbus and Hawley, 1991). This process occurs in weakly magnetised disks, even in a region where the ionisation fraction is low. Additional mechanisms for angular momentum removal such as the convective instability and gravitational instability are

discussed and contextualised in the review of Gammie and Johnson (2005). Other global phenomena such as spiral density waves (Zhu et al., 2015; Kratter and Lodato, 2016) and magnetohydrodynamic (MHD) driven winds (Blandford and Payne, 1982) can also be invoked as less significant methods for angular momentum transport away from the disk..

2.2.1 Disk structure and composition

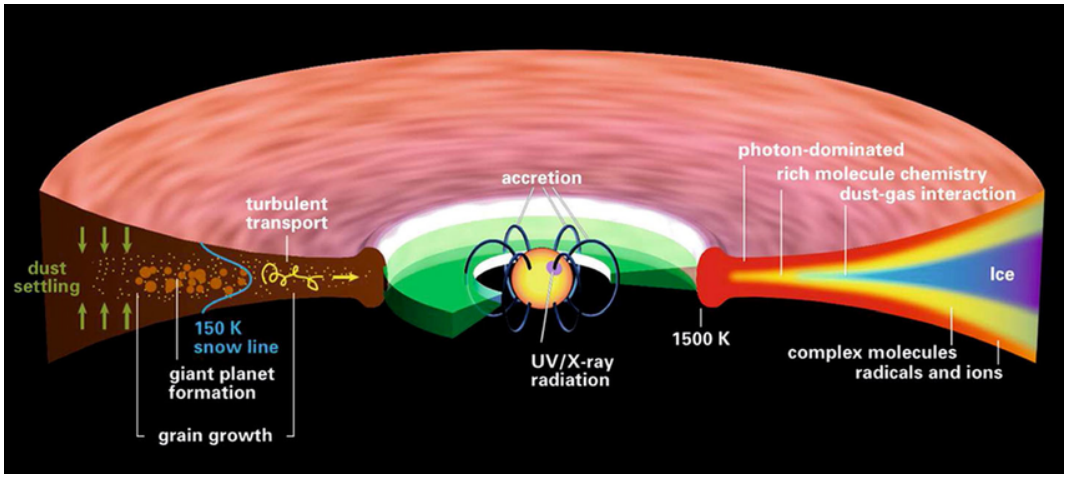

Figure 2.2.2: Figure from Henning and Semenov (2013) showing the chemical composition of the disk at $\sim 1-5$Myr around a $1M_{\odot}$ star, highlighting dust grains, complex molecules and ices.

Protoplanetary disks contain all of the necessary raw materials needed to build a solar system, with all the variety and complexity that that entails. Whilst the majority of the ISM is made up of Hydrogen and Helium, heavier elements and more complex molecules are also present and survive through to the protoplanetary disk phase. Disks themselves play a role in the formation of complex molecules, with dust grains acting as catalysts for the formation of complex and organic molecules (Hill and Nuth, 2003; Henning and Semenov, 2013). Additionally, the radial temperature structure within disks allows for the different molecules to freeze out at different radii, forming snow or ice lines (Morbidelli et al., 2000). Figure 2.2.2 illustrates the basic structure of a disk with particular references to its astrochemical composition.

Identifying the presence of a disk around a star can be achieved by observing infra-red excess in the star's spectral energy distribution or SED (Lada, 1987). This diagnostic is a useful means to classify the presence of circumstellar material in young stellar objects with strong infra-red excesses (see Figure 2.2.3) but has limitations when used to infer

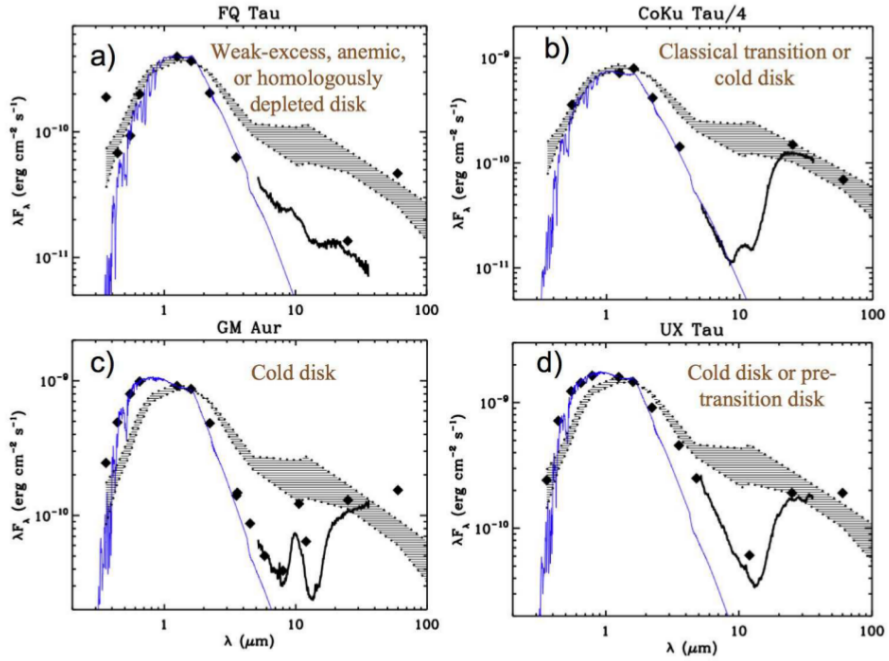

Figure 2.2.3: Figure from Williams and Cieza (2011) showing how the SED of a disk varies for different disk structures.

information about the structure of that material. Kenyon and Hartmann (1987) first suggested the presence of flared disks to explain the strong IR excess that they observed with IRAS, a phenomenon that was confirmed via direct imaging of disks with the Hubble space telescope (Burrows et al., 1996; Padgett et al., 1999; Smith et al., 2005). The density of a disk in hydrostatic equilibrium (assuming azimuthal symmetry) is a function of both radius R and vertical height Z, defined as:

$$\rho(R,Z) = \frac{\Sigma(R)}{\sqrt{2\pi}H} \exp\left(-\frac{Z^2}{2H^2}\right) \tag{2.2.1}$$

where $\Sigma(R)$ is the disk surface density and $H(R)$ is the scale height which is dependent on the balance between the thermal pressure and gravity in the Z direction, assuming self-gravity and rotation (Williams and Cieza, 2011). Chiang and Goldreich (1997) found an approximate power-law dependence of the disk flaring by considering the heat exchange between the star and disk interitor via the heated surface layers of the disk, finding that $H \propto R^h$ where $h \sim 1.3-1.5$. However, observations of disk SEDs exhibit less mid infra-red flux than would be expected for a disk with this degree of flaring, explained by the settling of dust to the disk mid-plane, with the upper layers of the disk being purely comprised of gas (Chiang et al., 2001, see Figure 2.2.2).

The introduction of ALMA opened up the opportunity to directly image protoplane-

tary disks with unprecendented angular resolution in the millimetre and submillimetre regimes. The initial results from ALMA (ALMA Partnership et al., 2015) focussed on imaging the disk around the T Tauri star HL Tau, revealing the presence of multiple gaps traced in the sub-mm continuum. Examples of objects with disks exhibiting a similar gap structure include Elias 2-24 (Cieza et al., 2017), TW Hya (Huang et al., 2018), AS 209 (Fedele et al., 2018) along with several other objects that were part of a large survey by Long et al. (2018). The presence of gaps due to planet formation was already a well established aspect of the star formation paradigm but presentation of the new ALMA data influenced many theorists to construct novel models to complement the ALMA observations. Dipierro et al. (2015) constructed a disk model with three embedded, accreting protoplanets within the disk, and found that their models made a good match to the ALMA data. Dipierro et al. discussed that the spiral density waves launched by the protoplanets in their simulations affected different sized dust grains in different ways with millimetre sized grains being influenced the most, therefore creating the biggest gaps. Van der Marel (2018) explored the possibility that the increased grain growth expected at a snow line could be the mechanism behind the dusty rings observed in the millimetre continuum. An example of an alternative mechanism for the clearing of gaps in a disk was proposed by Lorén-Aguilar and Bate (2015), namely the presence of toroidal vortices that gather the dust into rings which are observable in the continuum and scattered light, but such processes require further modelling to test their significance. ALMA has also been used to reveal the presence of large asymmetric dust traps in protoplanetary disks, such as in the work of van der Marel et al. (2013). It is theorised that such dust traps can overcome the inward drift of dust particles that occurs during planet formation.

2.3 YSO classifications

YSOs can be identified and classified by observing their SEDs, which are a useful tool to study the structure and physical properties of young stars and the circumstellar material associated with them. Protostars are classified from Class 0 to Class III based on their bolometric temperature, the temperature of a black body with the same mean frequency as the target object (Myers and Ladd, 1993), defined as,

$$T_{\rm bol} = 1.25 \times 10^{-11} \overline{\nu}\ {\rm K\ Hz^{-1}} \tag{2.3.1}$$

where $\overline{\nu}$ is the mean frequency. Class 0 objects are young protostars that are still contracting adiabatically, with SEDs that are characterised by extremely weak emission in

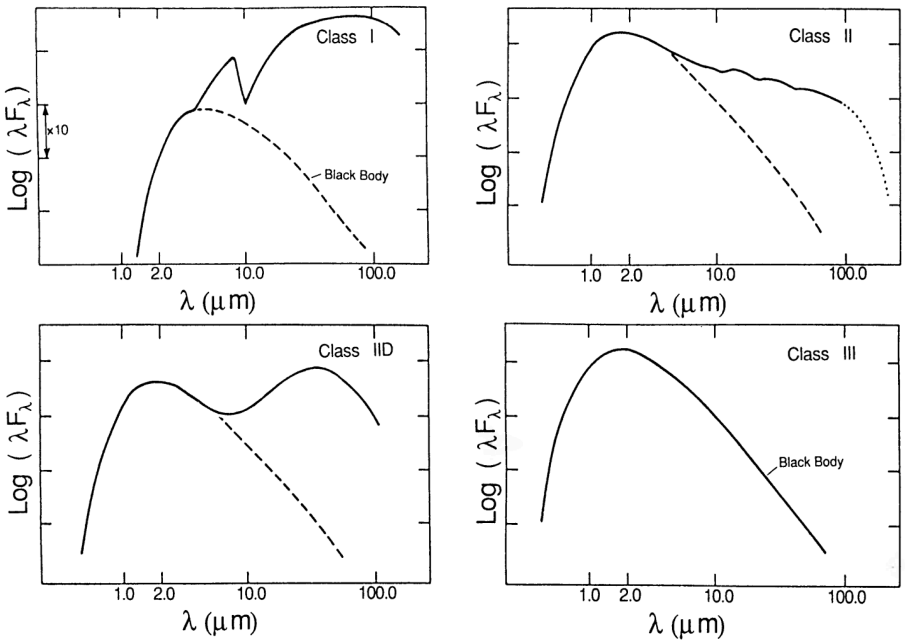

Figure 2.3.1: Figure adapted from Wilking (1989) showing how the SED of a protostar varies as it evolves through different classification states.

optical and near infra-red with most of their emitted radiation in the submillimetre regime (Barsony, 1994; Enoch et al., 2011). Class I objects have undergone the core collapse to form a circumstellar disk and envelope, and are still very weak at optical wavelengths with SEDs that peak in the mid- to far-infrared (Muzerolle et al., 1998a; Watson et al., 2004). Class II protostars are classical T Tauri stars which host significant circumstellar disks, with spectra that are dominated by UV and IR excess, strong emission lines and detectable emission at optical wavelengths (Adams et al., 1987; Hartmann et al., 1998). For these objects the angle at which they are viewed strongly influences the shape of the overall SED, as different parts of the star and disk are revealed and obscured at different viewing angles. Class III objects exhibit fewer emission lines as well as a weaker IR-excess than their Class II counterparts. These objects are no longer actively accreting matter, and have thin debris disks that produce a similar SED no matter what angle they are viewed at. The SEDs for different protostellar classes are shown in Figure 2.3.1.
In addition to characterising YSOs due to their SED, it is also useful to characterise them based on their more detailed spectral signatures. Herbig (1962) first outlined the observational spectroscopic criteria that describe T Tauri stars as follows:

1. The presence of Hydrogen and Ca II lines in emission.
2. The presence of fluorescent Fe I emission lines at 4063Å and 4132Å

3. The [S II] emission lines at 4068Å and 4076Å are usually present, [S II] lines at 6717Å and 6731Å along with [O I] line at 6300Å are probably characteristic as well
4. Presence of strong Li I absorption at 6707Å

Additionally, Herbig stated that the lines should be superimposed on a continuous spectrum ranging from featureless to the absorption spectrum of a star with a spectral type of late F, G, K or early M. This definition was later revisited by Bastian et al. (1983), who suggested altering the definition of T Tauri stars to a purely phenomenological form as follows:
"Stellar objects associated with a region of obscuration; in their spectrum they exhibit Balmer lines of hydrogen and the Ca II, H and K lines in emission, the equivalent width of H_α being at least 5Å. There is no supergiant or early-type (earlier than late F) photospheric absorption spectrum."
Herbig (1960) examined 26 stars exhibiting similar spectral features as those associated with T Tauri stars, but with earlier spectral types of A and B. Herbig's selection criteria included "a spectral type of A or earlier, with emission lines", the star lying in "an obscured region" and "the star illuminates fairly bright nebulosity in its immediate vicinity". The presence of associated nebulosity is crucial to distinguish between Herbig Ae/Be stars and main sequence Ae/Be stars, as both sets of stars exhibit strong emission lines in their spectra. With this in mind, Bastian et al. (1983) proposed the new definition:
"Stellar objects earlier than F0, associated with a region of obscuration and a reflection nebula; in their spectrum they exhibit emission lines of the Balmer series of hydrogen."
For the most massive stars, with masses exceeding $8M_\odot$ and spectral types of early B and O, the established star formation paradigm might be caused to break down. The increased radiation pressure from a more massive and luminous central star impedes the flow of accreting circumstellar material, making it much more difficult for matter to be transported from a disk on to the surface of the young star (Wolfire and Cassinelli, 1987; Cesaroni et al., 2007). Observatons of disks around massive YSOs are few and far between (e.g. Bik and Thi, 2004; Kraus et al., 2010; Ilee et al., 2016), likely due to their short lifetimes when compared with T Tauri disks and the fact that many massive YSOs remain embedded for the majority of their formation period, making observations problematic. Interestingly, recent observations of massive YSO disks (Kraus et al., 2010; Ilee et al., 2016) also reveal the presence of perpendicular outflows, giving credence to the idea that the star formation mechanism for lower mass stars may be "scaled-up" for their high mass counterparts (as is also suggested by the spectroscopic observations of Cooper

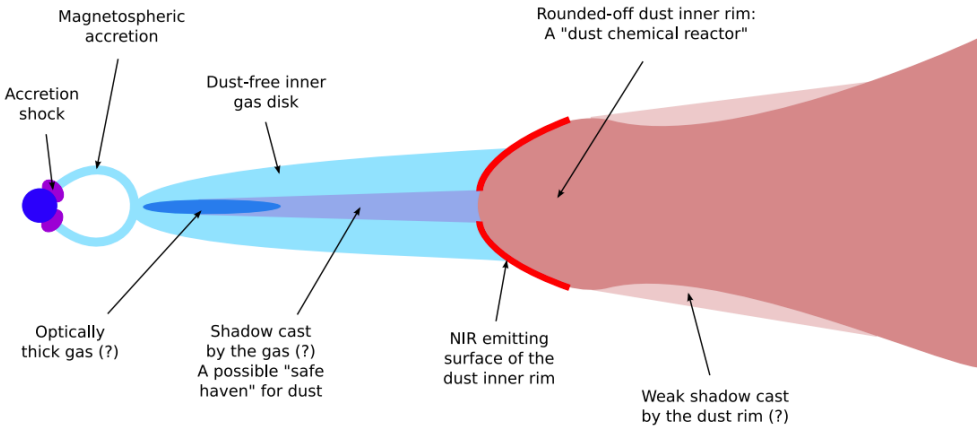

Figure 2.4.1: Schematic of the inner disk region from Dullemond and Monnier (2010) illustrating the magnetospheric accretion region, the inner gaseous disk as well as the puffed up inner rim of the dusty disk.

et al., 2013). Simulations by Krumholz et al. (2009) suggest that the increased radiation pressures from massive YSOs can be overcome via self-shielding, non-axisymmetric disks and accretion flows formed via gravitational and Rayleigh-Taylor instabilities.

2.4 The inner disk

The process of accretion transports matter through the disk towards the central star and it is in the innermost regions of the disk where the most energetic physics takes place. Here, the thermal radiation from the star heats the disk to temperatures exceeding $\sim$1500K, meaning that the majority of dust species cannot survive and are sublimated into their gaseous form. The direct heating of the inner-edge of the dust disk by the central star causes the dust rim to puff up, causing the material immediately outside the rim to be shadowed (Natta et al., 2001; Dullemond et al., 2001; Isella and Natta, 2005). The shadowed region is cooler than the surrounding material, causing the scale height to decrease, with the more extended disk material escaping from the shadow due to flaring.

The model constructed by Dullemond et al. (2001) features a vertical rim geometry, for which one would expect to observe zero emission from the irradiated dust rim for objects viewed wth a face-on geometry. This is clearly inconsistent with SED observations of Herbig Ae/Be stars, which all exhibit some emission in the near-IR no matter the viewing angle (Dominik et al., 2003). Isella and Natta (2005) proposed that the rim's shape is governed by the vertical density gradient of the disk, causing the bright side of the rim to take on a curved shape rather than a vertical wall (shown in Figure 2.4.1). Many such models

of the irradiation of the dust rim assume that the gas interior to the dust sublimation radius is optically thin, allowing the stellar radiation to propagate freely until it reaches the dust. However, Muzerolle et al. (2004) investigated the opacity of the accreting circumstellar gas and found that for high accretion rates ($M \gtrsim 10^{-8} M_{\odot} \mathrm{yr}^{-1}$) the gas becomes optically thick. Figure 2.4.1 illustrates how the optically thick accreting gas can shadow parts of the dust sublimation front.

For the majority of young stars, the near-IR continuum appears to be dominated by emission coming from the dust sublimation front, but the study by Monnier and Millan-Gabet (2002) showed that for some Herbig Ae/Be stars the emission scenario is more complex. In this study Monnier and Millan-Gabet used interferometry to derive a size-luminosity relation for a sample of Herbig Ae/Be stars (comparing the results to the expected dust sublimation radius), finding that the most luminous stars in the sample were more compact than expected. Some of the possible explanations for this phenomenon of "undersized" Herbig Be stars are discussed in the work of Kraus (2015), including:

- Optically thick gas emission partially shields the dust from the stellar radiation, allowing the dust to exist inside of the dust sublimation radius (Monnier and Millan-Gabet, 2002; Muzerolle et al., 2004, see Figure 2.4.1).
- Gas emission from inside the dust sublimation region can contribute to the near-IR continuum emission (Eisner et al., 2004).
- Highly refractory dust grain species with sublimation temperatures higher than 2000K can exist closer to the star than the most common Silicate and Carbonaceous dust grains (Benisty et al., 2010)

2.4.1 Accretion

The processes by which young stars accrete matter from their circumstellar disks play a major role in the ongoing evolution of young solar systems, by providing mass and affecting the stars' angular momentum (Bouvier et al., 2007a). Zeeman broadening measurements of magnetically-sensitive photospheric lines (Guenther et al., 1999; Johns-Krull et al., 1999) along with the detection of electron cyclotron emission (Smith et al., 2003) reveal the presence of strong $\sim 1-3$kG magnetic fields from classical T Tauri stars. Various equations for predicting stellar magnetic fields based on observable data have been published in the works of Königl (1991), Collier Cameron and Campbell (1993) and Shu et al. (1994a), assuming that a disk equilibrium state exists. with the latter including the ram pressure of the accreting material from the disk and the Keplerian rotation velocity

of the inner disk. Shu et al. (1994a) predict the integrated stellar magnetic field strength B_* (in kilogauss, kG) to be equivalent to:

$$B_* \sim \left(\frac{\alpha_x}{0.923}\right)^{-7/4}\left(\frac{M_*}{M_\odot}\right)^{5/6}\left(\frac{\dot{M}}{10^{-7}M_\odot \mathrm{yr}^{-1}}\right)^{1/2} \times \left(\frac{R_*}{R_\odot}\right)^{-3}\left(\frac{P_*}{1\ \mathrm{day}}\right)^{7/6}, \quad (2.4.1)$$

where α_x is a parameter describing the extent of the interaction between the disk and the magnetic field and $\dot{M}$ is the mass accretion rate. M_*, R_*, and P_* represent the mass, radius and rotational period of the central T Tauri star respectively. The parametrisation of α_x differs in individual studies, with Shu et al. (1994a) giving a value of 0.5 for α_x and Ostriker and Shu (1995) determining an α_x of 0.923 for a steady accretion state.

Königl (1991) invoked the mass flow model of Ghosh and Lamb (1979), which had previously been developed for X-ray pulsars and applied it to the case of circumstellar accretion disks. Königl showed that the strong magnetic fields of the T Tauri stars disrupts the inner gaseous disk a few stellar radii from the central star. Material is then channeled out of the plane of the disk along magnetic field lines towards the stellar poles, creating bright accretion shocks where the material impacts on the stellar surface. Observations of inverse P Cygni profiles (a line profile with a red-shifted absorption feature and blue-shifted emission) in the Hα line can provide evidence of infall along accretion columns (Bouvier et al., 2007b). In particular, Edwards et al. (1994) noted such profiles with the red edge of the absorption feature located between $200-300\mathrm{kms}^{-1}$indicating that the line-emitting gas is located within a few stellar radii of the central star, in the region where magnetospheric accretion must occur.

Observations of excess flux in the UV wavelength regime can be explained by the hot accretion shocks that are intrinsic to magnetospheric accretion (Muzerolle et al., 1998b). This excess manifests as the Balmer jump, a sharp increase in flux close to the limit of the Balmer series of hydrogen lines (see Section 4.2 for an explanation of spectral line series) and its strength can be used as a diagnostic of accretion rate (Herczeg and Hillenbrand, 2008). Najita et al. (2003) conducted a study of the gaseous inner disk around several T Tauri stars by observing the CO fundamental emission, finding evidence that the disks they observed were truncated as opposed to extending all the way to the central star. Measurements of T Tauri star light curves reveal rotational modulation consistent with bright surface spots caused by accretion shocks on the stellar surface (Bouvier et al., 1995). In addition to hot spot variability, it is also possible to observe the periodic obscuration of the central star by the rotating warps in the disk caused by a misaligned stellar magnetic

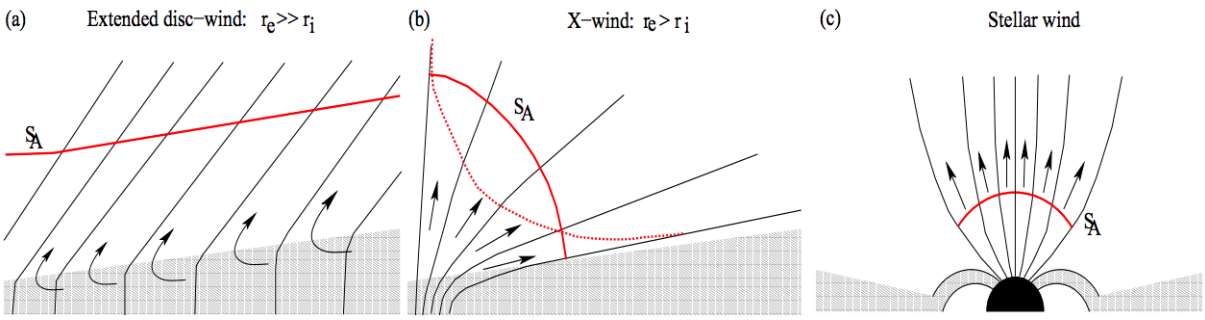

Figure 2.4.2: Schematic from Ferreira et al. (2006) showing the launching regions and Alfvén surfaces (S_A) for a disk-wind, X-wind and stellar wind.

field (Romanova et al., 2004).

2.4.2 Outflow launching

The presence of collimated outflows from young stars and the nature of their connection with the accretion process is one of the most elusive problems in the field of star formation. The evolution of jets from YSOs mirrors the evolution of the accretion system. During the initial molecular cloud collapse, when the accretion rate is high due to infall of mass from the envelope and disk, the jet is also in its most energetic phase (Pudritz et al., 2007). When the YSO has reached a steady disk accretion state the jet is optically visible and when the disk eventually disappears so does the jet (Pudritz et al., 2007). Despite the uncertainty about their origin, it is clear that these jets can efficiently extract angular momentum and gravitational potential energy from the accretion disk through their torque.
The three most commonly discussed jet-launching mechanisms are outlined in the work of Ferreira et al. (2006): extended disk winds, X-winds and stellar winds (see Figure 2.4.2). Disk winds are magnetically driven with the magnetic field threading the gaseous inner disk at a relatively large radial extension, extending out to a few au. X-winds (Shu et al., 1994b) originate from the region where the stellar magnetic field interacts with the disk at distances of just a few stellar radii. The stellar wind paradigm involves the ejection of material along the open field lines from the polar regions of the central YSO. Stellar winds are driven by their own thermal pressure gradients (Lamers and Cassinelli, 1999) rather than the angular momentum of the disk (as in the case of disk winds and X-winds). The disk wind model was first proposed by Blandford and Payne (1982) to explain the production of radio jets from active galactic nuclei. This model was then applied to accretion disks around young stellar objects by Pudritz and Norman (1983, 1986). One of the key problems in using a stellar wind as the rotational source for the outflow is outlined

in the work of Pudritz and Norman (1986), with the observed linear velocity of the jet being $\sim 200\text{kms}^{-1}$ (a stellar wind would require a mass loss rate of at least $10^{-6}M_{\odot}\text{yr}^{-1}$ to reach these velocities). In its most basic form, the theory states that under certain conditions accretion disks can drive jets via the action of large scale magnetic field by tapping the mechanical energy released in the accretion process and transferring it to the ejection portion of matter (Ferreira, 2007). The magnetic field topology in the jet-launching region of the disk is also very important: the field lines must be inclined at an angle of less than 60° to the disk plane. The mathematics behind MHD disk wind mechanisms can be found in the work of Blandford and Payne (1982), Konigl and Pudritz (2000) and Ferreira (2007).

Observations of T Tauri stars offer a useful way to constrain the physics of disk winds. Self-similar solutions for disk winds put forward by Garcia et al. (2001) show that the line-of-sight velocities for so called "cold" disk winds are greater than the velocities observed in forbidden line profiles and demonstrate that "warm" disk wind solutions provide a better match with the observed spectra. Furthermore, Anderson et al. (2003) demonstrated that it is possible to constrain the wind launching radius independently of an MHD disk wind solution by determining the stellar mass and the rotational velocity of the outflow. Applying this method to their observations of DG Tau, Anderson et al. demonstrated that the lower velocity component of the outflow originates at a radial distance of ~ 0.3 to 4AU, strengthening the idea that the slower components of the outflow are driven at larger stellocentric radii. The origin of the higher velocity outflow components is harder to constrain.

An example of such a component was reported by Anderson et al. (2003) around DG Tau, exhibiting a radial velocity of 220 kms^{-1} (also observed by Bacciotti et al., 2000). The implications of such a high radial velocity are that the wind must be launched at much smaller stellocentric radii, of order 0.1 AU or smaller. Due to its extremely compact nature, direct observations of the launching region are difficult to obtain, and so the lack of data has proven a major barrier to understanding this enigmatic process. The magneto-centrifugally driven disk-wind paradigm could be invoked at such small stellocentric radii, bu the proximity of the launching region to the central star could mean that the stellar magnetic field plays a role in the wind-launching process. This could manifest itself in the additional presence of a X-wind (Shu et al., 1994b) originating at the region where the accretion disk interacts with the stellar magnetic field. The compatibility of these X-winds with the disk wind paradigm has been called into question by Ferreira et al. (2006). For the X-wind paradigm it is assumed that there is no large-scale magnetic field, making

it incompatible with the disk wind model. Ferreira et al. conclude that the most likely scenario is that all the components (disk wind, X-wind and stellar wind) are present but most of the mass is carried by an extended magneto-centrifugally driven disk wind. More observations are needed to fully constrain which are the dominant mechanisms for mass outflow at small radial extensions of ~ 0.1 AU.

2.5 Chapter summary

In this chapter I discussed the star formation process as it is currently understood, starting with giant molecular clouds in the interstellar medium. I decribed how these clouds fragment to form individual hydrostatic cores which go on to collapse under self gravity to form protostars. I explained how the conservation of angular momentum causes circumstellar disks to form around young stellar objects and how these disks help to transport matter from the circumstellar envelope through to the central protostar. The disk's role in the transport of angular momentum away from the central protostar was also discussed.
I reviewed how disks evolve with time, with a particular focus on the change in the structure and composition of these disks as the star formation process is ongoing. I explored how the change in the structure and composition of the disk can be detected and interpreted through astonomical observations of young stellar objects. I explained how young stellar objects can be classified based on their observational characteristics, along with how these classifications give us information about the physical properties of young stars.
I focussed on the innermost regions of protoplanetary disks where the disk interacts with the star, describing how the structure of this compact inner disk is dependent on the properties of the star as well as the composition of the disk. The dynamic physical processes that take place in the innermost regions of protoplanetary disks were also explored, with a particular focus on accretion and outflow-launching mechanisms.

Chapter 3

Interferometry

3.1 Introduction

In Young's double slit experiment, the light from a distant monochromatic light source is incident on two parallel slits, projecting an interference pattern onto a screen on the far side of the slits. The interference pattern is caused by the wave-like nature of light, where each point on an expanding sphere of light behaves as if it were a new source of radiation of the same frequency and phase (argued by Huygens in *Traité de la Lumiere*, 1690). The simple analogue to this experiment is a two telescope interferometer, where light (of wavelength λ) from a single distant source is received by two telescopes separated by a baseline B, with the light then combined to form an interference pattern using a beam combining instrument. The fringe separation for this simple two-telescope interferometer can be given as,

$$\Delta\Theta = \frac{\lambda}{B} \text{ rad.} \tag{3.1.1}$$

The application of interferometry as a tool to study the heavens was first proposed by Fizeau (1854) and first carried out by Michelson to measure the diameter of Jupiter's moons (Michelson, 1891) and later the diameter of the star α Ori (Betelgeuse; Michelson and Pease, 1921).

A major advantage of astronomical interferometry is the opportunity to observe with extremely high angular resolution. The Rayleigh criterion defines the angular resolution of a single dish telescope as $1.22\frac{\lambda}{D}$, where D is the diameter of the telescope aperture. In this case, two point sources are described as resolved when the principle diffraction maximum of the first point source coincides with the principle diffraction minimum of the second. In the case of interferometry, the two point sources are described as resolved when their

fringe contrast becomes zero, which occurs when they are separated by an angle of $\frac{\lambda}{2B}$. At this separation the interference patterns created by each source will be exactly out of phase and thus will destructively interfere leaving no visible interference pattern. As the resolving power of the interferometer is directly dependent on the baseline length B, increasing the baseline length can enable astronomers to observe with unprecendent angular resolution.
In this chapter I will give an overview of the mathematical principles of interferometry, discuss the benefits of spectrally dispersed interferometry and explain how interferometric observables can be interpreted. I will examine several previous interferometric studies, exploring their impact on the field of star formation, and describe the inner workings of two specto-interferometric beam combining instruments.

3.2 Basic mathematical principles

In the following section we follow the derivations contained in Millour (2014). Considering light from a distant source we can represent the light coming from the target object as an electromagnetic wave, yielding the equations:

$$\vec{E}(\vec{z},t) = \vec{E}_0(\vec{z})e^{i\omega t},\ \vec{B}(\vec{z},t) = \vec{B}_0(\vec{z})e^{i\omega t}, \tag{3.2.1}$$

where $\vec{E}$ and $\vec{B}$ are the electric and magnetic fields respectively, $\vec{z}$ is the spatial direction, t is the time and ω is the angular frequency of the light ($\omega = \frac{2\pi c}{\lambda}$). The light intensity at the instrument focus is the superposition of the light waves that propagate through the instrument aperture:

$$I(\vec{x}) = \langle \|\vec{E}(\vec{z},t)\|^2 \rangle_t, \tag{3.2.2}$$

where $\vec{x}$ is the 2D coordinate vector onto the focal plane. For the case of an interferometer, we consider each of the telescopes to be an infinitely small pupil identified by an index i or j. The interferometer is sensitive to the coherence of the incoming light, measured by the mutual coherence function Γ. This is defined as the correlation between the two incident wavefronts $\vec{E}$ coming from positions p_i and p_j:

$$\Gamma_{i,j}(\tau) = \langle \vec{E}(\vec{p}_i, t-\tau_i)\vec{E}^*(\vec{p}_j,t) \tag{3.2.3}$$

where τ is the light delay between the two positions. Combining this with equation 3.2.2, we can express the intensity I as a function of the coherence:

$$I(\vec{x}) = \sum_i \Gamma_{i,j}(0) + \sum_{i,j} \left[ ]\Gamma_{i,j}(\tau_i - \tau_j) + {\Gamma_{i,j}}^*(\tau_i - \tau_j)\right]. \tag{3.2.4}$$

Here, $\Gamma_{i,j}(0)$ is the intensity as if there were only one coherent light source. The delays τ_i and τ_j are a function of the configuration of the interferometer and of the origin of the two incident wavefronts. If we define $\tau = \tau_i - \tau_j$, and deal with the case of two wavefronts (like an interferometer combining beams from a telecscope pair) the intensity is defined as:

$$I(\vec{x}) = I_1(\vec{x}) + I_2(\vec{x}) + \Gamma_{1,2}(\tau) + {\Gamma_{1,2}}^*(\tau). \tag{3.2.5}$$

By normalising the coherence to the total flux we obtain the complex coherence degree γ, defined as:

$$\gamma_{1,2}(\tau) = \frac{\Gamma_{1,2}(\tau)}{\Gamma_{1,1}(0) + \Gamma_{2,2}(0)}. \tag{3.2.6}$$

Considering a 1D interferogram ($\vec{x} = x$) the intensity I is expressed as:

$$I(x) = [I_1(x) + I_2(x)][1 + \mu_{1,2}^{\text{obj}} \cos\left(\frac{2\pi x}{\lambda} + \phi_{1,2}\right)], \tag{3.2.7}$$

where $\mu_{1,2}$ is the modulus of $\gamma_{1,2}(0)$ and $\phi_{1,2}$ is its phase, with the cosine modulation corresponding to the shape of the interference fringe. Equation 3.2.7 is sometimes known as "the interferometric equation", as it mathermatically describes the pattern of the interferogram with the μ term known as the visibility of the interferogram and ϕ as its phase. In this case, x is a length corresponding to the delay difference between the two beams.
The interferometric equation is a solution for the simple case of a point source, but when the target object becomes resolved things become more complex. The Van Cittert-Zernicke theorem (van Cittert, 1934; Zernike, 1938) links the value $\gamma_{1,2}(0) = \mu_{1,2}^{\text{obj}} \exp(\phi_{1,2}^{\text{obj}})$ (also called the complex visibility V) to the on-sky projection of the observed brightness distribution. This theorem can be mathematically expressed as:

$$V(u,v) = \frac{\iint_{-\infty}^{+\infty} I(x,y) e^{-2\pi i(ux+vy)} dx\, dy}{\iint_{-\infty}^{+\infty} I(x,y) dx\, dy} \tag{3.2.8}$$

$$V(u,v) = \frac{\mathscr{F}(I)}{I_{\text{tot}}} \tag{3.2.9}$$

where $I(x,y)$ is the brightness distribution of the source at angular coordinates x and y, u and v are the spatial frequency coordinates at which the visibility V is calculated. The overall implications of this theory is that the complex visibility measured by an interferometer is a Fourier transform of the on-sky brightness distibution of the target object. The full demonstration of this theory can be found in (Thompson et al., 2017). Extracting the visibility from the interferometric signal is as simple as calculating the fringe contrast:

$$V = \frac{F_{\max} - F_{\min}}{F_{\max} + F_{\min}} \tag{3.2.10}$$

where $F_{\max}$ and $F_{\min}$ are the maximum and minimum intensites of the interference fringe. Often the quantity that is observed is the squared visibility, which helps to remove biases such as detector and photon noise.

The above applies for the case in which the light from the source is unimpeded, but in reality there are several factors which affect the observation of the interference fringes. In particular, the atmospheric turbulence adds an additional term to the phase between telescopes, known as the atmospheric piston. This term corresponds to a change in the optical path difference between the two telescopes caused by the light passing through different regions of the sky, each with its own degree of turbulence (illustrated in Figure 3.2.1). The direct result of this is that the observed phase is not representative of the object phase. For longer wavelength regimes (wavelengths exceeding $\sim 100\mu$m) the phase can be directly measured as the temporal timescale of the atmosphere in the infrared is on the order of 10^{-2} seconds, whereas in the millimetre regime the timescale is on the order of tens of minutes.

For optical interferometry, the visibility is obtained in its squared form:

$$V_{i,j}^2 = |\gamma_{i,j}|^2, \tag{3.2.11}$$

which eliminates the phase, including the atmospheric piston (although biases such as "jitter" which are caused by the atmosphere are still present in the squared visibility). When observing with finite integration times the contrast of the interferogram is artificially reduced due to "smearing" caused by motion of the interferogram. This effect can be calibrated by observing the squared visibility of a calibrator star with a known size before and after the science target. Whilst interferometry remains a ground-based endeavour, atmospheric turbulence makes obtaining the true object phase impossible. However, there are several ways in which we can preserve some phase information. Phase referencing is a technique that involves observing an object close to the science source which is used to calibrate the atmospheric phase changes. This technique works well for observations

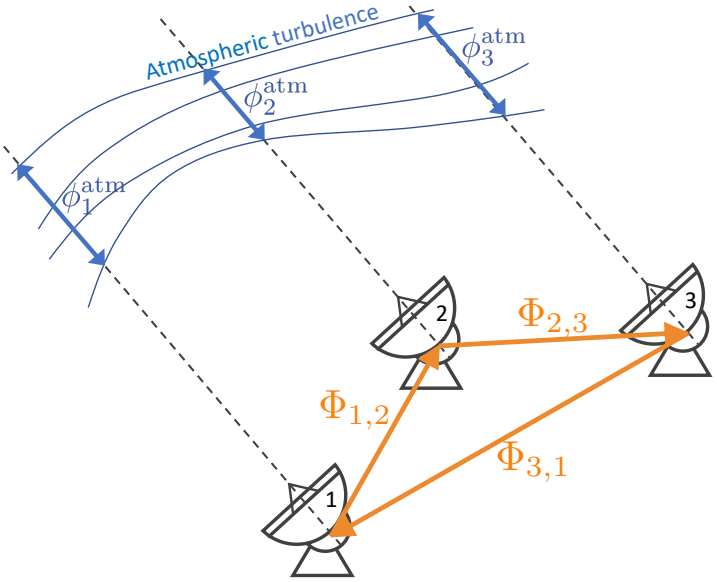

Figure 3.2.1: A diagram of a three telecope interferometer, showing how the telescope vectors and atmospheric phase constributions are defined.

in the sub-millimetre and radio regimes (Filho et al., 2008) and is beginning to produce good results for optical interferometry (GRAVITY Collaboration et al., 2017).

In 1958, Jennison outlined a new technique to obtain phase information without using phase-referencing. The concept behind this technique is shown in Figure 3.2.1 and makes use of the fact that for an interferometer with three or more apertures, the atmospheric piston term is cancelled when the phase terms are added in a closed triangle. The case of three telescopes (with indices 1, 2 and 3), the phase for each baseline is defined as:

$$\Phi_{1,2} = \phi_{1,2}^{obj} + \phi_2^{atm} - \phi_1^{atm} \tag{3.2.12}$$

$$\Phi_{2,3} = \phi_{2,3}^{obj} + \phi_3^{atm} - \phi_2^{atm} \tag{3.2.13}$$

$$\Phi_{3,1} = \phi_{3,1}^{obj} + \phi_1^{atm} - \phi_3^{atm} \tag{3.2.14}$$

where ϕ^{obj} is the object phase and ϕ^{atm} is the atmospheric piston. Summing these phases yields the result that the total phase contains only information from the object, and none of atmospheric turbulence:

$$\Psi_{1,2,3} = \Phi_{1,2} + \Phi_{2,3} + \Phi_{3,1} \tag{3.2.15}$$

$$= \phi_{1,2}^{obj} + \phi_{2,3}^{obj} + \phi_{3,1}^{obj}. \tag{3.2.16}$$

Due to this attribute the closure phase is a self-calibrating quantity, meaning that the changes in the atmospheric conditions do not need to be calibrated (as is required when measuring the visibility for example).

3.3 Spectrally dispersed interferometry

Additionally, relative phase information can be preserved by obtaining spectrally dispersed interferograms. For example, instead of directly measuring the phase we obtain the differential phase, which is a measure of the change in the object phase for adjacent spectral channels, introduced by Beckers (1982). The observed phase can be defined as a function of the wavelength:

$$\phi_{i,j}(\lambda) = \phi_{i,j}^{\text{obj}}(\lambda) + \frac{2\pi\delta(t)}{\lambda} + o\Big(\frac{1}{\lambda}\Big), \tag{3.3.1}$$

with $o\left(\frac{1}{\lambda}\right)$ denoting the higher order terms including fluctuations caused by water vapor and atmospheric turbulence. The central term $\left(\frac{2\pi\delta(t)}{\lambda}\right)$ corresponds to the optical path difference (OPD) and can be accurately estimated and subtracted from the phase measurement, leaving just the object's phase (which does not significantly vary with time but varies with wavelength) and the remaining phase variations (which can be averaged at the expense of some precision). This must be done in the complex plane, by taking the cross spectrum:

$$W^{\text{noP}} = \widetilde{\gamma_{i,j}(0)} \times e^{-2\pi i \frac{\delta(t)}{\lambda}} \tag{3.3.2}$$

where $\widetilde{\gamma_{i,j}(0)}$ denotes the observed coherent flux. In this expression the OPD term has been removed, but there remains the phase offset caused by the atmospheric piston along with some higher order terms. The phase offset can be corrected for by calculating the phase difference between the current wavelength (or "working channel") and a reference wavelength:

$$\widetilde{\phi^{\text{diff}}} = \arg\langle W^{\text{noP}}(\lambda_{\text{work}}) W^{\text{noP}}(\lambda_{\text{ref}})\rangle_t. \tag{3.3.3}$$

The reference channel can be defined as a single channel or the average of several channels, with the most common method to use the average of all channels but the working channel. The differential phase is related to the object phase via the following equation:

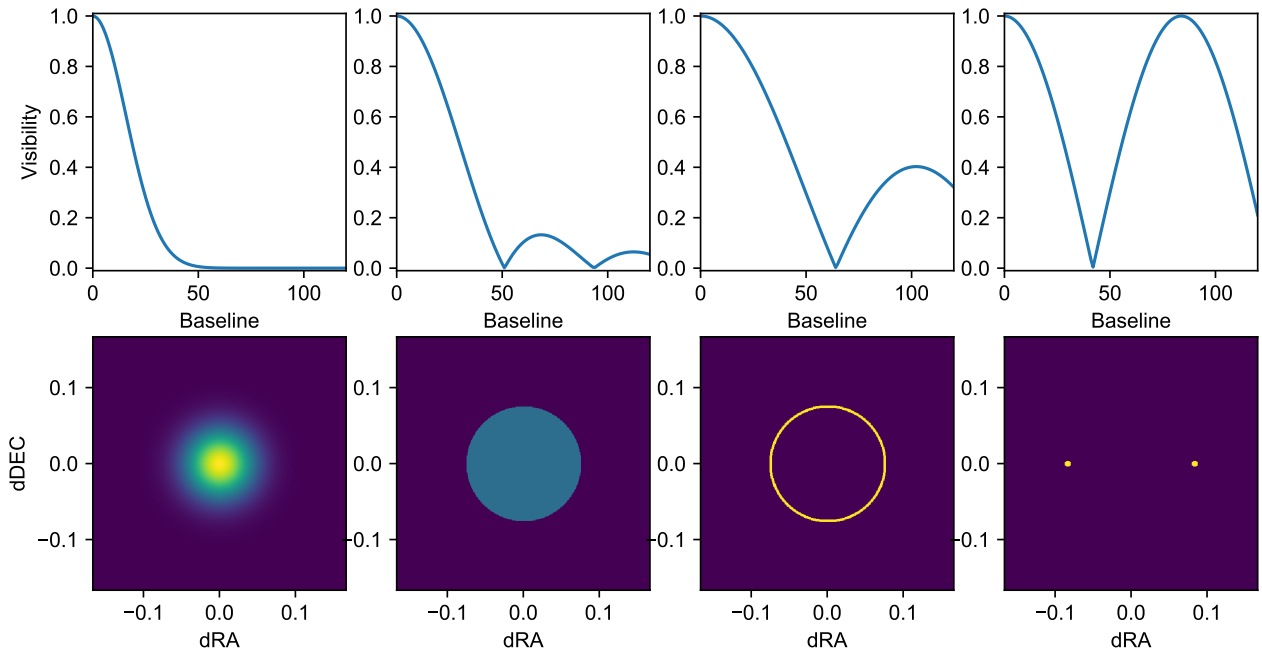

Figure 3.4.1: Visibility profiles (top) along with the corresponding brightness distributions (bottom) for several simple astrophysical scenarios, namely (from left to right) a Gaussian distribution, a uniform disk, a thin ring and a binary system.

$$\widetilde{\phi_{i,j}^{\text{obj}}} = \frac{N_\lambda - 1}{N_\lambda}\phi_{i,j}^{\text{diff}} + \frac{\alpha}{\lambda} + \beta, \tag{3.3.4}$$

where N_λ is the number of wavelength channels used as a reference.

3.4 Interpreting interferometric observables

3.4.1 Visibility modelling

Interferometric data is an immensely powerful tool to directly measure the physical characteristics of astrophysical phenomena, but the interpretation of this data is far from trivial. The visibility is the most fundamental of the interferometric observables as well as the simplest to interpret. Typically the visibility is expressed as a function of the baseline length, and this kind of visibility profile provides direct information about the characteristic size and morphology of the target object. Interpreting the visibility profile often involves calculating analytical models for the visibilities of simple scenarios such as binary stars, uniform disks, rings and Gaussian distributions. These analytical descriptions are obtained by calculating the Fourier tranforms of their respective brightness distributions,

a process that has been demonstrated in previous literature (see Berger and Segransan, 2007). An illustration of several simple visibility profiles and their corresponding brightness distributions is shown in Figure 3.4.1.

However, there are few instances where a single-component model is insufficient to account for full range of visibility information, particularly in the case of star formation where most objects contain a young star or stars (typically modelled as an unresolved delta-function) in addition to the circumstellar material. In this case, the linearity property of Fourier transforms can be employed to compute model visibilities:

$$\mathscr{F}\Big(\sum_{j=1\ldots n}\big(I_j(x,y)\big)\Big) = \sum_{j=1\ldots n}\Big(\mathscr{F}\big(I_j(x,y)\big)\Big). \tag{3.4.1}$$

Therefore the visibility of a complex brightness distribution is the normalised sum of the visibilities of the individual components that make up that brightness distribution. Along with the complexity that a multi-component model brings, all astrophysical objects such as protoplanetary disks are inclined and tilted with respect to the observer. These geometric effects mean that the object appears compressed by a factor of $\cos(i)$ when observed along the objects minor axis. It is possible to correct for this by changing the baseline reference frame to account for the rotation and compression caused by this geometric effect, a process known as "de-projection" (see Berger and Segransan, 2007). Visibility modelling is an extremely useful and versatile tool for analysing interferometric data. With a small number of data points it is possible to determine the characteristic size of an object and by increasing the range of baseline lengths that are sampled it becomes possible to distinguish between different morphologies (such as those shown in Figure 3.4.1) which only become distinct as the object is resolved. Additionally, by sampling over a wider range of position angles it is possible to determine if an object is elongated along a particular angle (possibly due to inclination effects).

3.4.2 Interpretations of the phase

The phase is a direct measure of the astrometric position of a source and, as such, contains useful information about the science target. The closure phase is strongly sensitive to an objects asymmetry, but due to the combination of multiple baselines the precise astrometric information is not retained. Non-zero closure phases indicate the presence of asymmetries in the target object whereas 0° or 180° closure phase signals are indicative of symmetric brightness distributions. However, obtaining closure phase information is

essential for interferometric image reconstruction, dicussed further in Section 5. Differential phases are sensitive to the astrometric position of the source at a specific wavelength relative to its position at a different wavelength. This quantity comes into its own when observing spectral line emission from a target source, where the differential phase directly tracks the photocentre of the line emission across different spectral channels. For line emission that arises in a high-velocity or dynamic region of space (such as a rotating disk or a high velocity jet) the Doppler broadening of the line enables measurement of the photocentre for both blue-shifted and red-shifted material. In the case of unresolved or marginally resolved objects (Le Bouquin et al., 2009) the differential phase can be used to measure the two-dimensional photocentre shifts in a model-independent way, a technique discussed in more detail in Sections 6.4, 8.3.2 and 6.10. In addition to the differential phase, wavelength-dependent visibilities are also obtained. The change in the visibility across the spectral line reflects the change in the characteristic size of the object from just continuum emission to a combination of line and continuum. Interpreting this kind of visibility requires a multi-component model as one must simultaneously fit the continuum emission as well as the line-emitting component. The best way to simultaneously fit the wavelength-dependent visibilities, differential phases and spectrum is via kinematic modelling, a process discussed further in Section 4.

3.5 Observing star formation with interferometry

Star formation is a field that is well suited to interferometric study as the process is characterised by the presence of circumstellar material. The majority of the dynamic physical mechanisms that are essential to formation of star systems take place in their protoplanetary disks. Whilst these disks can extend out to hundreds of au from the central star, the majority of star forming regions in our galaxy are distant, the closest being $\sim$140pc away. This means that interferometry is the best tool to achieve the high angular resolution required to directly observe protoplanetary disks. An in depth discussion of the processes involved in observing disks with interferometry are discussed further in Sections 3 and 5. Kraus et al. (2008a) used VLTI/AMBER in the K band to measure the Brγ hydrogen line emission around five Herbig Ae/Be stars, namely HD 163296, HD 104237, HD 98922, MWC297 and V921 Sco. Whilst Brγ is known to trace hydrogen gas inside the inner dust rim (Eisner et al., 2010), the precise kinematics of the gas and the physical processes that it traces are difficult to constrain. Initial AMBER observations of the Herbig Be star MWC 297 by Malbet et al. (2007) indicated that the spatial origin of the Brγ line emis-

sion is more extended than the continuum. Similar observations by Tatulli et al. (2007) of the Herbig Ae star HD 104237 showed no visibility changes in the Brγ line, indicating that the line-emission arises in the same region as the continuum for this object. This gave Kraus et al. cause to believe that the mechanisms traced by Brγ emission are different for different objects. They posited that for HD 163296, HD 104237, MWC297, and V921 Sco the Brγ emission is caused by the excitation of outflowing gas launched either by an extended stellar wind or a disk wind. For HD 98922, they found that the line-emitting region is much more compact, consistent with a magnetospheric accretion scenario. By observing a diverse sample of Herbig Ae/Be stars, Kraus et al. were able to investigate general trends across the population, finding that the Brγ line intensity did not depend on the stellar parameters such as luminosity but that there was a connection with other spectroscopic features such as the Hα line profile.

AMBER's MR mode is useful for distinguishing the differences between line and continuum, but with a spectral resolution of $R = 12\,000$, the HR mode has the capability to measure the kinematics of the line emission from a young star. Weigelt et al. (2011) used the HR mode to observe MWC297, obtaining a hour-angle with a compact linear configuration of the VLTI auxiliary telescopes (ATs). Weigelt et al. observed strong differential phases across the Brγ line along with a drop in the visibilities in the line, indicating that the line-emitting region is $\sim$3 times more extended than the continuum. Weigelt et al. fit their AMBER data with a kinematic model of a disk wind, with a half-opening angle (the angle between the rotation axis and the innermost streamline of the disk wind) of 80°.

Kraus et al. (2012a) also used AMBER's high spectral dispersion mode to study the kinematics of line-emitting gas, this time around the Herbig B[e] star V921 Sco. Using the AMBER data to fit a kinematic model of a rotating Keplerian disk, Kraus et al. obtained spectro-astrometric data from the CRIRES at the VLT. This data was used to calculate photocentre displacement vectors (similar to those discussed prevously in Section 3.4) as well as being incorporated into the kinematic modelling fit.

Kurosawa et al. (2016) modelled the kinematics around the Herbig Ae star HD 58647 using the Torus radiative transfer code, finding an optimal fit to their AMBER HR-K data using a model of a disk wind with a magnetospheric component. Garcia Lopez et al. (2015) used AMBER's HR-K mode to observe the Herbig Ae star MWC 275 with the UT2-UT3-UT4 configuration across three epochs. Their observations indicated that the Brγ emitting region is more compact than the continuum for this object, consistent with the findings of Kraus et al. (2008a). Using the non-LTE disk wind model discussed in the previous works of Weigelt et al. (2011), Grinin and Tambovtseva (2011) and Tam-

bovtseva et al. (2014) they simulated an outflow scenario using their observations. Their best-fit disk wind model suggests a very compact wind-launching region 2-4 stellar radii (0.02-0.04au) with a half-opening angle of 45°. Caratti o Garatti et al. (2015) used a similar technique to study HD98922 whilst also observing the object using the VLT/SINFONI instrument. Similar to Garcia Lopez et al., they found that the Brγ emitting region is more compact that the continuum for this object. Using the same non-LTE model as above, they found that their observations fitted a disk-wind scenario with a half-opening angle of 30° and a compact wind launching region extending from 0.1-1au.

Surveying a large number of astronomical targets is a difficult task with interferometry as each observation is a difficult and intenstive process and achieves a very small field of view. However, Eisner et al. (2004) and Lazareff et al. (2017) demonstrate how such works help to further our knowledge of the star formation process as a whole, finding trends between stellar properties and interferometric observables. Eisner et al. (2004) used the Palomar Testbed Interferometer (PTI) to observe fourteen Herbig Ae/Be stars in the K-band, resolving the inner disk around all but two of their targets. Eisner et al. found that earlier-type objects were best-fit with geometrically flat accretion disk models, whilst the later type objects were better explained with models incorporating puffed-up inner disk walls. Later, Eisner et al. (2005) used the Keck interferometer to observe the K-band ($\sim$2.2μm) continuum around four T-Tauri stars, simulating the emission with models of incorporating puffed up inner disk walls. Lazareff et al. (2017) expanded upon the work of Monnier and Millan-Gabet (2002) by investigating the relation between the interferometric size-luminosity relation, observing a wide spread of sizes that can not be fully explained by the different sublimations temperatures of the various dust species. More seminal interferometric studies focusing on image reconstruction are discussed in Chapter 5.

3.6 Spectrally dispersed beam-combining instruments

3.6.1 VLTI/AMBER

AMBER (Astronomical Multi-BEam combineR, Petrov et al., 2007) was a near-infrared (J, H and K bands, i.e. 1.1μm to 2.4μm) beam combiner at the VLTI, the first instrument at the VLTI capable of achieving spectrally dispersed interferometry in this wavelength regime. The VLTI array is comprised of four 8.2 metre unit telescopes (UTs) which are fixed in position and four 1.8 metre auxilliary telescopes (ATs) which are free to move to different positions along tracks. AMBER was designed to achieve coherent combination

of three telescope beams, enabling observers to obtain visibility and closure phase information (see Figure 3.6.1). The light from the three VLTI telescopes is spatially filtered through single-mode fibres (resulting in a 65 mas field of view for the UTs and 280 mas for the ATs) before being passed through beam splitters, to separate the light between recombination and the photometric channels. The multi-axial beam recombination system is set up for the output baselines to be non-redundant, so that the individual interference fringes that correspond to each baseline are easily distinguishable. The three photometric channels and the interference fringes are then dispersed using a prism for the low spectral dispersion mode ($R = 35$) or grisms for the MR ($R = 1\,500$) and HR ($R = 12\,000$) modes. Each of these spectral modes offer different functionality:

- The low spectral dispersion mode (LR) covers a wide spectral range, from $\sim 1.5 - 2.4\mu$m in one exposure. This is useful for observing wavelength dependence in continuum-emitting structures as well as improving *uv*-coverage, making use of the fact that spatial frequency is proportional to the wavenumber $\left(\frac{1}{\lambda}\right)$.

- The medium spectral dispersion (MR) mode is able to resolve individual spectral lines and distinguish between line emission and continuum emission. Additionally, the wide spectral range covered (not as wide as LR but still able to cover an entire spectral band) enables the observer to simultaneously observe several spectral features at once, provided that they are in the same spectral band.

- The high spectral dispersion (HR) mode covers a much smaller wavelength range than the previously discussed modes, but can achieve the spectral resolution required to resolve a Doppler-broadened spectral line over tens of spectral channels ($R = 12\,000$). This mode requires bright targets and favourable atmospheric conditions but allows the observer to constrain the high-order kinematics of the line-emitting material from the target source.

Since 2007, AMBER has made use of the fringe tracking instrument FINITO (Gai et al., 2004; Le Bouquin et al., 2008). FINITO measures the phase difference between the telescope light beams in real time and uses the VLTI delay lines in order to counteract the atmospheric piston, allowing for longer integrations for observations using AMBER's MR and HR modes. The introduction of FINITO greatly improved the quality of high-dispersion spectro-interferometry data available from the VLTI.
AMBER achieved first fringes in March 2004, with the instrument becoming available for general use with the UTs in 2006 (ESO P77) and the ATs in 2007 (ESO P79). In 2018

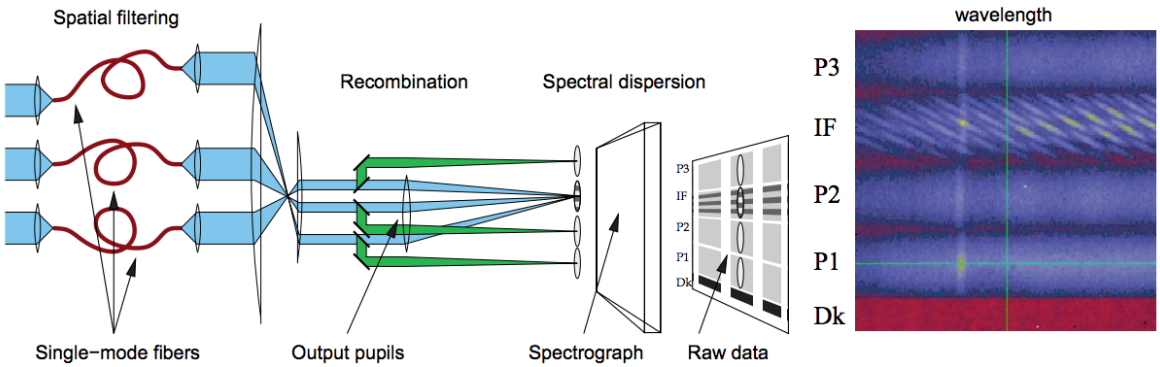

Figure 3.6.1: Figure from Petrov et al. (2007) illustrating the AMBER instrument design. The three beams are spatially filtered through single-mode fibres, recombined and then spectrally dispersed via a prism (LR) or grism (MR and HR) on to the detector.

(P101) AMBER was decommissioned to make way for the next generation of spectrally dispersed beam combiner at the VLTI. An overview of the AMBER data reduction process can be found in Tatulli et al. (2007).

3.6.2 VLTI/GRAVITY

GRAVITY (Gillessen et al., 2010) is a second-generation beam combining instrument for the VLTI, with a focus on extremely small-scale astrometry as well as phase-referenced interferometric imaging for faint objects in the K-band. GRAVITY offers spectrally dispersed interferometry between 1.95 and 2.45μm with a maximum spectral dispersion of $R\sim$4000. Amongst the primary scientific goals for the instrument is the observation of gas clouds and stars passing close to Sgr A*, the supermassive black hole at the centre of our galaxy (Gravity Collaboration et al., 2018a,0). The GRAVITY project has many secondary scientific aims, ranging from exoplanet detection and characterisation to probing the nature of NIR emission from microquasars, along with studying the line emission from the inner regions of protoplanetary disks.

Whilst being a step down from AMBER in terms of spectral resolution (moving from $R = 12\ 000$ to $R = 4\ 000$), GRAVITY offers numerous improvements over the former VLTI instrument. The ability to combine beams from four telescopes doubles the number of *uv*-points that can be sampled from in a single observation over what could previously be achieved with AMBER (from 3 baselines to 6). GRAVITY can achieve unprecedented sensitivity for a spectro-interferometric beam combiner, with limiting correlated magnitudes of 10.0 in single-field mode (9.0 with the ATs) and 17.5 with dual-field tracking (16.5 with the ATs). For the field of star formation this opens up the possibility to probe a

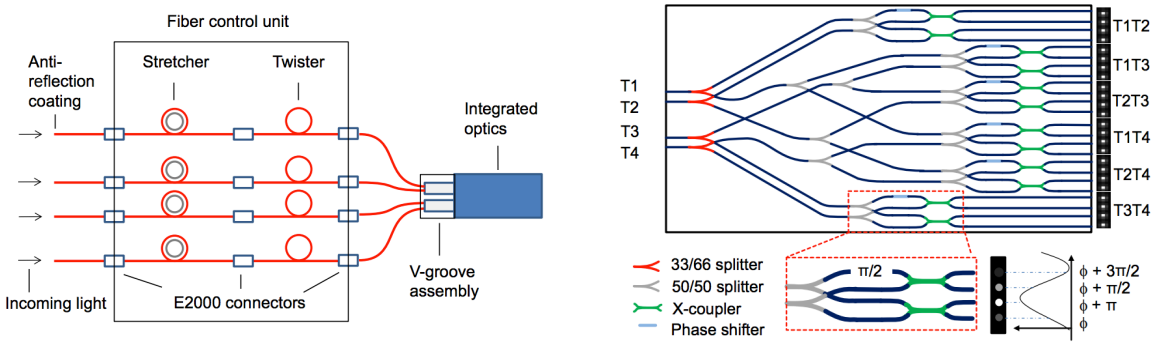

Figure 3.6.2: Figures from Gravity Collaboration et al. (2018a) illustrating aspects of the GRAVITY instrument design. Left: The fibre control unit setup for GRAVITY, showing how the optical path length and polarisation are varied. Right: The integrated chip setup showing how the four telescope beams are input on the left, phase-shifted and recoupled resulting in the output on the right.

new regime of young stellar objects, namely the lower mass T Tauri stars which typically have magnitudes fainter than ∼7.0. This increased sensitivity also means that a higher SNR is achievable for the brighter objects that were previously observed with AMBER. The GRAVITY setup also utilizes the wide, 2" field of view of the VLTI as well as taking advantage of the adaptive optics systems for infrared wavefront sensing.

The working principle of GRAVITY is discussed in Gillessen et al. (2010) and again in GRAVITY Collaboration et al. (2017). A bright star close to the science target (but outside the 2" FOV) is imaged with the Coudé infrared adaptive optics sensors (CIAO) and the wavefront correction is applied using a deformable mirror AO system (MACAO or NAOMI, Arsenault et al., 2003; Dorn et al., 2014). Both the science target and the phase reference star (within the VLTI's 2" FOV) are then imaged using the delay lines before interferometry is achieved using the GRAVITY beam combiner. The light from each of the four telescopes is passed through a fibre control unit where the polarisation and the differential optical path length are controlled by twisting and stretching the fibres (Figure 3.6.2, left). The actual interference of the telescope beams takes place on a single silica-on-silicon integrated optics chip. The four beams are fed into the chip, where they are then split, phase-shifted and then re-coupled to output six groups of four beams, one group for each baseline combination (Figure 3.6.2, right). Each of the beams in this group contains the interference information for a relative phase shifts of 0, $+\frac{\pi}{2}$, $+\pi$ and $\frac{3\pi}{2}$.
The 24 output beams from the integrated optics chip are input into a fringe tracking spectrometer and a science spectrometer. The fringe-tracking spectrometer is optimised for high frame-rate readout in the kHz regime, with six spectral channels. The science spec-

trometer has the option to use spectral resolutions of $R = 22$, $R = 500$ and $R = 4000$ and is optimised for long integrations, with durations ranging from seconds up to minutes. These long integration times are ideal for faint objects where high spectral dispersion is necessary, such as young stellar objects.

3.7 Chapter summary

In this chapter I have discussed the theory of interferometry and its application in the field of observational astronomy. I have shown how interferometry enables astronomers to observe with an angular resolution far superior than what can currently be achieved using a traditional single-aperture telescope. Starting from first principles I have described how light can be combined from multiple telescopes to construct interference fringes which can be used to infer information about the astronomical target source. The visibility extracted from the interference pattern is related to the on-sky brightness distribution of the observed astronomical target via the Van Cittert-Zernicke theorem, which states that the visibility is the Fourier transform of the brightness distribution. Obtaining spectrally-dispersed interferograms is a useful way to preserve wavelength differential observables for objects which exhibit spectral line emission.

I haven given an overview of the different observables obtained using interferometry and explained how different information about the target scource can be extracted from each different observable. The interpretation of interferometric observables such as the visibility and phase is discussed, as well as how different aspects of the data can be interpreted using models. I explored how interferometry has successfully been used to study star formation in the past and discussed the impact of the technique on our understanding of the star formation process.

I have given an overview of the internal workings of two spectrally dispersed beam combining instruments that are used in this thesis, namely AMBER and GRAVITY. I have shown how these two instruments use different methods to obtain interferograms with various spectral dispersions.

Chapter 4

Kinematic modelling

4.1 Introduction

Observing spectral line emission is a powerful tool for analysing the physical conditions in astronomical phenomena, as well as acting as a diagnostic for the presence of complex molecules. The emission of spectral lines from celestial objects is in itself an interesting process, as it represents a link between the macroscopic astrophysical phenomena and the microscopic quantum regime. In the case of protoplanetary disks, particles within the disk can exist only in a series of discrete quantum energy states. When transitions between states occur, photons are emitted with a wavelength (λ) related to the energy gap (E) by the relation:

$$\lambda = \frac{hc}{E}, \tag{4.1.1}$$

where h is the Planck constant and c is the speed of light.

The appearance of spectral lines is governed by the laws laid down by Kirchhoff (1860):

1. A hot, dense gas (or plasma) will emit light at all wavelengths as a black body.
2. A low density, hot gas in front of a cool, low density background with emit an emission line spectrum.
3. A low density, cool gas in front of a hot, black-body source will exhibit an absorption spectrum.

Each particle present in a disk has its own unique set of energy states, meaning that they all have a unique spectral signature. This allows astronomers to determine the chemical composition of the circumstellar material that is observed. However, the shape of the

spectral line holds a great deal more information about the physics of the line-emitting material. Emission lines can be broadened by several mechanisms, such as the Zeeman effect, natural broadening and the Doppler effect. Doppler broadening occurs when an emission line is emitted by material that is in motion along the line of sight of the observer, with material that is moving faster in the line of sight exhibiting a larger doppler shift. This means that measuring the line's width, relative to the central wavelength, yields the maximum velocity of the line-emitting material along the line of sight (see Equation 4.3.1). Further exploration of the interpretation of line profiles is discussed in Section 4.3.

4.2 Spectral series

A simple approximation of an atom, the Bohr model, postulates that atoms consist of a nucleus surrounded by one or more electrons moving in circular orbits. As the mass of the electrons is negligible when compared to the mass of the nucleus, the nucleus is fixed at the centre of mass of the atomic system. The electrons have de Broglie wavelengths of the form:

$$\lambda_e = \frac{h}{p} = \frac{h}{m_e v}, \tag{4.2.1}$$

where p is the electron's momentum, m_e is its mass and v its velocity. Electrons can only achieve a stable orbit around a nucleus in a standing wave state, meaning the circumference of the electrons n'th orbit must be equal to the integer value n (known as the principle quantum number) multiplied by λ_e:

$$2\pi a_n = n\lambda_e = \frac{hn}{m_e v} \tag{4.2.2}$$

where a is the Bohr radius. Rearranging these equations gives the result:

$$L = a_n m_e v = n\hbar \tag{4.2.3}$$

where L is the angular momentum and $\hbar$ is the reduced Planck constant $\left(\frac{h}{2\pi}\right)$. Balancing the Coulomb attraction with the centripetal force for the simplest case of a hydrogen atom we find:

$$\frac{e^2}{a_n^2} = \frac{m_e v^2}{a_n}. \tag{4.2.4}$$

Combining this relation with Eq. 4.2.3 we can define a_n in terms of n and physical constants:

$$a_n = \frac{n^2\hbar^2}{m_e e^2}. \tag{4.2.5}$$

An electron in this atom can fall from a given level n to any level $n' = n - \Delta n$ by emitting a photon with an energy corresponding to the energy difference between the two levels. The resulting spectral lines are called recombination lines as when formerly free electrons recombine with ions they cascade down the energy levels emitting photons before reaching the ground state.
The total energy of an electron in a hydrogen atom is the sum of its kinetic and potential energy:

$$E = E_k + E_p = \frac{1}{2}E_p = \frac{-e^2}{2a_n} = -e^2\left(\frac{m_e e^2}{2n^2\hbar^2}\right) = -\left(\frac{m_e e^4}{\hbar^2}\right)n^{-2}. \tag{4.2.6}$$

The energy change of a photon dropping from an energy level n to an energy level n' is conserved as a photon $h\nu$:

$$\Delta E = \frac{m_e e^4}{2\hbar^2}[n'^{-2} - n^{-2}] = h\nu. \tag{4.2.7}$$

Therefore we can define the frequency of the emitted photon as:

$$\nu = \left(\frac{2\pi^2 m_e e^4}{h^3 c}\right) c\ [n'^{-2} - n^{-2}] \tag{4.2.8}$$

The first term in this equation is known as the Rydberg constant, $R_\infty = 1.097 \times 10^7 \mathrm{m}^{-1}$. Conducting the same derivation using the reduced mass instead of assuming a negligible electron mass yields the equation:

$$\frac{1}{\lambda} = R_\infty\left(1 + \frac{m_e}{M}\right)^{-1}[n'^{-2} - n^{-2}]. \tag{4.2.9}$$

It must be stated that these derivations rely on a treatment of the Hydrogen atom that is incomplete, and which has since been replaced with a full quantum mechanical model. Indeed, some observational effects such as natural broadening cannot be explained without invoking quantum mechanics and are therefore inconsistent with the Bohr model used above.
Observationally, these mechanisms manifest themselves as series of lines which are char-

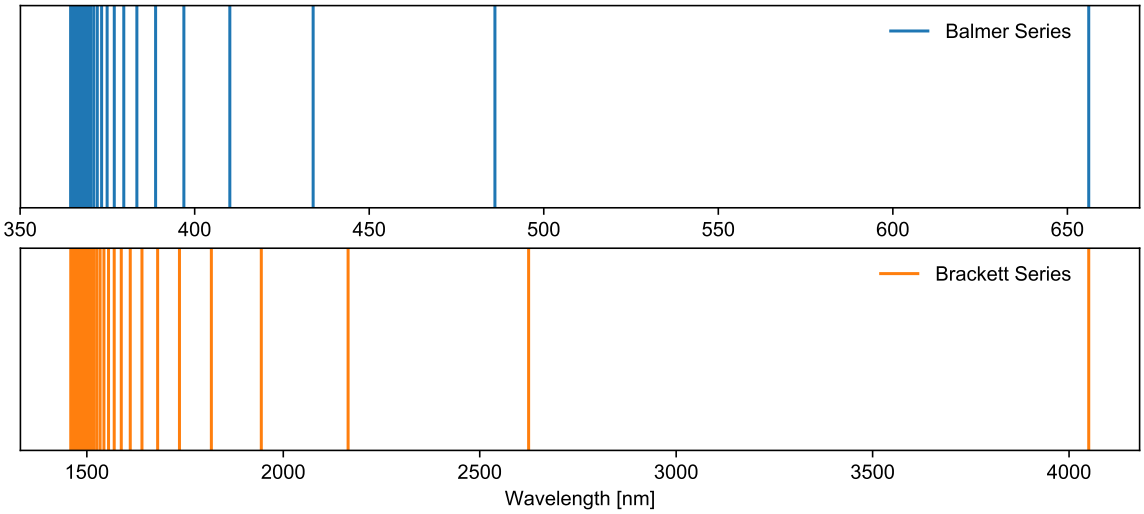

Figure 4.2.1: The wavelength positions of the Balmer series ($n' = 2$, top) and the Brackett series ($n' = 4$, bottom) of Hydrogen lines, showing how the spacings between each line change with wavelength.

acterised by the final energy state in which the electron sits. We can see from Eq. 4.2.9 that for large values of n the n^{-2} term becomes negligible, meaning the emitted wavelength is dominated by the final rest channel n'. The result is a characteristic pattern of emission lines between $\lambda_{\Delta n=1}$ and $\lambda_{\Delta n=\infty}$ that are spaced further apart with increasing wavelength (shown for Hydrogen spectral series in Figure 4.2.1). In this thesis we focus on spectral lines in the H and K bands, namely lines in the Brackett series. These lines are referred to by the shorthand notation of the series (i.e. Br for Brackett) followed by the transition number (equal to n' - n). For lower order lines the transition number is often replaced by the corresponding letter in the greek alphabet, for instance the $n = 7$ to $n' = 4$ transition is referred to as Brγ and the $n = 10$ to $n' = 4$ transition is referred to as Br6.

4.3 Interpreting spectral line profiles

Whilst the wavelength of a line can be used to determine the chemistry and excitation energy of a line-emitting species, more information can be gleaned from the line's shape or "profile". The Doppler effect predicts how the frequency ν of line emission is affected by the velocity v of the line-emitting gas along the observer's line of sight:

$$\nu_{\text{obs}} = \left(1 + \frac{v}{c}\right)\nu_{\text{emit}} \tag{4.3.1}$$

This can be used to find the objects line-of-sight velocity compared with the local standard of rest (LOS). The Doppler effect causes broadening within spectral lines that come from a single source and material can be blue- and red-shifted by kinematic processes such as rotation or accretion. In these cases the line profile is a strong diagnostic of the nature of the processes that form the emission. The width of the line relative to its central wavelength is directly related to the maximum line-of-sight velocity, which can be used to infer information about the kinematics of the line-emitting gas as well as the inclination of the disk. The use of physical models to interpret spectral line observations has yielded many interesting results which have increased understanding of the dynamic processes involved with star formation.

4.4 Kinematic scenarios in star formation

Accreting circumstellar matter is subject to many different velocity fields as it propagates through the disk towards the central star. The outer regions of protoplanetary disks experience Keplerian rotation, as well as infall through the disk towards the central star, whilst the inner-most regions of the disk are host to the complex kinematic scenarios of magnetospheric accretion and outflow launching. Each of these different scenarios is characterised by line emission in a different wavelength regime.

4.4.1 Keplerian rotation

The majority of material within circumstellar disks orbits the central star according to Kepler's laws of orbital motion. Kepler's third law can be demonstrated by equating the gravitational attractive force with the centripetal force felt by an orbiting particle of mass m:

$$\frac{GMm}{r^2} = \frac{mv^2}{r} \tag{4.4.1}$$

where M is the mass of the central star, r is the semi-major axis of the orbit, v is the orbital velocity and G is the gravitational constant. Re-arranging this equation to find the velocity yields

$$v = \sqrt{\frac{GM}{r}} \tag{4.4.2}$$

as well as the relation that the square of the orbital period is directly proportional to the cube of the semi-major axis ($T^2 = \frac{4\pi^2}{GM}a^3$). As a result, high velocity material is found

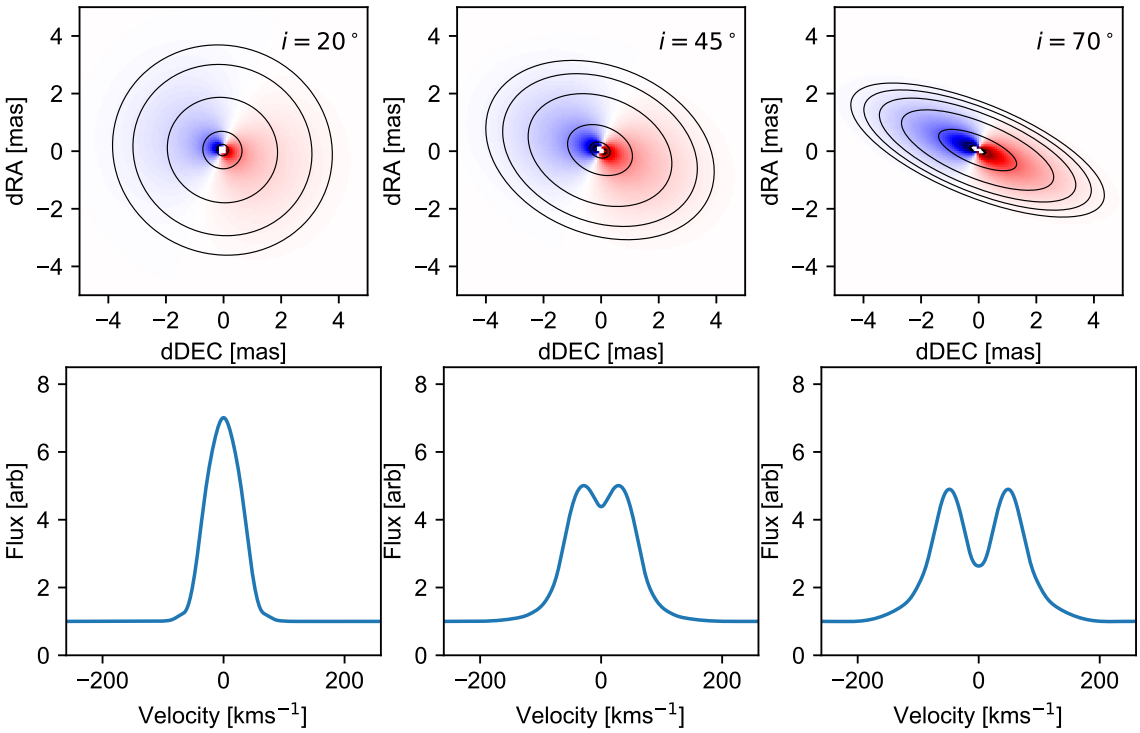

Figure 4.4.1: Moment maps (top) and simulated spectra (bottom) for a Keplerian disk viewed at a range of inclinations. This illustrates how the spectral shape is strongly dependent on the disk inclination. The darkness of the blue and red colour is proportional to the line-of-sight velocity of the Doppler shifted material.

closer to the central star, with lower velocity material occupying the more extended region of the disk.

Keplerian rotation is typically associated with a double-peaked line profile that results from the Doppler broadening of the line caused by material with different orbital velocities. The shape of the spectral line can be a used as a diagnostic for the inclination of the disk as seen by the observer, with a disk viewed close to edge-on exhibiting a larger range of velocities in the line of sight than a disk viewed close to face-on (see Figure 4.4.1). Additionally, as the inclination increases the spectrum becomes more double peaked, with a larger depression in the line centre.

4.4.2 Disk winds

The inner disk is host to more complex and dynamic kinematics, with both infall and outflow mechanisms playing a large role. A frequently discussed outflow-launching sce-

nario is the disk wind model, as introduced in Section 2.4.2. As the outflowing material is launched from the surface of the disk in this scenario, the line-emitting material still exhibits Keplerian rotation in addition to the out-of-plane velocity component. The driving force for the ejection in the disk wind paradigm is the large-scale magnetic field which permeates the disk and accelerates material along the magnetic field lines. Knigge et al. (1995) first demonstrated a biconical geometric approximation for such a scenario, where the wind acceleration streamlines are defined as straight lines which extend from an imaginary source behind the disk between a range of angles (an illustration of this geometry is included in Section 6.7). Other wind launching scenarios, such as thermally driven disk winds (Sauty and Tsinganos, 1994), are not considered as part of our modelling framework but may be an important part of the outflow scenario for young stars, particularly for more luminous Herbig Ae/Be stars.

4.5 Modelling framework

Kinematic modelling requires creating separate models for each of the sampled wavelength channels, making it a computationally intensive venture. To compute the differential interferometric quantities we make use of the principles laid out in Section 3.2 to extract interferometric observables from our 2D model intensity maps. The Fourier transform of each model frame is calculated, and the 2D visibility and phase are extracted at the spatial frequencies that correspond to each of the baselines sampled in the *uv* plane of our specific observation. We often simultaneously model multiple data sets which have a range of different wavelength dispersions, such as in the case where we compare models to high resolution spectra as well as spectro-interferometric data. In this case the spectral resolution of our model must align with the data set which has the highest spectral dispersion, with the data then being convolved to the spectral response of the lower-resolution data. In order to find the correct convolution we compare the spectra and use the convolution function that results in a match of the width of the telluric lines. From the extraction we obtain velocity-dependent visibilities, differential phases and a spectrum that we can directly compare with the observed wavelength-dependent data. The channel velocity $v_{\rm chan}$ is converted to wavelength $\lambda_{\rm chan}$ using the following equation:

$$\lambda_{\rm chan} = \lambda_{\rm rest}\left(1 + \frac{v_{\rm chan}}{c}\right) \tag{4.5.1}$$

where $\lambda_{\rm rest}$ is the rest wavelength of the line and c is the speed of light.

4.5.1 Pure kinematic 2D modelling code (simmap)

Our versatile in-house 2D kinematic modelling code (hereafter referred to as simmap) offers a useful way to explore a large range of kinematic scenarios and directly interpret differential interferometric quantities. This code (primarily developed by Stefan Kraus) has been previously used to model the bipolar wind from η Car (Weigelt et al., 2007) and the accretion disk around V921 Sco (Kraus et al., 2012c). This code creates a two-dimensional, geometrically thin representation of a YSO disk system as it is viewed on-sky by an observer, with the pixel scale of the model image assigned a size in units of milli-arcseconds. The simmap code then evaluates each of the regions associated with each pixel and calculates that pixel's intensity according to the intensity functions that are being modelled.

It is important to construct an accurate model for the continuum emission, as this is an essential comparison point for calculating the differential interferometric quantities. Along with a delta function to simulate the central, unresolved star we can model the continuum emission with a range of different intensity distributions. For objects where the continuum emission is only marginally resolved, a simple inclined Gaussian distribution is sufficient to determine that visibility level as well as the flux ratio between the star and the disk. Where the object is more resolved, a ring or temperature-gradient disk model can offer a better fit to the more complex visibility data in the second lobe (see Section 3.4.1 and Figure 3.4.1).

The line-emitting region is defined as an axisymmetric region around the central star between an inner radius $R_{\rm in}$ and outer radius $R_{\rm out}$. Within this region the intensity of the emission is proportional to the radius, varying with r^{β}, where r is the radius and β is a free parameter. Using the stellar mass $M_{\star}$ and distance D, the Keplerian rotation velocity is calculated for each point in the line-emitting region. The variation of the rotational velocity as a function of radius can be altered within the code, along with the ability to scale the velocity field as a function of the Keplerian velocity. Additionally, a velocity component can be introduced that simulates the infall of material through the disk towards the central star. The disk's inclination is then taken into account and the velocity for each pixel in the line of sight of the observer is determined. For the more complex case of a disk wind, the out-of-plane velocity vectors extend through the disk from an imaginary source offset from the centre of the disk in the z direction (Knigge et al., 1995). The distance of the imaginary source from the disk D_z determines the degree of collimation of the wind at the inner radius and subsequently throughout the line-emitting region. The out-of-plane velocity can be defined either as a constant velocity or as a function of the

Keplerian velocity. For each pixel the velocity along the observers line of sight is calculated and added to the existing rotational velocity.
With the velocity field defined we can then calculate a 2D intensity map for a range of velocities. We define our sample velocity channels to reflect the spectral dispersion of the highest resolution data set that we are modelling. Using a Python wrapper, a series of 2D frames is calculated for each velocity bin. The interferometric observables are extracted using the method discussed above and converted to the corresponding wavelength using Eq. 4.3.1. The resulting series of wavelength dependent quantities are then compared with the observed data.
My personal contribution to the simmap code was revolved around constructing a Python interface with the code which allows the user to easily construct a kinematic scenario (or series of scenarios) to explore. I also helped to developed the code that extracts the interferometric quantities from the model images, along with developing code that compares these quantities with the observed data. The framework that I developed has been incorporated into the analysis software that has also been used by my collaborators on projects that are not featured as part of this PhD

4.6 Chapter summary

In this chapter I have given an overview of the mechanisms by which particles emit light at specific wavelengths and how such emission lines carry information about motion of line-emitting species. I have discussed the formation of spectral line series, with a particular focus on the hydrogen recombination series that are the subject of our spectro-interferometric observations in this thesis. I explored how the shape or profile of a spectral line can be used to infer information about the location and kinematics of the line-emitting material, making it a useful diagnostic for the dynamical mechanisms involved in the formation of stars. I have demonstrated how emission line profiles can also be used to derive information about the orientation of a disk system.
Material that propagates through an accretion disk experiences multiple different velocity fields before it reaches the central star. In this chapter I have summarised the physics behind the Keplerian rotation and disk wind velocity fields, as well as outlining how they are applicable to a protoplanetary disk system. I have given an overview of the kinematic modelling framework that is used to model the spectro-interferometric data in this thesis, explaining how I synthesise interferometric observables from model image frames. The specific modelling code that I have employed to construct velocity-dependent model

images is described in detail, along with previous studies that were conducted using this code.

Chapter 5

Chromatic image reconstruction

5.1 Introduction

Interferometric image reconstruction is a powerful technique for creating visual representations of astronomical objects with extremely high angular resolution. Whilst image reconstruction is not a model-independent process, it allows for a more direct interpretation of interferometric data than traditional modelling techniques. This is particularly useful in cases where model fitting is challenging, such as in the case where the brightness distribution is complex and asymmetric. In these cases, model fitting can yield results that do not accurately represent the true brightness distribution. The process reduces the data from its raw interferometric form into an intuitive, on-sky brightness distribution, the interpretation of which has been at the core of astronomy since its inception.

The interferometric investigations that have successfully achieved image reconstruction rank amongst the most seminal and impactful works that have been achieved with interferometry. A contributing factor to this is that image-reconstruction requires a large ammount of data, so studies that can achieve image reconstruction can also present extremely detailed analysis of the raw interferometric data. For instance, Monnier et al. (2007) used the CHARA array to construct an image of the surface of the rapidly rotating A7 star Altair (α Aquilae). The image (see Figure 5.1.1, panel a) that Monnier et al. presented showed that fast rotation of the star caused it to elongate along the equator and flatten at the poles. The image also showed clearly the increased heat of the polar region compared with the inflated equatorial region, due to the more extended stellar material being further from the heat source of the star's core. The ALMA Partnership et al. (2015) presented a stunningly detailed image of rings and gaps within the HL Tau protoplanetary disk, achieving unprecedented angular resolution in the submillimetre regime (Figure

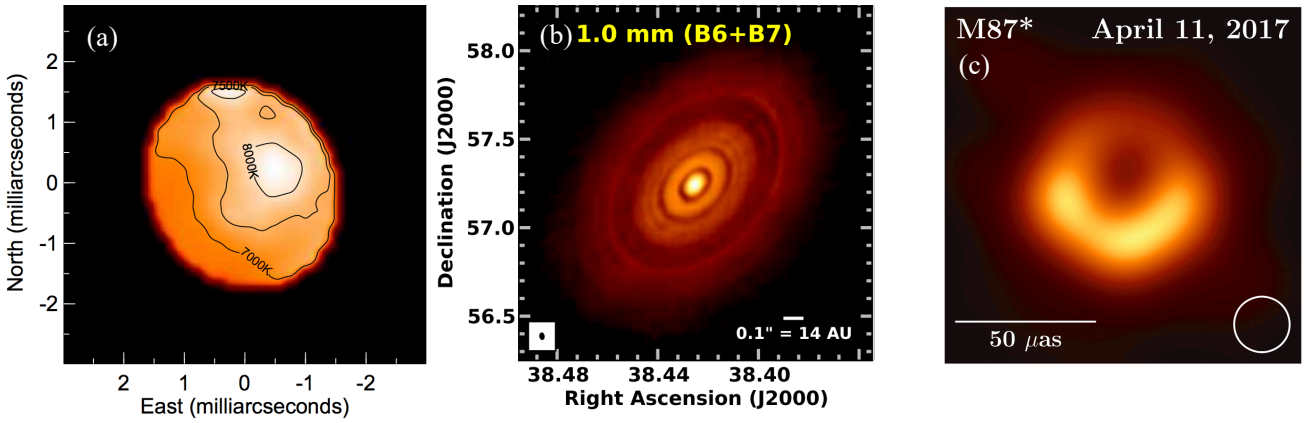

Figure 5.1.1: Panel a): Image of the surface of Altair taken from the work of Monnier et al. (2007), reconstructed from CHARA/MIRC interferometry data. The elongated shape of the star can clearly be seen, along with the increased intensity from the hot polar region. Panel b): Image of the protoplanetary disk around HL Tau made using the ALMA interferometric array (taken from ALMA Partnership et al., 2015). The ring structure of the disk has since been the subject of various theoretical models of planet formation and disk evolution. Panel c): Image of the supermassive black hole in the core of M87. This image has the highest angular resolution ever achieved in astronomy.

5.1.1, panel b). The data from the reconstructed image has since been the subject of many simulations of planet formation and disk hydrodynamics. Arguably the most remarkable advancement yet in the field of interferometric image reconstruction was presented by the Event Horizon Telescope Collaboration et al. (2019a, 2019b), who presented the first resolved image of material orbiting close to the event horizon of a black hole (Figure 5.1.1, panel c). The Event Horizon Telescope Collaboration et al. combined the light from telescopes across the globe, achieving unprecendent baseline spatial frequencies in the giga-λ regime. The image was recognised the world over as an extroardinary feat of human ingenuity. Interferometry and image reconstruction have been central to some of the most technical astronomical achievements in human history. The insights that can be achieved by analysing raw interferometric data are powerful but nothing captures the imagination as well as images of the cosmos, giving them a different kind of power.

5.2 Interferometric image reconstruction

The theory behind interferometry is laid out in this thesis in Section 3, where we discussed the Van Cittert-Zernicke theorem, the principle that the visibility observed with an interferometer is the Fourier transform of the on-sky brightness distribution. However,

deriving an image from interferometric data is more complex than simply performing an inverse Fourier transform on the observed data. Image reconstruction must be tackled as an inverse problem (Tarantola and Valette, 1982; Tarantola, 1987) by imposing prior constraints to select a unique image from all those that fit the observed data. These priors, also known as the regularisation, are selected to smoothly interpolate between the voids that are present in the *uv*-coverage (Titterington, 1985). For this reason it is imperative to sample as much of the *uv*-plane as possible, in addition to ensuring that the *uv*-coverage is as uniform as it can be. Image reconstruction is then a case of keeping the image as simple as possible whilst achieving a good fit to all of the available visibility data (Thiébaut and Young, 2017).

Image reconstruction processes such as the CLEAN algorithm (Högbom, 1974) have been successfully used for decades in the field of radio and sub-millimetre interferometry. There are many advantages to observing in this wavelength regime, such as that the telescopes that make up the interferometer are much less expensive to make and that the effects of atmospheric turbulence are much reduced at longer wavelengths. As a result, the amplitude and phase of the complex visibility can be directly measured and the *uv*-plane extensively and uniformly sampled, both being essential for a successful image reconstruction.

However, achieving image reconstruction at shorter wavelengths, such as in the infra-red, is far more challenging. Optical interferometers recombine light from far fewer elements than their radio counterparts, leading to a much sparser and less uniform coverage of the *uv*-plane. In order to collect light at optical wavelengths the telescope mirrors must be smooth to an accuracy of $\sim$20nm, which is far more difficult and expensive to achieve than the $\sim 20\mu$m required to reflect sub-mm light. The shorter wavelengths also require the positions of the telescopes to be known to a degree of accuracy that is $\sim 100\times$ higher than is required for the radio regime. The result is that optical interferometers are made up of far fewer elements (usually between 3 and 6 telescopes) than radio or sub-mm interferometers. As such, achieving a *uv*-coverage sufficient for image reconstruction takes many nights worth of observations, rather than a few hours.

At optical wavelengths, observing the phase of the complex visibility is extremely difficult, as we discuss in Section 3.2. Observables such as the closure phase only preserve some of the phase information, meaning that a significant part of the complex visibility information cannot be recovered. Without all of the phase information, image reconstruction is far more problematic than a simple inverse Fourier transform of the complex visibility function. An example of a method for image reconstruction can be found in the

work of Renard et al. (2011).

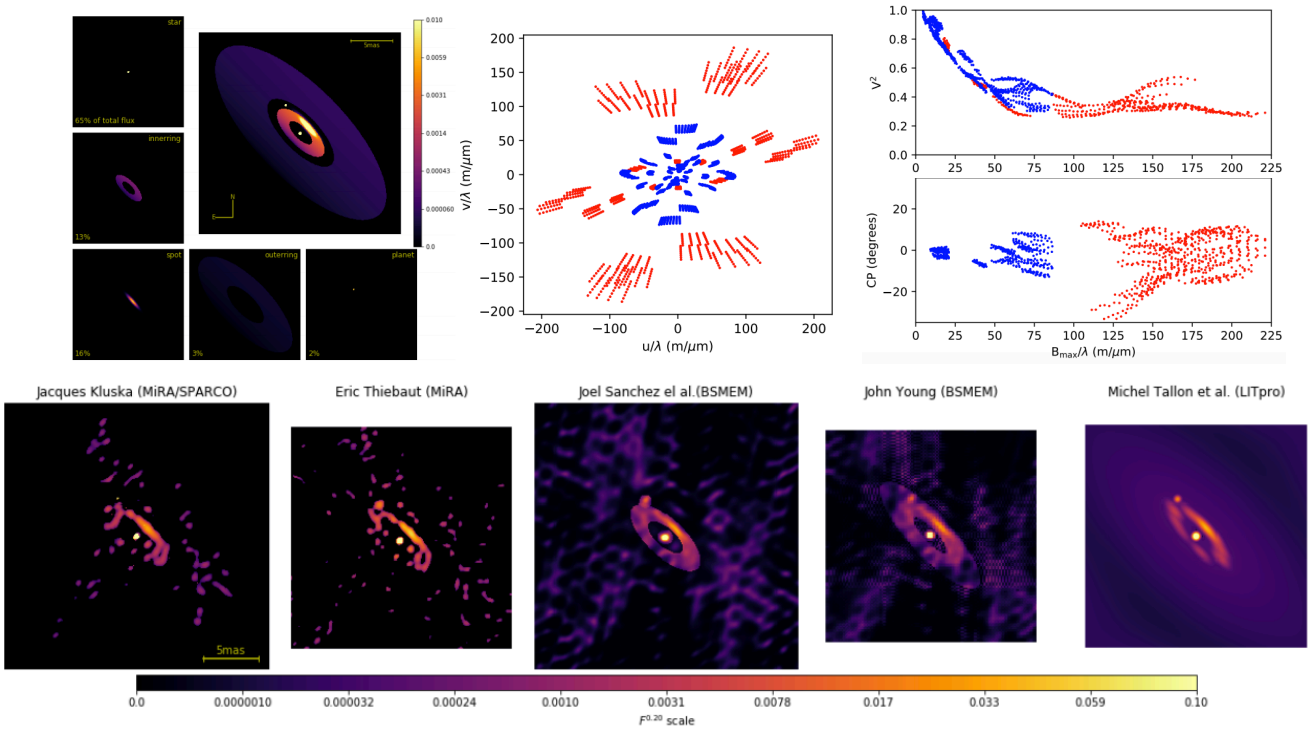

Figure 5.2.1: Figure using images from Mérand et al. (2018) illustrating the initial model and results of the 2018 optical interferometry image reconstruction contest. Top left panel: An image of the inital disk model along the various components (and relative flux ratios) that comprise it. Top middle panel: Sample VLTI+CHARA *uv*-coverage for the simulated observations. Top right panel: Simulated squared visibilities and closure phases of the disk model. Bottom row: Reconstructed images of the disk model calculated using the sample data. The team leader and reconstruction algorithm are shown above each image.

The effectiveness of various different image reconstruction codes is discussed in the 2018 optical interferometry image reconstruction contest (Mérand et al., 2018). Five different research groups were given a data set constructed using a complex disk-system model with a sample VLTI/PIONIER and CHARA/MIRC *uv*-coverage. Each group used their own image reconstruction process in an attempt to achieve an image that best matches the original model. Each of the image reconstruction approaches determines the correct location of the planet and the correct orientation of the disk. The gap between the inner and outer disks was detected at the correct location in the image reconstructions by Kluska, Thiébaut and Sanchez, whilst the inner disk was entirely resolved in the images by Sanchez, Young and Tallon. The winning image by Sanchez et al. used a novel technique of using one algorithm to construct an initial image, which was then used as a first approximation for a second image reconstruction algorithm.

5.3 Spectrally dispersed image reconstruction

More information can be revealed about dynamic astronomical processes by observing with spectrally-dispersed interferometry and using the data to reconstruct images across multiple spectral channels. This process means that the light observed is split into discrete bins, meaning that to obtain a high SNR, the observations must have longer integration times than similar observations without spectral dispersion. Such spectrally dispersed observations of protoplanetary disks in the sub-millimetre regime reveal clear signatures of Keplerian rotation (Murillo et al., 2013) and mass infall (Yen et al., 2014) along with the transition between the two kinematic scenarios (Aso et al., 2015). Mass outflow scenarios such as disk winds (Bjerkeli et al., 2016; Güdel et al., 2018) and jets (Lee et al., 2017) have also been observed in this wavelength regime for YSOs. Extraordinarily, recent ALMA observations of disks in Keplerian rotation have been used to detect the presence of forming planets. Pinte et al. (2018) was able to infer the presence of an embedded protoplanet in the disk around HD 163296 by detecting a small distortion in the otherwise perfectly Keplerian velocity field. Pinte et al. repeated the feat in 2019, observing a similar kinematic signature of an embedded protoplanet in the disk around HD 97048, at a radius perfectly in alignment with a gap detected in the continuum emission. This discovery provides more evidence of the connection between gaps in protoplanetary disks and the planet formation process, as well as revealing spectro-interferometry as an exciting new tool for detecting protoplanets. However, the millimetre and sub-millimetre wavelength regimes do not permit observers to detect the hotter dynamical processes that occur close to the central star. These mechanisms require observations at infra-red wavelengths, firmly in the realm of optical interferometry.

5.3.1 IRBis

In 2014, Hofmann et al. presented IRBis (Image Reconstruction software using the Bispectrum) an image reconstruction algorithm for optical interferometry based on the building block method described by Hofmann and Weigelt (1993). As with all image reconstruction algorithms IRBis takes raw visbility and phase data from an interferometer and aims to reconstruct the observed brightness distribution. To do this, the following steps are taken:

1. The bispectrum elements from the observed visibility and phase are derived and used as the data set from which the reconstructed image is calculated.

2. The IRBis algorithm searches for the 2D brightness distribution $o_k(\vec{x})$ with a bispectrum that best represents the observed. Here k is the iteration number and $\vec{x}$ is a 2D coordinate vector.

3. A regularisation term $H[o_k(\vec{x})]$ is introduced to mitigate the effects of the sparse *uv*-coverage that is unavoidable for optical interferometry. This term is combined with the χ^2 function, $Q[o_k(\vec{x})]$, to give the cost function $J[o_k(\vec{x})]$.

4. Minimisation of the cost function $J[o_k(\vec{x})]$ is achieved using the alternative set algorithm conjugate gradient routine (*ASA_GW*, Hager and Zhang, 2005, 2006).

The product of combining data from three telescopes is called the bispectrum, $O^{(3)}$, which can be expressed using the following relation:

$$O^{(3)}(u_1,u_2) = \sqrt{V^2(u_1)V^2(u_1+u_2)V^2(u_2)} \cdot e^{i\beta(u_1,u_2)}, \tag{5.3.1}$$

where u_1 and u_2 are 2D spatial frequency coordinates, V^2 is the squared visibility and $\beta(u_1,u_2)$ is the closure phase. The comparison between the potential best-fit images and the observed data is performed using the reduced χ^2. The χ^2 for the bispectrum is represented by the function:

$$Q_1[o_k(\vec{x})] = \int_{u_1 u_2} \frac{w_d(u_1,u_2)}{\sigma^2(u_1,u_2)} \cdot \left| \gamma_0 O_k^{(3)}(u_1,u_2) - O^{(3)}(u_1,u_2) \right|^2 \mathrm{d}u_1 \mathrm{d}u_2, \tag{5.3.2}$$

where $w_d(u_1,u_2)$ is a weighting factor accounting for the unequal distribution of *uv* points, σ is the bispectrum error and γ_0 is a scaling factor.
Sparse *uv*-coverage means that many different reconstructed images can fit the observed bispectrum with similarly small $Q_1[o_k(\vec{x})]$ values. The bispectrum of these different images may behave strangely in the holes between *uv* points (i.e. making large jumps as opposed to changing smoothly) which can be counteracted through introduction of a regularisation factor. This is acheived by defining the cost function:

$$J[o_k(\vec{x})] = Q[o_k(\vec{x})] + \mu \cdot H[o_k(\vec{x})], \tag{5.3.3}$$

where μ is the regularisation factor which determines the scale to which the regularisation function $H[o_k(\vec{x})]$ is applied. IRBis can apply a range of different regularisation functions, outlined in Section 2.2.2 of Hofmann et al. (2014). The cost function is minimised using a large-scale, non-linear, bound-constrained optimisation algorithm, *ASA_GW*. The

large-scale nature of the algorithm is manifest in the large number of pixels in the image reconstruction (between 10^4 and 10^5). It is important that the algorithm be constrained by bounds to preserve the positive value of pixels so as to avoid a non-physical best-fit image. A model image such as a Gaussian or ring that is a good fit to the data can be used as a first-guess for algorithm.

The quality of the reconstructed image is estimated by comparing the extracted visibiliy and closure phase of the image with the observed visibility and closure phase data. This comparison can be achieved by calculating the reduced χ^2 along with the residual ratio ($\rho\rho$, calculated by taking the ratio of positive and negative residuals). These two comparison quantities can be combined into the positive parameter:

$$q_{\rm rec} = \frac{1}{4}\left[|\chi^2_{V^2} - 1| + |\rho\rho_{V^2} - 1| + |\chi^2_{\rm CP} - 1| + |\rho\rho_{\rm CP} - 1|\right] \tag{5.3.4}$$

A good image reconstruction should have a $q_{\rm rec}$ value close to zero. To avoid noise-fitting, in the case that the χ^2 is lower than one the reciprocal $1/\chi^2$ is used. The output image from the reconstruction algorithm is convolved with the beam of the simulated *uv*-coverage.

An example of the successful application of the IRBis method to construct spectrally dispersed images is shown in the work of Weigelt et al. (2016) (Figure 5.3.1). Here Weigelt et al. made use of the differential phase data from AMBER in their image reconstruction as well as the closure phase. Using the wavelength-differential phase, and the known continuum phase, the Fourier phase of the object's brightness distribution could be derived across multiple wavelength channels. This method of using the Fourier phases derived from the differential phases and wavelength dependent visibilities is referred to as the differential phase method. Weigelt et al. observed the luminous blue variable (LBV) star η Car with AMBER's high spectral dispersion mode using the ATs. η Car has a strong ($\sim$250% continuum strength) and wide ($\pm\sim$750kms^{-1}) Brγ emission line, allowing Weigelt et al. to obtain velocity resolved images across over 100 spectral channels. For the first time, the velocity resolved images showed that the wind from η Car is strongly wavelength dependent and asymmetric.

5.4 Chapter summary

In this chapter I have given an overview of how interferometric data can be directly interpreted by reconstructing images with unprecedented angular resolution. The results of several previous studies using image reconstruction were discussed which illustrate how

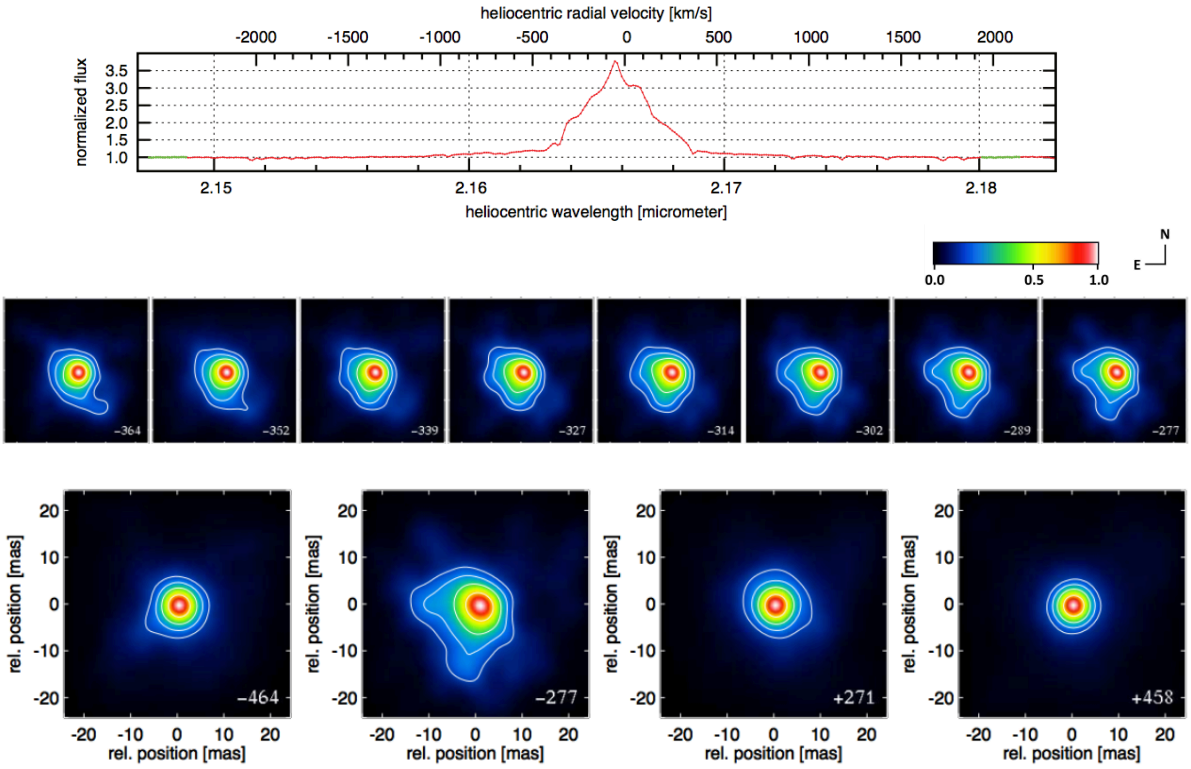

Figure 5.3.1: Figure from Weigelt et al. (2016) showing the results of velocity resolved image reconstruction of η Car using IRBis. The top panel shows the wavelength-dependent intensity of the Brγ emission line. The middle row shows the fine wavelength-dependent structure in the blue-shifted section of the line, showing the presence of fan- and bar-like structures in the line-emitting material. The bottom row shows the difference between the red-shifted and blue-shifted material at a range of velocities.

such high-angular resolution images can be used to further our collective knowledge of astrophysics. I have described how the image reconstruction process is approached as an inverse problem that is made simpler with a more extensive sampling of the *uv*-plane. Spectrally dispersed image reconstruction has been succesfully achieved in the sub-mm and radio regimes, but it is more challenging for optical wavelengths as it is more difficult to obtain a *uv*-coverage that is sufficient. I have outlined the previous results of spectro-interferometric image reconstruction in both the long and short wavelength regimes for young stellar objects. Finally, I have given a brief mathematical overview of the IRBis method for image reconstruction which is used for spectro-interferometry data in this thesis. I have included a discussion of the work by Weigelt et al. (2016), in which the IRBis method is used to reconstruct wavelength dependent images of η Car.

Chapter 6

Gas dynamics in the inner few AU around the Herbig B[e] star MWC297.

This chapter is based on a paper that was published by Hone et al. (2017) in Astronomy & Astrophysics Volume 607 (Article 17).

6.1 Introduction

As MWC297 has such a bright K-band flux it has been used as an effective back-up target for interferometric observations. This means that by the start of my PhD in 2015 our team had built a substantial spectro-interferometric data-set for the object, comprising of nine separate observations. These observations cover the widest possible range of angles and baselines that is possible using the VLT UTs, making it the largest high-spectral dispersion interferometric data set ever assembled for a young stellar object. Such an extensive data set presents a unique opportunity to study an enigmatic YSO with unprecedented detail. We were able to achieve spectrally-dispersed image reconstruction acros the Brγ line of a YSO for the first time ever, an achievement that represents a significant step forward in the fields of star formation and interferometry.

In this Chapter the Brγ line of MWC297 is spatially and spectrally resolved and the distribution and kinematics of the line-emitting gas are studied in order to place physical constraints on the processes traced by Brγ. In Section 6.2 I present AMBER spectro-interferometry and CRIRES spectro-astrometric observations which are interpreted in Section 6.3 by fitting the visibilities with geometric models and in Section 6.4 by mea-

suring the 2D photocentre displacements across the Brγ line. The fitting of low-spectral dispersion AMBER data was performed by Alex Kreplin using his own geometric model fitting scripts. In Section 6.6 I present the results of spectrally dispersed image reconstruction of MWC297 that was performed by Karl-Heinz Hofmann and the team around Gerd Weigelt at the Max Planck Institute for Radio Astronomy in Bonn. In Section 6.7 I present kinematic models of both Keplerian rotation and a magneto-centrifugally driven disk wind and compare the models to the observed data.
I was able to distinguish between two subtly different velocity fields to deduce that the Bγ emitting gas traces an extended disk wind. The subtle differences between the Keplerian rotation and disk wind velocity fields are explored in Section 6.8, with the results indicating that the perceived angle of rotation is a useful diagnostic for the presence of outflowing material. This finding in particular is the basis for a significant portion of the analysis presented in Chapter 7.

6.1.1 Earlier studies of MWC297

MWC297 is one of the nearest Herbig stars, with a mass of $\sim 10 M_{\odot}$, spectral type B1.5V and a distance of 170 pc (Fairlamb et al., 2015). Spectroscopic observations by Drew et al. (1997) indicate that MWC297 is rapidly rotating with $v \sin i = 350 \pm 50\,\mathrm{kms}^{-1}$. Stellar rotation becomes critical when $v = v_{crit} = \sqrt{2GM_*/(3R_*)}$ (Maeder and Meynet, 2000) which for MWC297 is $450 \pm 50\,\mathrm{kms}^{-1}$ (assuming $R_* = 6 R_{\odot}$ and $M_* = 10 M_{\odot}$, Drew et al. 1997; Weigelt et al. 2011). Assuming that the disk and star are aligned, this rapid rotation is called into question by the interferometric observations of the disk inclination, which was determined to be $\sim 20^{\circ}$ by Malbet et al. (2007), Acke et al. (2008) and Weigelt et al. (2011). With these parameters, v takes the value $\sim 1023\,\mathrm{kms}^{-1}$ which far exceeds the $450\,\mathrm{kms}^{-1}$ break up velocity. This 'unphysical' result could point to a possible misalignment between the star and the disk.
Important insights into the au-scale geometry of the disk around MWC297 have been obtained with near- and mid-infrared interferometry (Malbet et al., 2007; Acke et al., 2008; Kraus et al., 2008a; Weigelt et al., 2011). An interesting recurring result from these works is that the observed continuum radius is much smaller than the predicted dust sublimation radius of $\sim 3\,\mathrm{au}$ (assuming a dust sublimation temperature for silicate grains of $T_{\mathrm{sub}} = 2000\,\mathrm{K}$). This characteristic has also been found in other luminous objects, including Z CMa and V1685 Cyg (Monnier et al., 2005). Like MWC297 (B1), both of these objects are early-type B stars (Z CMa: B0, van den Ancker et al. 2004; V1685 Cyg: B3, Hernández et al. 2004), indicating that this could be characteristic for young, luminous

Herbig Be stars.
MWC297 was also resolved with VLTI/PIONIER in the H-band by Lazareff et al. (2017). They fitted Gaussian-modulated ring models to their visibility and closure phase data but could not find any evidence for a sharp inner edge around MWC297. Instead, the measured visibility profile is very smooth and indicated a Gaussian-like profile with the system axis along a position angle (PA) of $13.7 \pm 1.7^{\circ}$, which is consistent with our PA estimate within 0.88σ. The morphology of the near-infrared continuum varies for different objects, with lower-mass Herbig Ae stars showing a ring shape (tracing the inner dust rim) and the higher-mass Herbig Be stars having a more radially extended ring structure, sometimes leading to Gaussian-shaped continuum emission (Lazareff et al., 2017). MWC297 displays an intriguing continuum geometry with the NIR emission well inside the dust sublimation radius and no "hole" in the emission indicative of a ring-like structure. The variation of optical depth in the inner gas disk was investigated by Muzerolle et al. (2004), who found that for high accretion rates ($\dot{M} \gtrsim 10^{-8}$ $M_{\odot}yr^{-1}$) the inflowing gas can become optically thick. Further study of the accretion rate and gas opacity in the inner disk is beyond the scope of this study.
Spectrally dispersed interferometry with VLTI/AMBER offers a unique opportunity to observe wavelength-dependent changes in the object morphology at medium spectral resolution ($R = 1\ 500$) or the kinematics of line-emitting gas at high spectral resolution ($R = 12\ 000$), retaining the extremely high angular resolution achieved with optical interferometry. This technique was employed by both Malbet et al. (2007) and Weigelt et al. (2011) to observe the Brγ emission line of MWC297. Malbet et al. (2007) interpreted their single baseline $R = 1\ 500$ data with a model comprised of two codes: one simulating an optically thick, continuum-emitting disk around MWC297, and the other modelling the source of the line emission as a stellar wind from the central star. Their model provides a good fit to the observed spectral energy distribution (SED), differential visibility and Brγ spectrum, but with no differential phase measurements and a very small sample of data (just one baseline), the gas kinematics are not well constrained. In addition, they assumed a double-peaked Brγ line profile for their kinematic modelling, while a later reanalysis of the same ISAAC data set showed that the double-peaked profile was a calibration artifact and that the line profile is single-peaked (Kraus et al., 2008a).
Weigelt et al. (2011) developed a more complex kinematic model which included a continuum-emitting ring with an extended disk wind component contributing to the Brγ line emission. The geometry of the disk wind component of their model is similar to that detailed in the work of Kurosawa et al. (2006) with the parameterisation of mass-loss and accel-

eration detailed further in Weigelt et al. (2011). The shape of the differential visibilities and phases from the model are a good match to the observed quantities, but there are significant residuals between the model and the data which leaves room for further study into the object with similar techniques. The data set that they modelled contained only a small range of short baselines (14 to 42m) along a linear configuration with a position angle of 68°, which is insufficient to constrain the two-dimensional (2D) geometry of the line-emitting region.

6.2 Observations and data reduction

6.2.1 VLTI/AMBER spectro-interferometry

We observed MWC297 between 2008 and 2012 with ESO's Very Large Telescope Interferometer (VLTI) and its beam combination instrument AMBER (Petrov et al., 2007). Our VLTI/AMBER observations are outlined in Table 6.2.1 and the *uv*-coverage of these observations is shown in Fig. 6.2.1. The data set that we present contains the three baselines from the linear configuration of Weigelt et al. (2011) obtained with the 1.8 m Auxiliary Telescopes (ATs) along a PA of 67° but we improve on this *uv*-coverage by adding nine additional observations with the 8.2 m Unit Telescopes (UTs). Our additional AMBER data contains baselines with position angles ranging from ∼10° to ∼130° and the full possible range of deprojected baseline lengths achievable with the UTs (30-132 m). In order to improve the signal-to-noise ratio (SNR), we employed the fringe-tracking instrument FINITO (Gai et al., 2004; Le Bouquin et al., 2008). The use of long integration times (up to 8000 ms) improves the SNR on the wavelength-differential observables, but can also bias the absolute visibility calibration. Therefore, we calibrate the continuum visibility level using low-spectral-resolution AMBER data. Each science observation of MWC297 was accompanied by a calibrator observation, with the targets HD175583, HD187660, HD166460, HD152040 and HD164259 used as interferometric calibrators (detailed in Table 6.2.1). The data was reduced with the AMBER data-processing software package, which uses the pixel-to-visibility matrix algorithm P2VM (Tatulli et al., 2007; Chelli et al., 2009) in order to extract visibilities, differential phases, and closure phases for each spectral channel of an AMBER interferogram. We adopt heliocentric line-of-sight velocities for each observation using the ESO Airmass tool.

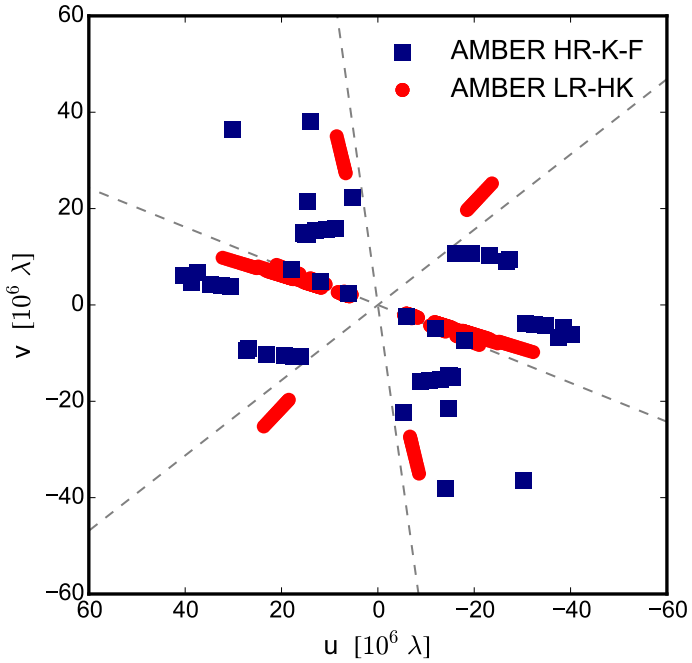

Figure 6.2.1: *uv*-coverage achieved with our VLTI/AMBER interferometric observations of MWC297 for both $R = 30$ (red circles) and $R = 12\,000$ (blue squares) spectral resolutions. The gray dashed lines indicate the slit orientations for our CRIRES spectro-astrometric observations.

6.2.2 VLT/CRIRES spectro-astrometry

We complement our AMBER spectro-interferometric data with observations taken with the CRIRES spectrograph at the VLT (Kaeufl et al., 2004). The observation details are outlined in Table 6.2.1. Spectro-astrometry uses long slit spectra to measure the wavelength-dependent centroid offset of an unresolved object with respect to the continuum. Whilst this does not let us formally resolve the object spatially, it offers extremely high spectral resolution of $R = 100\,000$, meaning that we can spectrally resolve the detailed structure in the Brγ line profile. The centroid position can be measured with much higher precision than the size of the point-spread-function (PSF), allowing us to measure the small-scale photocentre displacements characteristic of the kinematics in the inner disk. By measuring the centroid offset along three slits oriented at position angle offsets of 60° we can derive 2D photocentre displacement vectors. We chose to observe with slits oriented at PAs of 8°, 68°, and 128° (and their corresponding anti-parallel PAs 188°, 248° and 308°), in order to complement the interferometric observations published by Weigelt et al. (2011) that were obtained along a baseline PA of 68°. Our CRIRES observations were obtained on 2009 September 12 using an integration time of 1.5s and a slit width of

Table 6.2.1: Observation log for our MWC297 data taken with VLTI/AMBER and VLT/CRIRES.

Instrument	Date	Telescopes	UT	DIT	NDIT	Proj. baselines	PA	Calibrator	UD diam.
			[h:m]	[ms]	#	[m]	[○]		[mas]
AMBER	2008-04-06	H0/G0/E0	08:14	8000	100	14.0 / 28.0 / 42.0	247.9 / 247.9 / 247.9	HD175583	1.00 ± 0.10
HR-K	2009-05-13	U2/U3/U4	10:01	200	1200	46.0 / 48.0 / 75.8	45.9 / 118.5 / 83.1	HD187660	1.85 ± 0.19
"	2009-06-13	U2/U3/U4	04:15	1000	560	41.0 / 61.1 / 82.2	34.0 / 108.5 / 79.7	HD166460	1.54 ± 0.15
"	"	U2/U3/U4	08:22	3000	125	44.5 / 45.4 / 71.0	121.3 / 45.5 / 83.0	HD187660	1.85 ± 0.19
"	"	U2/U3/U4	08:38	500	600	41.9 / 44.9 / 67.1	123.8 / 45.1 / 82.9	HD187660	1.85 ± 0.19
"	2009-08-03	U2/U3/U4	03:46	3000	200	46.6 / 54.9 / 84.3	45.8 / 113.9 / 83.0	HD166460	1.54 ± 0.15
"	2012-04-03	U1/U2/U3	08:19	500	840	39.1 / 49.4 / 87.7	28.8 / 13.1 / 20.0	HD152040	0.57 ± 0.06
"	2012-05-04	U1/U2/U3	10:02	400	1200	46.5 / 56.4 / 102.4	46.0 / 34.3 / 39.6	HD166460	1.54 ± 0.15
"	2012-06-01	U2/U3/U4	05:57	500	960	43.9 / 62.4 / 88.3	220.0 / 109.0 / 81.4	HD152040	0.57 ± 0.06
AMBER	2007-04-14	H0/G0/E0	08:09	50	5000	28.2 / 42.2 / 14.1	68.1 / 68.1 / 68.1	HD166460	1.54 ± 0.15
LR-K	2007-06-19	H0/G0/E0	07:10	50	5000	30.1 / 45.2 / 15.1	73.1 / 73.1 / 73.1	HD166460	1.54 ± 0.15
"	2007-09-01	H0/G0/E0	00:46	100	10000	31.9 / 47.9 / 16.0	72.5 / 72.5 / 72.5	HD172051	0.64 ± 0.06
"	2007-09-02	H0/G0/E0	00:23	100	2500	31.7 / 47.6 / 15.9	72.1 / 72.1 / 72.1	HD160213	0.15 ± 0.01
"	"	H0/G0/E0	00:36	50	5000	31.9 / 47.9 / 16.0	72.4 / 72.4 / 72.4	HD160213	0.15 ± 0.01
"	2008-06-03	H0/G0/E0	08:18	50	15000	29.7 / 44.6 / 14.9	73.0 / 73.0 / 73.0	HD177756	0.51 ± 0.05
"	2009-05-16	G1/D0/H0	08:21	100	5000	64.8 / 68.1 / 63.4	137.3 / 14.2 / 73.1	HD166460	1.54 ± 0.15
CRIRES	2009-09-12	UT1	01:43	1500	1500	N/A	8.0 / 68.0 / 128.0	HD165185	0.56 ± 0.06

0.197".

To derive the differential phase signal from our CRIRES observations, in order to later model our AMBER and CRIRES data simultaneously, we follow the method outlined by Kraus et al. (2012b). This method makes use of the fact that the centroid shifts $X(v)$ that we calculate above are mathematically equivalent to the differential phase signals that we measure using spectro-interferometry at very short baseline lengths. We employ the equation $\phi(v) = -\frac{2\pi X(v)}{\sigma}$ to determine the differential phase $\phi(v)$ from the observed centroid shifts $X(v)$ for each spectral channel v, where σ is the full-width at half-maximum (FWHM) of the PSF measured in the spectrum.

6.3 Geometric modelling

6.3.1 AMBER LR-K continuum visibilities

To measure the characteristic size and morphology of the near-infrared continuum disk around MWC297 I fitted a 2D geometric model to our low-spectral resolution (R=30) AMBER K-band observations. These observations are outlined in Table 6.2.1 and provide a good coverage towards position angles 14°, 137°, and a range between 68° and 73° (Fig. 6.2.1, red data points). We fit a 2D geometric model of an elongated Gaussian brightness distribution to the data. Our best-fit model parameters indicate a FWHM size of 4.9 ± 0.1 mas with the minor axis (later referred to as the 'system axis') along position angle of $9.6° \pm 4.8°$. We find that the FWHM sizes of the minor and major axes are 5.3 ± 0.1 mas and 4.5 ± 0.1 mas respectively, corresponding to an inclination of $32° \pm 3°$. This derived continuum size is larger than the results derived by Acke et al. (2008) and Weigelt et al. (2011), who measured characteristic continuum FWHM sizes of $\sim$4.3 mas and $\sim$4.6 mas, respectively. Additionally, the inclination measurements are in agreement with the tentative disk inclination of $\sim$20° with an upper limit of 40° determined by Acke et al. (2008). Below we use the orientation and basic geometry of the continuum disk to compare with the distribution of the line-emitting gas.

6.3.2 AMBER HR-K line visibilities

Observing with high-spectral-resolution interferometry allows us to obtain visibility information for individual spectral channels across the Brγ line, thus constraining the spatial distribution of the line-emitting gas. The differential visibility signatures show a strong

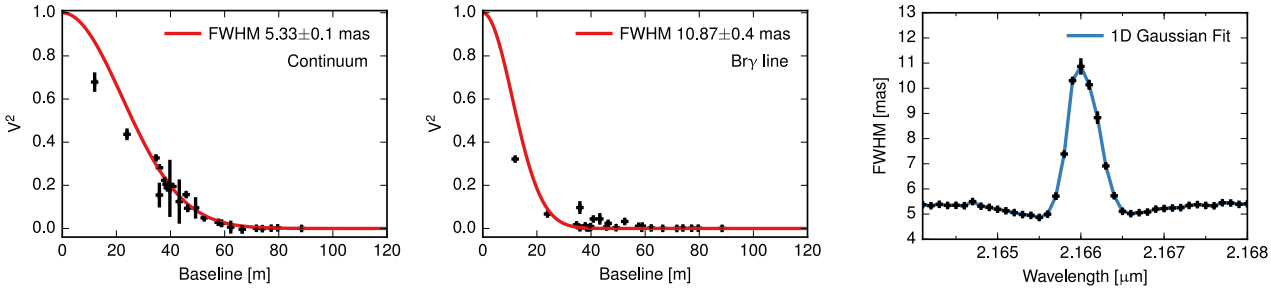

Figure 6.3.1: Left: Results of our 1D Gaussian model fit to deprojected visibilities for continuum channels (Error rounded up to 0.1mas). Middle: Results of our 1D Gaussian model fit to deprojected visibilities for the central channel in the Brγ line. Right: Wavelength-dependent 1D Gaussian fit FWHM diameters for each channel across the Brγ line.

decrease in the line, indicating that the line-emitting region is more extended than the continuum, and so we apply our geometric modelling code to fit the de-projected visibilities channel-by-channel across the Brγ line, using the relation from (Berger and Segransan, 2007):

$$r_{uv\theta i} = \sqrt{u_\theta^2 + v_\theta^2 \cos(i)^2}, \tag{6.3.1}$$

where u_θ and v_θ are the spatial co-ordinates of the baseline vector, θ is the disk PA, and i is the disk inclination.

By applying this transformation for all spectral channels we take the approximation that the line emission is seen under the same inclination as the continuum emission. We apply this de-projection to our baseline vectors, adopting the position angle and inclination values of 9.6° and 32° determined from modelling our AMBER LR data (Sect. 6.3.1). The differential visibility data is then split by wavelength in order to derive the baseline-dependent visibilities for each spectral channel. We fit a simple 1D Gaussian model to the deprojected baseline-dependent visibility data across the Brγ line and determine the wavelength-dependent FWHM of the line-emitting region (Figure 6.3.1, centre panel). There is a clear size increase detected up to a peak FWHM size of 10.87±0.4 mas in the line centre (see Figure 6.3.1, right panel), similar to the wavelength-dependent size profile shown in Weigelt et al. (2011), where the line-emitting region was observed to increase in size towards the line centre to a peak FWHM size of 12.61 mas.

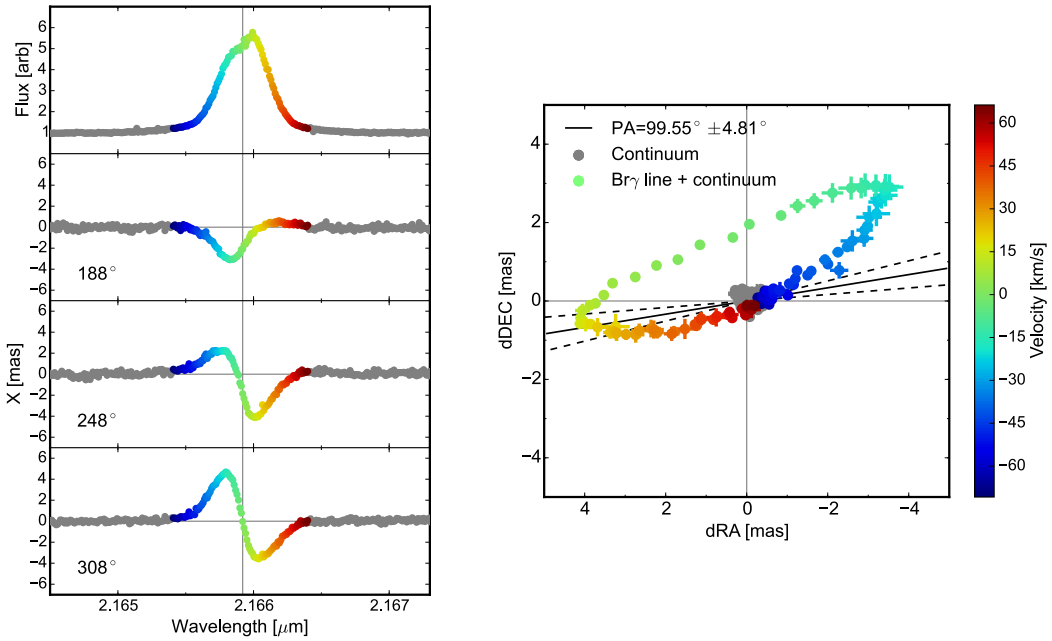

Figure 6.4.1: Left: VLT/CRIRES high-resolution ($R = 100\ 000$) Brγ spectrum (top panel) and centroid displacements of the Brγ-emitting region (lower panels) for MWC297. The position angle of each slit is shown to the left of each phase panel. Right: Derived 2D photocentre displacement vectors of the Brγ + continuum emission for MWC297. The black line shows the position angle of the disk major axis determined from our AMBER LR observations.

6.4 Photocentre analysis

6.4.1 CRIRES spectro-astrometry

CRIRES spectro-astrometry allows us to directly measure centroid displacements between spectral channels at very high spectral resolution with high SNR, making it a powerful tool for determining the nature of the kinematics traced in spectral lines. We calculate the photocentre displacement vectors ($\vec{p}$) from our CRIRES spectro-astrometric data by combining the spectro-astrometric signal for each of our three observed slit vectors (corresponding to the baseline vectors B_i) and finding the best-fit photocentre vector using the Nelder-Mead simplex algorithm (as described in Kraus et al., 2012b). Using this method we obtain the series of wavelength-dependent photocentre displacement vectors of the combined continuum and line emission shown in Figure 6.4.1 (right panel).

The derived photocentre vectors show an offset between the red-shifted and blue-shifted vectors along a position angle of $114 \pm 3°$. The photocentres of the higher-velocity channels are less displaced from the continuum emission than the lower-velocity channels,

indicative of a rotational field where the velocity decreases with radius, such as Keplerian rotation. An alternative explanation for this could be due to the fact that the photocentres contain both line and continuum emission, meaning that channels with less line flux are weighted to trace the continuum emission more closely. I fitted a linear function to these photocentre displacement vectors in order to determine the axis along which the blue and red-shifted lines are displaced. We determine that this "axis of motion" is oriented along PA $114^\circ \pm 3^\circ$, which differs from the PA of the disk major axis of $99.6^\circ \pm 4.8^\circ$ determined from our AMBER-LR observations. The photocentre shifts for the whole line exhibit an interesting arc pattern, with the vectors becoming more displaced to North as they approach the line centre. It is possible that this pattern is caused by obscuration of the further regions of the disk shifting the photocentre vectors towards the observer, an idea that we explore further in Sect. 6.7 as part of our modelling of the disk kinematics.
Our very-high-spectral-resolution data taken with the VLT/CRIRES instrument (Figure 6.4.1) show that the Brγ line from MWC297 is single-peaked. Some small asymmetries seen in the CRIRES Brγ line profile are consistent with the line profiles shown for a disk wind at low inclinations in the work of Tambovtseva et al. (2016). We do not detect any variability in the shape or intensity of the Brγ line across the different epochs of our VLTI/AMBER data set.

6.5 AMBER spectro-interferometry

Measuring differential phases allows us to gain unique insight into small-scale spatial displacements between spectral channels. These displacements are a very powerful diagnostic for the gas kinematics at scales of just a few stellar radii. Initially we calculate the photocentre displacement vectors $\vec{p}$ (of both the continuum and line-emitting region with respect to the continuum centre) from our AMBER differential phase measurements by solving the following set of 2D equations:

$$\vec{p} = -\frac{\phi_i}{2\pi} \cdot \frac{\lambda}{\vec{B}_i}, \tag{6.5.1}$$

where ϕ_i is the differential phase measured for the ith baseline, $\vec{B}_i$ is the corresponding baseline vector, and λ is the central wavelength (Lachaume, 2003; Le Bouquin et al., 2009).
We simultaneously use the data of many baseline vectors by combining the differential phases and baseline vectors for each spectral channel and applying the Nelder-Mead simplex algorithm to find the best-fit photocentre vector using Equation 6.5.1. However, it

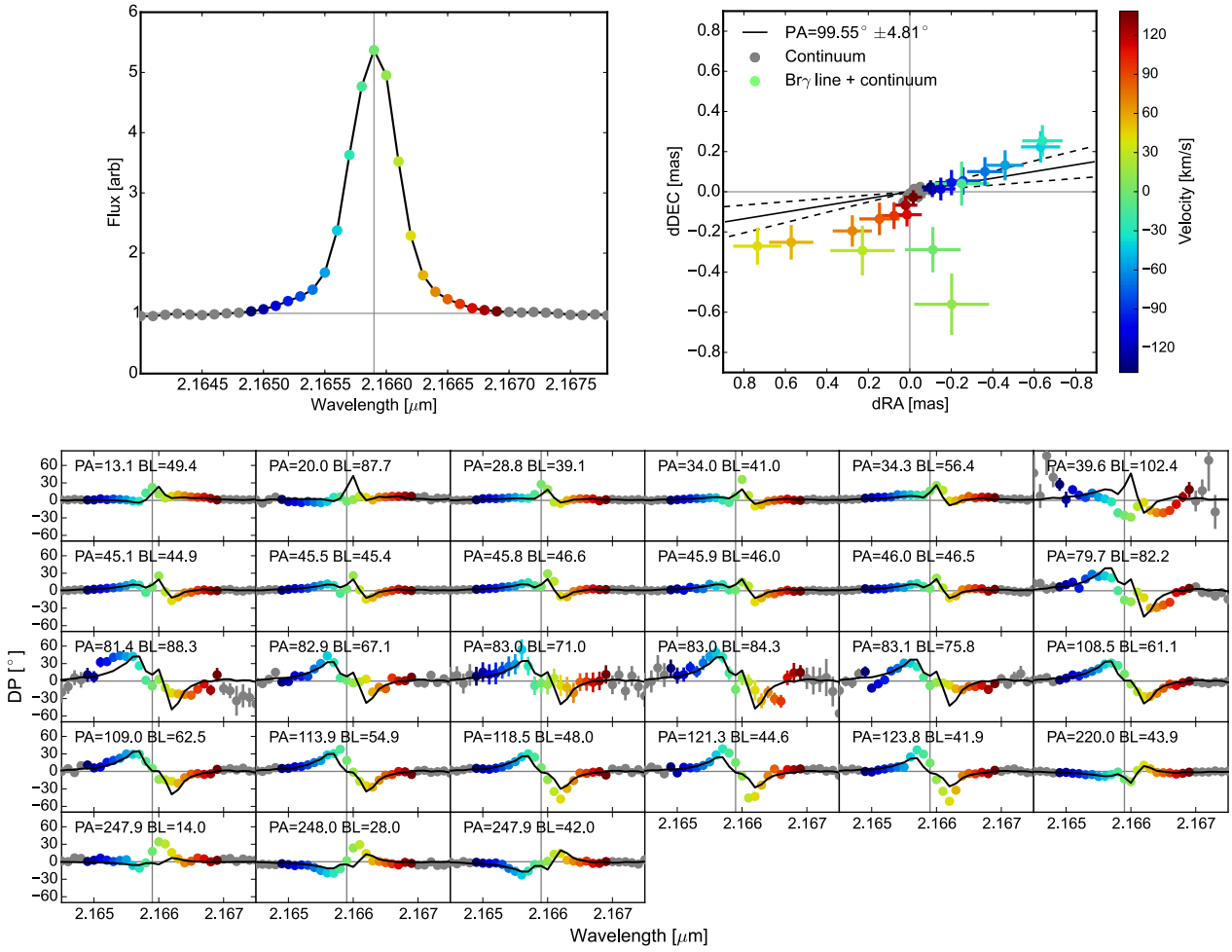

Figure 6.5.1: Upper left panel: K-band spectrum of MWC297 measured with AMBER, averaged across all baselines. Upper right panel: Derived 2D photocentre displacement vectors for the Brγ line + continuum determined from our AMBER HR-K data. The black line shows the position angle of the disk major axis determined from our AMBER LR observations. Lower panel: Differential phases for MWC297 observed with AMBER (circular points) compared with differential phases corresponding to the photocentre shifts shown in the upper right panel of this Figure (black lines). The frame with PA=39.6°, BL=102.4m is offset by 180° in order to see the differential phase changes at the Brγ line centre.

is worth noting that Eq. 6.5.1 is derived for marginally resolved objects. Our AMBER data formally resolve the line-emitting region of MWC297 and therefore we note that the photocentre assumption might not provide an adequate approximation, in particular in the line centre, as is discussed at the end of this Section. The grey continuum photocentre points trace the location of the central star.

The derived photocentre shifts obtained from our AMBER data are shown in Figure 6.5.1 (upper right panel). Using the same method as for our CRIRES data we determine the axis of motion of our AMBER photocentres to be along a position angle of $112 \pm 10°$, with red-shifted vectors to the south-east of the continuum and blue-shifted vectors to the north-west. The axis of motion PA values for CRIRES ($114 \pm 3°$) and AMBER ($112 \pm 10°$) are consistent with each other so we adopt the CRIRES value, with smaller uncertainties, as our best estimate for the motion angle. The PA of the axis of motion is similar to, but not fully consistent with, the PA of the disk major axis of $99.6° \pm 4.8°$ from our AMBER-LR observations (Sect. 6.3.1). The combined continuum and line photocentre vectors of the line wings (indicative of faster circumstellar material) are less displaced than those closer to the line centre, suggesting that the closer-in circumstellar material is orbiting the star at a higher velocity than the material at large stellocentric radii. This is consistent with the paradigm of a simple Keplerian-rotating disk or a disk wind.

The photocentre shifts for the lower-velocity, red-shifted channels ($\lesssim 90$ km/s) show an interesting arc-like structure with the channels closer to the line centre more displaced to North of the disk plane. This does not apply for the line centre (with $|v| \lesssim 10$ km/s) where the photocentre vectors are displaced to South of the disk plane. A similar arc-like structure was reported by Kraus et al. (2012b) for the Herbig B[e] star V921 Sco and was interpreted to result from opacity effects similar to those that we suspect cause the arc structure seen in the CRIRES photocentre vectors (Figure 6.4.1).

The scenario outlined above can explain the arc structures seen in the line wings, but cannot account for systematic displacement in southern direction that we see in the lowest-velocity channels ($|v| \lesssim 10$ km/s; light-green points in Figure 6.5.1) and that is not observed in the CRIRES photocentres. We observe this effect only in the three line channels in the very centre of the line, where the line-emitting region is most extended (see Figure 6.3.1, right panel). In these channels, the line-emitting region is strongly resolved (with visibilities of a few per cent) and the approximation in Eq. 6.5.1 is likely not applicable anymore. Therefore, we believe that the systematic displacement observed in these channels is an artifact, indicating that the geometry of the line-emitting region is too resolved to be reasonably represented by a simple photocentre displacement. This conclusion is

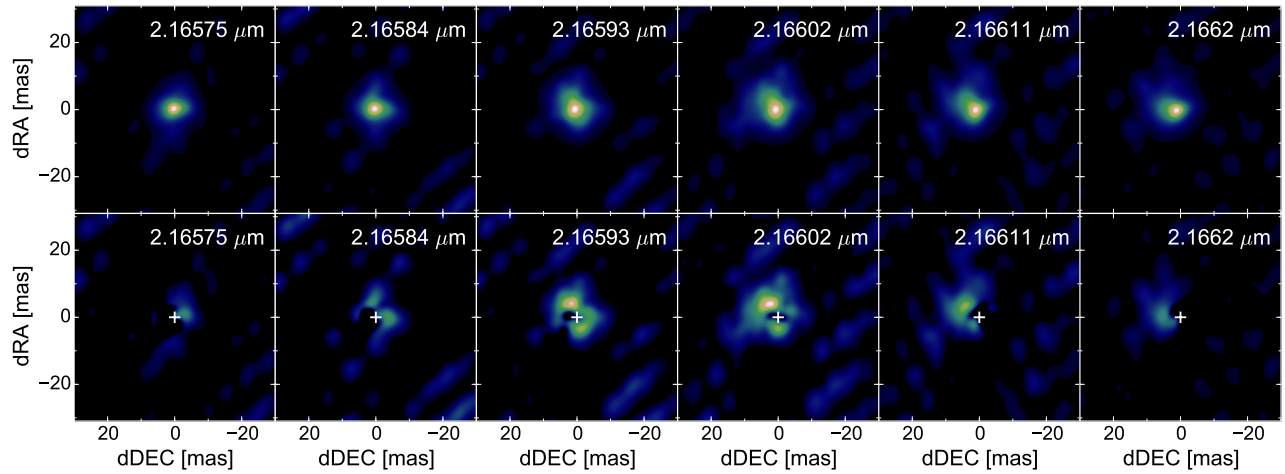

Figure 6.6.1: Velocity-resolved aperture synthesis images of MWC297 calculated by applying the *IRBis* software to our AMBER HR-K data. The raw images are shown in the upper panels and the continuum-corrected images are shown in the lower panels. The corresponding wavelength for each spectral channel is shown in the upper right corner of each image and the location of the continuum centre is marked as a white cross in the continuum-corrected images.

also supported by the lower panel shown in Figure 6.5.1, where we compare the differential phases that correspond to the photocentre displacement model (black line) with the actual measurements and where we observe significant residuals in the line centre.

6.6 Velocity-resolved image reconstruction

Interferometric imaging is a useful way to gain a model-independent representation of the brightness distribution. Spectrally dispersed interferometry enables us to obtain such images in multiple spectral channels, revealing wavelength-dependent differences due to gas kinematics. Velocity-resolved images in infrared line tracers such as Brγ have already been obtained for a supergiant A[e] star (Millour et al., 2011) and a Luminous Blue Variable (Weigelt et al., 2016; GRAVITY Collaboration et al., 2017). Here, we apply this method to obtain the first velocity-resolved images for a young star at infrared wavelengths. We use the *IRBis* method for image reconstruction (Hofmann et al., 2014) in order to reconstruct images for each channel across the Brγ line, using the differential-phase method outlined in Millour et al. (2011) and Weigelt et al. (2016, Sect. 2). The obtained images were convolved with the point-spread function of a single-dish telescope with a diameter which is twice the length of the longest baseline in our *uv*-plane. We see that the brightness distribution clearly changes with wavelength in our image cube, reflecting

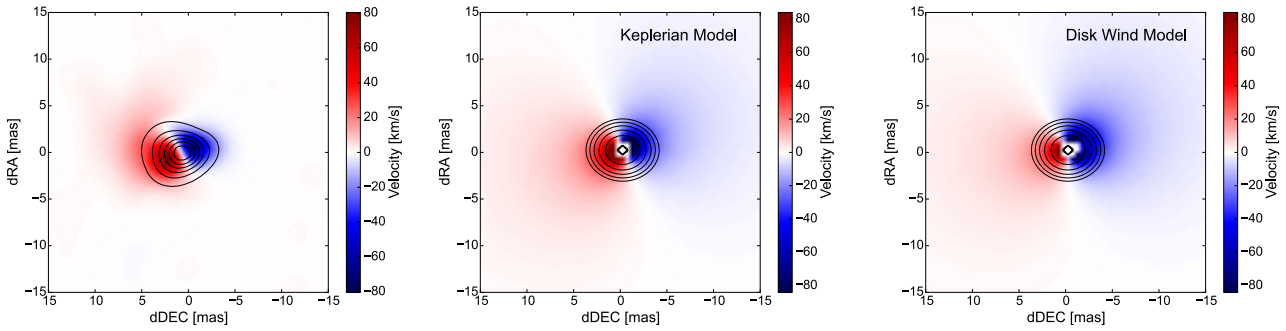

Figure 6.6.2: Left panel: First moment map for the Brγ line computed from our MWC297 AMBER images (shown in Figure 6.6.1, upper panel). Black contours show the continuum emission region. Middle panel: First moment map constructed from the frames of our Keplerian disk model. Right panel: First moment map constructed from the frames of our disk wind model.

the strong signals detected in the wavelength-differential visibilities and phases across the Brγ line. Comparing the images at different velocity channels (Figure 6.6.1) we see that the line emission is clearly more extended in the two central channels (2.16593μm and 2.16602μm) than in the high-velocity channels (2.16575μm and 2.1662μm).

In order to display the geometry of the line-emitting region with better contrast, we normalize the flux level of each image equal to the corresponding flux from the AMBER spectrum and then subtract the continuum intensity distribution, with the results shown in Figure 6.6.1 (lower panel). Examining the continuum-subtracted images we can see that the morphology of the line-emitting region changes significantly across the Brγ line. In the highest-velocity channels (wavelengths of 2.16575μm and 2.1662μm, $25 \lesssim |v| \lesssim 37$ km/s) the emission is displaced to the West (right) in the blue-shifted line channels and to the East (left) for the red-shifted channel. In the channels with intermediate velocity (2.16584μm and 2.16611μm, corresponding to $12 \lesssim |v| \lesssim 25$ km/s) the material is more extended, but still displaced in the same direction as in the lower-velocity channels. Additionally the shape of the brightness distribution changes from a single-lobed structure at the highest velocities (2.16575μm and 2.1662μm) to a double-lobed structure with two brightness peaks at intermediate velocities, one lobe further to the North and one further to the South (seen most clearly in the 2.16584μm channel). The line-emitting region is most extended in the line centre and most compact in the line wings. At these lowest-velocity channels (2.16593μm and 2.16602μm, $|v| \lesssim 12$ km/s) the brightness distribution shows an extended ring-like structure, with a more pronounced northern lobe than southern lobe. This can be viewed as a continuation of the previously discussed double-lobed structure where the brightness distribution is now more extended

to the North and South than in the East-West direction.
To further study the kinematics, we construct a first moment map from our image cube, where we compute the first moment coordinate value M_1 with

$$M_1 = \frac{\sum I_i v_i}{v_{\rm norm}}, \tag{6.6.1}$$

where I_i is the pixel value, v_i is the velocity of the image frame relative to the line centre and $v_{\rm norm}$ is a factor that normalizes the maximum absolute value of M_1 to the total width of the image cube in velocity space. The resulting 2D velocity field is shown in Figure 6.6.2 and supports what we see in the continuum-subtracted images, with red-shifted material displaced to the East of the star and blue-shifted material displaced to the West. By finding and measuring the angle between the respective peaks of the blue- and red-shifted emission lobes we can estimate the "axis of motion" (identical to the disk axis in the case of a Keplerian-rotating disk) of 114°, a very good match to the photocentre displacement vectors of both AMBER ($112 \pm 10°$) and CRIRES ($114 \pm 3°$).

6.7 Kinematic modelling

In order to obtain quantitative constraints on the gas velocity field around MWC297 we fit a kinematic model to our AMBER observables exploring different scenarios for the origin of Brγ emission, namely a simple Keplerian-rotating disk and a rotating disk with an outflowing velocity component corresponding to a simplified disk-wind scenario. To model the kinematics traced by the AMBER HR-K differential quantities we employ the code that is discussed in Section 4.5.1. We model multiple physical scenarios that are described in the following two subsections, including a Keplerian rotation field in a geometrically thin disk and a velocity field similar to a magneto-centrifugally driven disk wind (Blandford and Payne, 1982).
For both scenarios, we compute synthetic images that include contributions from a continuum-emitting component and the line-emitting component. The continuum is modelled with an inclined Gaussian brightness distribution, using the FWHM size D, inclination i and system axis position angle θ determined in Sect. 6.3. The line-emitting region is modelled to extend from an inner radius R_{in} to an outer radius R_{out}, while the radial brightness distribution follows the power-law $\propto r^{\beta}$, where r is the radius and β is a free parameter (see Figure 6.7.1 for a schematic of the model setup). To avoid unphysical sharp edges in our model images (which might introduce artifacts), we implement the outer truncation using

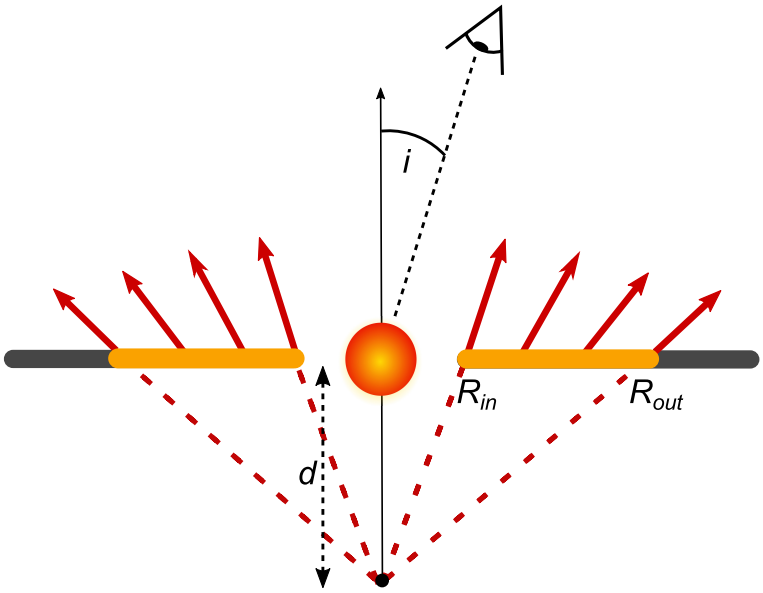

Figure 6.7.1: In our kinematic model the Brγ emission is emitted from a region of the disk's surface between R_{in} and R_{out} (shown in yellow) and is viewed at an inclination angle i. The kinematics of the line-emitting region include a toroidal component (analogous to v_k) and poloidal component, shown as red vectors from an imaginary source displaced at a distance d from the centre of the system.

a Fermi-type smoothing function (see Kraus et al., 2008b). To model the arc structures we see in the photocentre displacements, we introduce an opacity gradient (multiplied by an arbitrary factor α_o) which darkens the more distant parts of the disk. We adopt the stellar parameters (mass $M_\star$ and distance d) quoted in Sect. 6.1. From the resulting 3D image cube we compute wavelength-differential visibilities and phases at the uv-coordinates covered by our data.

6.7.1 Keplerian disk model

We first consider a simple Keplerian disk model, where the Brγ-emitting region extends from an inner radius R_{in} to an outer radius R_{out}. In the Keplerian rotation model, the velocity field $v_k(r)$ is defined as in Equation 4.4.2. We systematically sample the parameter space and compute the reduced χ^2 between the measured and model visibilities and phases: $\chi^2_r = \chi^2_{r,V} + \chi^2_{r,\phi}$. The parameter uncertainties are calculated by fitting the χ^2 surface near the minimum. The model parameter values and uncertainties corresponding to the best-fit model are listed in Table 6.7.1 and the corresponding model visibilities/phases/spectra are shown in Figs. 6.7.4 and 6.7.5 (solid blue lines). The model is able to reproduce the visibility drop across the line well for the majority of intermediate to

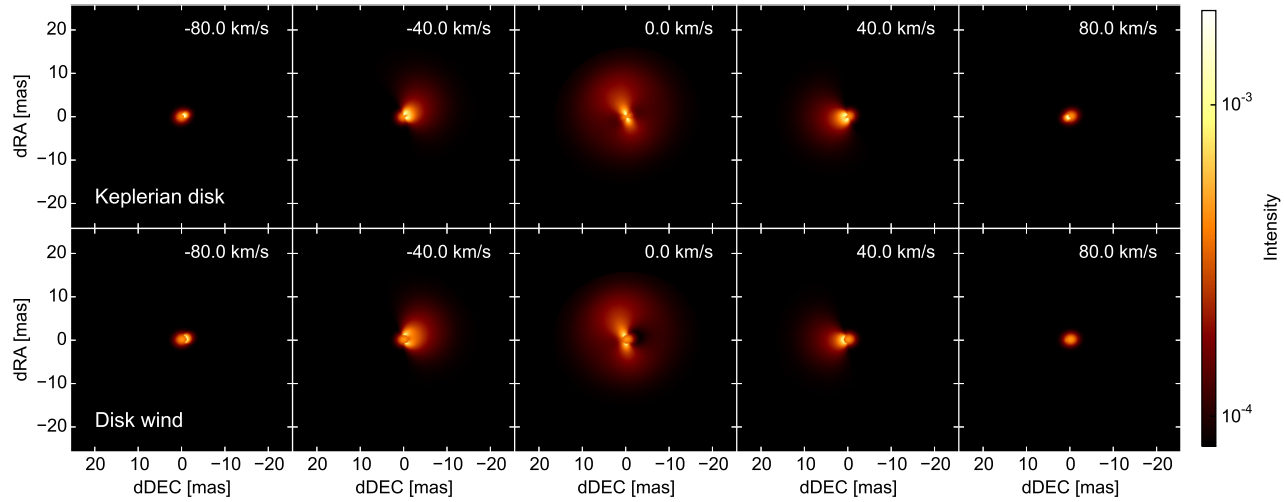

Figure 6.7.2: Upper panel: Synthetic model images calculated for our Keplerian model for five spectral channels. Lower panel: Synthetic model images calculated for our disk wind model for five spectral channels. We use an arbitrary logarithmic color scale to show the brightness distribution.

long baselines, but for the shortest (< 42m) baselines the model visibilities are lower than the observed quantities across the line. The sign and shape of the differential phase measurements are reproduced for the majority of baselines, with some significant residuals visible for the red-shifted part of the baselines with PAs between -100° and -96°. The single-peaked spectral line is modelled well with this scenario.

After fitting the AMBER data we also determine how the photocentre displacements from our best-fit model images compare to our observed CRIRES spectro-astrometry data. Figure 6.7.3 shows that the Keplerian model is a good fit to the CRIRES data, able to recreate the features of the DPs and the single peaked shape of the emission line.

Despite this model providing a generally good fit to the AMBER HR-K interferometry data, we find that the disk PA in the best-fit model does not match the disk orientation of the continuum-emitting disk, as modelled in Sect. 6.3. We find a θ value of 202.3° for our Keplerian model which is a perfect match to the axis of motion measured in Sect. 6.4 but shows a $\sim 3\sigma$ deviation from our AMBER LR measurement of the continuum PA. This calls the validity of the model into question, as it is an intrinsic property of a Keplerian disk model that the PA of the line displacement must be aligned with the major axis of the dust continuum disk.

Table 6.7.1: Ranges and best-fit values for our kinematic model parameters. The reduced χ^2 values for each of our best-fit kinematic models are also shown.

Parameter	Range	Keplerian	Disk wind
R_{in}	0 - 20 mas	1.7±0.5 mas	1.9±0.5 mas
R_{out}	0 - 100 mas	45±4 mas	45±4 mas
θ	0° - 180°	202.3±1.9°	192.1±2.1°
i	0° - 90°	21.8±3.5°	23.1±3.4°
β	−2.0 - 0.0	−0.99±0.08	−0.99±0.08
v_z	0.0 - 2.0 × v_k	-	0.14±0.02 × v_k
d	0 - 45 mas	-	1.1±0.4 mas
$\chi^2_{r,V}$	-	0.45	0.39
$\chi^2_{r,\phi}$	-	1.19	1.11
χ^2_r	-	1.64	1.50

6.7.2 Disk wind model

Given the remaining residuals in the Keplerian disk model (see Figure 6.7.4) as well as the significant deviations between the continuum disk orientation and the Brγ line photocentres (Sect. 6.4), we investigate in this section a more complex gas velocity field, such as a velocity field similar to a disk wind. For this purpose, we add to our Keplerian disk model a velocity component that points out of the disk plane, as predicted by theoretical accretion-driven MHD disk wind models (e.g., Blandford and Payne, 1982; Goodson et al., 1999; Ferreira et al., 2006). We assume that the line emission originates from the hot gas located near the disk, oriented relative to the observer with the disk inclination i and major axis PA θ, with both quantities treated as free parameters. In this model, the gas velocity is modelled as a superposition of the toroidal velocity component v_ϕ (identical to the Keplerian velocity v_k used in our previous model and a poloidal component representing the motion of material that is accelerated and lifted off the disk surface. To parameterise this poloidal velocity component we adopt a geometry similar to the one discussed in Kurosawa et al. (2006), with wind streamlines drawn from an imaginary point on the opposite site of the disk plane and located at a distance d (Figure 6.7.1). The velocity along this poloidal vector is treated as a free parameter and scales as a function of the Keplerian velocity v_k.

The synthetic images from our simple disk wind model are shown in Fig. 6.7.2 (lower panel) and its comparison to our observed data can be seen in Figs. 6.7.3 (CRIRES) and 6.7.4 (AMBER). Details of the best-fit values for all free parameters for both the disk wind and Keplerian models are listed in Table 6.7.1. The angular size of both the line and continuum-emitting regions for the disk wind model are nearly identical to those of the Keplerian model, causing the visibilities (which predominantly trace the object's 2D geometry) for each model to be very similar. The differences in the kinematic paradigm cause changes in the differential phase, however, due to the small out-of-plane velocity, these changes from the Keplerian model are subtle. We see no major deviations in the shape of the line profile, only a small shift of the line caused by the out-of-plane component (see Figure 6.7.5). The new model including the out-of-plane velocity component results in a much better fit to the PA of the continuum disk than the fit of the Keplerian disk model.

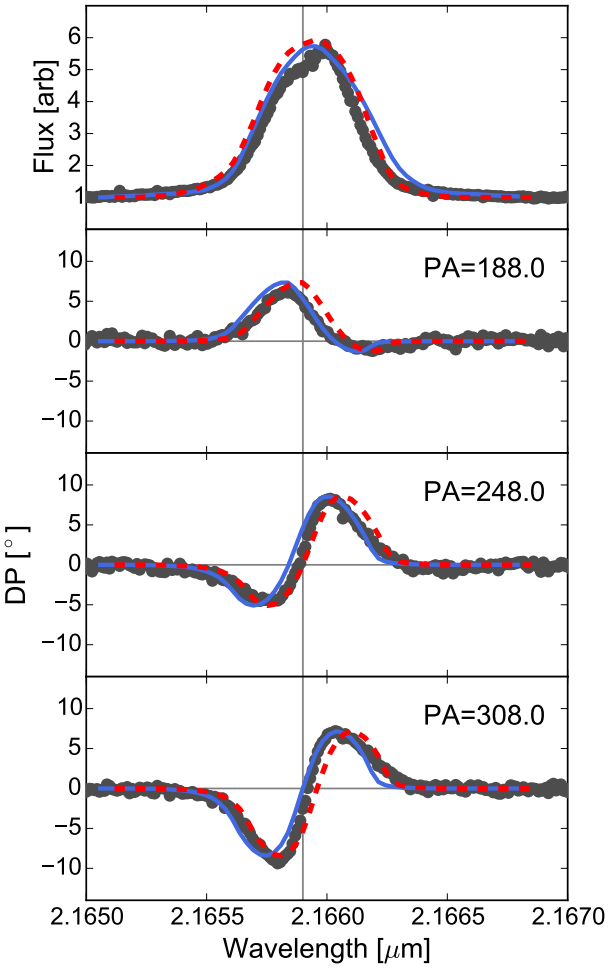

Figure 6.7.3: Synthetic spectra (top panel) and differential phases (lower panels) from our Keplerian (blue solid line) and disk wind (red dashed line) models plotted over our observed CRIRES data (dark grey points).

Throughout our kinematic modelling process we noted that adding an out-of-plane velocity component, such as is present in a disk wind, changes the perceived rotation angle traced by the Brγ photocentre vectors. To explore this phenomenon further we computed a grid of similar disk wind models, changing only the out-of-plane velocity for each different model, and calculated their photocentre displacement profiles from the raw model

fit images. Using a simple linear fit, we determine the position angle along which the photocentre vectors are predominantly displaced (see Fig. 6.8.1, left and middle panels) and find that the position angle offset increases linearly with increasing out-of-plane velocity (Fig. 6.8.1, right panel). We also find that as the wind velocity increases, the red-shifted photocentres become less displaced from the centre, with the blue-shifted vectors becoming more displaced. We therefore propose that measuring the displacement of the perceived axis of motion from the known disk major axis is a powerful diagnostic for the presence of out-of-plane velocity components. Further study into the physical interpretation of the PA shift, how it depends on the different parameters of the disk wind model, and an investigation of the phenomenon using other kinematic disk-wind models will be the subject of a future study.

6.8 Discussion

By measuring the photocentre displacement vectors from both spectro-interferometry and spectro-astrometry, we gain a model-independent view of the kinematics traced by the Brγ line. A remarkable trait of the photocentre patterns that is present in the AMBER and CRIRES data independently, are the loop-like arc structures. An example of a similar arc structure observed with IR spectro-astrometry can be found in the presentation of V921 Sco CRIRES data by Kraus et al. (2012b), although the displacement of the central channels away from the continuum was not as extreme as the case of MWC297 that we present in this paper. The ratio of the major/minor axes of the loop is dependent on the opacity parameter α_o and the inclination of the disk (minor axis becomes larger for more face-on objects). We account for this pattern in our model using an opacity field that obscures the furthest reaches of the disk. However, the origin of this opacity is not described in the model and there are a number of different scenarios that could be causing this effect in the observations.

In their recent work using SMA to study a massive young stellar object, Ilee et al. (2016) observed similar loop-like arc-like structures in the centroid shifts, traced by multiple spectral lines, which were the result of displacement of the central channel centroids away from the disk plane. Their system is seen closer to edge-on ($i\sim55^\circ$) and they interpret the arc-shaped displacement as being caused by the flaring outer regions of the disk. It is unlikely that this scenario applies to MWC297 as the disk is viewed almost pole-on ($i\sim20^\circ$) and any disk flaring will have only a small effect on the opacity so close to the centre of the disk. Therefore, other interpretations such as optically thick dust above the disk plane

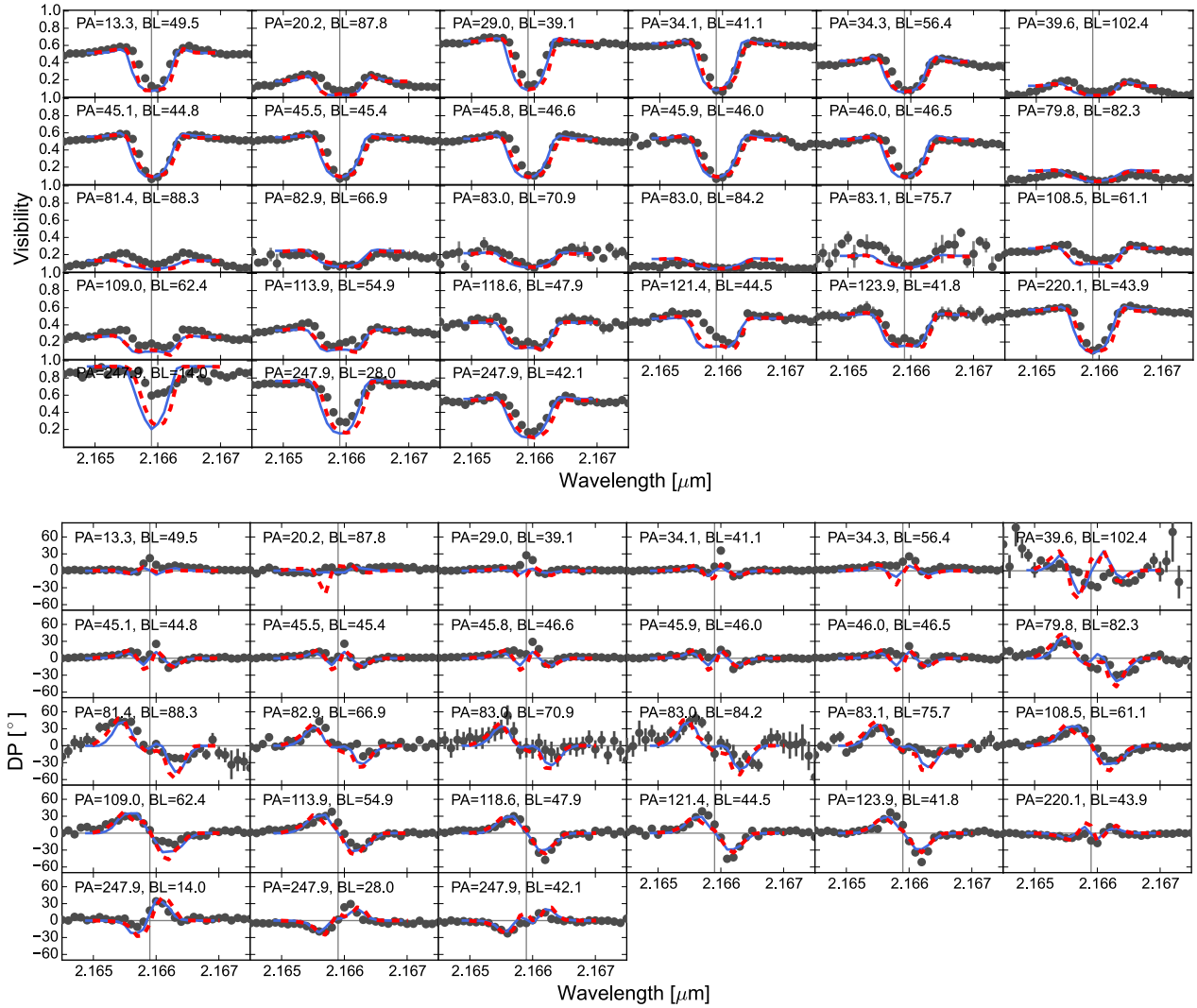

Figure 6.7.4: Visibilities (upper panel) and differential phases (lower panel) calculated from our kinematic models and compared to our observed AMBER data. The solid blue line represents the simple Keplerian disk model and the dashed red line represents our simple disk wind model. Data points are grey. The frame with PA=39.6, BL=102.4 is offset by 180° in order to see the differential phase changes at the Brγ line centre.

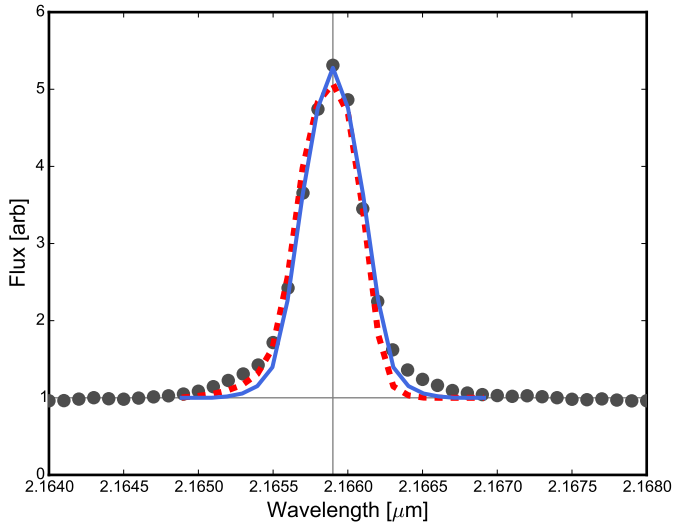

Figure 6.7.5: Spectrum calculated from our kinematic model compared with the Brγ spectrum from our AMBER data set. The solid blue line represents the Keplerian model and the dashed red line represents the simple disk wind model. Data points from AMBER are gray.

might be more applicable in the case of MWC297. Bans and Königl (2012) theorised that dust can exist above the disk plane. Theoretical explanations for this include the ejection of dust in a disk wind (Bans and Königl, 2012) and a dusty magnetically supported atmosphere (Turner et al., 2014).

At the longest baseline of our AMBER data set we see a 180° flip in the differential phase across the Brγ line (PA=39.6°, BL=102.4m). In Figs. 6.5.1 and 6.7.4 the range of the frame is shifted in order to show the differential pattern of the phase and the comparison to the models. This phase jump at long baselines is indicative of the visibility moving from the first to the second lobe, caused primarily by sharp edges in the observed brightness profile. The fact that we only see this phase jump in the Brγ line and at the longest baselines indicates a detection of a sharp inner or outer edge of the line-emitting region.

Using the *IRBis* method we reconstruct a series of velocity-resolved images across the Brγ line from our AMBER HR-K data set, the first such images of a young star achieved with optical interferometry (Sect. 6.6). We retrieved images for six spectral channels within the line and computed continuum-subtracted images (Figure 6.6.1) as well as a first-moment map (Figure 6.6.2) that reveals the 2D velocity field, with the blue- and red-shifted lobes displaced along a position angle of 114°. This is in agreement with the photocentre displacement vectors derived from both our AMBER and CRIRES data sets (Sect. 6.4).

The wavelength-dependent brightness distribution in the images closely resembles the synthetic images of both our Keplerian and disk wind models, both in the morphology

of the line-emitting gas and the perceived "axis of motion". At intermediate velocities (2.16584μm and 2.16611μm), we see a double-lobed structure, both in the reconstructed images and the model images ($\pm$40km/s), although it is not possible to distinguish between the Keplerian and disk wind scenario using the images alone.

To provide a comparison between our kinematic model and the image reconstructions we constructed first moment maps from our model frames using the same code as was used for the images in Sect. 6.6, with the results shown in the middle and right-hand frames of Figure 6.6.2. Both the Keplerian and the disk wind models show the displacement of blue- and red-shifted material along a similar PA to what was seen in the photocentre shifts of both AMBER (Figure 6.5.1) and CRIRES (Figure 6.4.1), as well as along a similar PA as seen in the moment map from the images (Figure 6.6.2, left panel). The most noticeable difference in the moment maps of the two model scenarios is that the blue-shifted lobe of the disk wind model traces a larger area than the corresponding lobe in the Keplerian model. Whilst there are some slight differences between the different models' moment maps, both moment maps are a good match to the results of the image reconstruction (Figure 6.6.2, left panel) and we find that comparing the moment maps is not a useful way to distinguish between models. The calculation of the moment map from our model frames using the same code as was used for the reconstructed images creates a small square shaped artifact at the centre of the moment map caused by the rotation of the inner edge of the line-emitting region.

Disks demonstrating Keplerian-like motion have also been observed around various other young stellar objects (e.g. V921 Sco, Kraus et al. 2012b; HD 100546, Mendigutía et al. 2015; HD 58647, Kurosawa et al. 2016). A significant difference between these cases and our observations of MWC297 can been seen in the relative geometries of the continuum and line-emitting regions. For the objects mentioned above, particularly V921 Sco and HD 100546, the Brγ line emission is more compact than the K-band continuum-emitting ring, usually tracing gas inside or near the dust inner rim (in contrast to MWC297). Our analysis and modelling of the wavelength-dependent visibilities shows that the line-emitting gas is located in a very extended region relative to the continuum, though this could be due to the extremely compact K-band continuum size. The compact nature of the continuum has already been discussed by many other authors (Eisner et al., 2004; Monnier et al., 2005; Malbet et al., 2007; Kraus et al., 2008a; Acke et al., 2008; Weigelt et al., 2011) but the physical interpretation for this compact continuum size is still a subject of discussion. This problem of undersized Herbig Be stars is not exclusive to MWC297, and was also found in several other high-luminosity objects in the size-luminosity study of

Monnier and Millan-Gabet (2002). Several general explanations as to why these objects are so compact have been put forward, including:

- emission from a compact viscously heated accretion disk (e.g. Kraus et al., 2008a)
- an inner gaseous component that shields stellar radiation to let dust survive closer to the central star (e.g. Eisner et al., 2004; Monnier and Millan-Gabet, 2002)
- additional emitting components such as highly refractory grains (e.g. Benisty et al., 2010).

Despite the extremely compact K-band continuum emission, the relative extension of the Brγ emission raises the question of how the line-emitting gas can be heated to the temperatures required to emit the Brγ line (i.e., $8000 - 10,000$K, Kurosawa et al., 2006). The compact nature of the K-band continuum requires optically thick material at small circumstellar radii, and therefore it is unlikely that the more extended line-emitting gas could be heated by radiation from the central star. In their previous work on this object, Weigelt et al. (2011) discussed the relationship between the continuum and the line-emitting materials and favoured the explanation that the compact continuum emission is caused by a mixture or warm dust and refractory grains which possibly play an important role in the formation of a disk wind. Material ejected in a disk wind can be rapidly heated by ambipolar diffusion up to temperatures sufficient to emit in the Brγ line, and these temperatures can also be exceeded in the disk midplanes of rapidly accreting objects.

We find that our best-fit Keplerian kinematic model shows a 3σ deviation from the continuum disk PA, a difference that we account for by employing a disk wind model which results in a similar PA to the continuum. Using the results from our photocentre analysis allows us to place tight constraints on the position angle of the rotation that we observe in the Brγ line. We can see from our observations in Figs. 6.4.1 and 6.5.1 that our observed CRIRES and AMBER photocentres are consistent with one another, with axes of motion of $112 \pm 10^\circ$ (AMBER, Sect. 6.5) and $114 \pm 3^\circ$ (CRIRES, Sect. 6.4.1), which results in our best estimate for the Brγ line position angle of $114 \pm 3^\circ$. This angle differs significantly from the major axis of the dust disk intensity distribution, as determined from near-infrared interferometry in the H- and K-band continuum. Measurements of the continuum geometry from PIONIER (Lazareff et al., 2017) and AMBER estimate the position angle of the disk major axis to $103.7 \pm 1.7^\circ$ and $99.6 \pm 4.8^\circ$, which are consistent with each other, but both differ from our measurements of the axis of motion by $\sim 10^\circ$ (detailed in Sect. 6.4, Figs. 6.4.1 and 6.5.1). Whilst modelling the kinematics of the

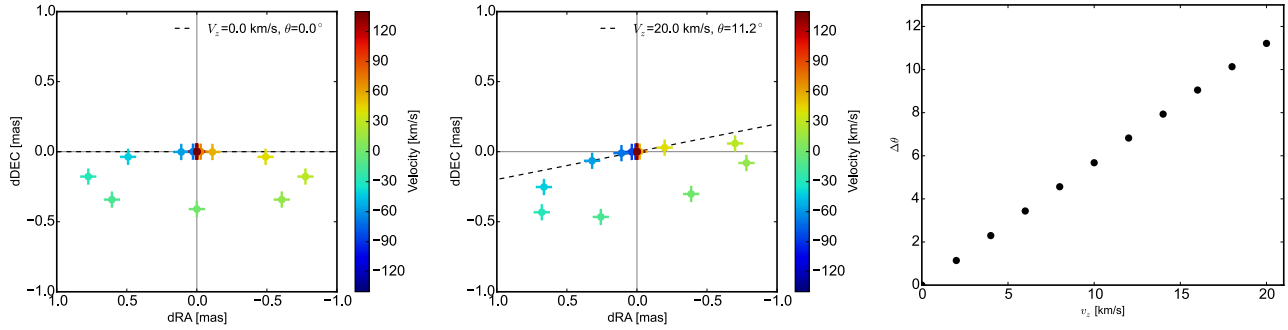

Figure 6.8.1: Left: Model photocentre displacements for our Keplerian disk model with the disk major axis along a PA of 90°. We impose an opacity field in order to shift the central channels away from the continuum so that they do not overlap. Middle: Model photocentre displacements for a similar model with an out-of-plane velocity of 20 km/s. We see that the perceived PA of the system axis is offset by a value of 11.2° and that the red-shifted vectors are less displaced from the continuum than their blue-shifted counterparts. Right: A plot of the out-of-plane velocity (v_z) plotted against system axis change ($\Delta\theta$) for our grid of models showing that the PA offset varies linearly with v_z.

disk wind (Sect. 6.7.2) we noted that the apparent PA of the axis of motion became displaced from the continuum disk axis as the out-of-plane velocity increased (shown in Fig. 6.8.1). We find that the observed PA offset of $\sim$10° can be explained by an out-of-plane velocity between 15 and 20 km/s. When exploring the disk wind model parameter space we found that the best-fit model is consistent with the continuum geometry as measured by PIONIER and AMBER as well as providing a good fit to the visiblity and differential phase measurements from our AMBER HR-K data. As a possible alternative explanation for the perceived PA difference we considered a warped-disk scenario, where the orientation of the disk changes as a function of radius. In this case, the continuum emission would trace a closer-in region of the disk than the Brγ line emission and the observed PA difference would trace the radial differences in disk orientation instead of kinematical effects. However, as the line-emitting region is only approximately two times larger than the continuum disk, the warping would have to be very extreme to produce a PA difference as large as the 10° that we see. Additionally, we see no evidence of a PA difference between the H-band PIONIER observations, which find a PA of $103.7 \pm 1.7°$ (Lazareff et al., 2017), and our AMBER K-band measurements with a PA of $99.6 \pm 4.8°$. The consistency of these two observations, which trace regions of the disk with different radial extension, suggests that the MWC297 disk is not significantly warped but more measurements of the disk PA at larger radial extension could further clarify this.

We test the fit of our disk wind model to the interferometric observations of MWC297 and examine how adding an out-of-plane velocity component affects the synthetic channel

maps and Brγ line profiles. It is easy to spot the main differences between our Keplerian model and disk wind model when we compare their synthetic model images (Fig. 6.7.2). Keplerian rotation produces symmetric brightness profiles in the channel maps, while the disk wind model also permits asymmetric profiles. In our disk wind model we can see a clear shift away from the symmetric velocity field of the Keplerian paradigm, with more flux visible in the blue- than in the red-shifted channels and an asymmetric brightness distribution in the central-wavelength channel image. We calculate the blue-shift caused by the out-of-plane velocity in the model and apply a corresponding wavelength correction to correct for the small wavelength changes we see in the disk-wind model. We find that the differences in the synthetic data between our Keplerian model and the disk wind model are subtle, and manifest themselves mainly as differences in the differential phase. For each scenario we compare the observed data with the synthetic data from each of our models and calculate the reduced χ^2, finding a marginal difference between the two models with the Keplerian model having a larger χ^2 (1.64) than the disk-wind model (1.50). In particular, the disk-wind model is able to reproduce small phase jumps in the centre of the Brγ line that are seen for baselines with position angles between 80° and 84° and remains a good fit to the simple S-shaped phases at other baselines. Some of the remaining residuals could be caused by higher-order velocity structures beyond the scope of our kinematic model but that could be reproduced by more complex kinematic codes.

A significant advantage that our disk-wind model has over the simple Keplerian model is that it allows us to reconcile the position angle of the major axis of the continuum disk and the position angle of the "axis of motion" measured in the AMBER and CRIRES photocentre shifts. Due to the position angle shift we see in our disk-wind model (see Fig. 6.8.1 and discussion above), the θ value for our disk-wind model is within the standard deviation of the PA observed by PIONIER (Lazareff et al., 2017) and AMBER LR (in contrast to the Keplerian model). Furthermore, the much better fit of the disk-wind model to the geometry of the continuum-emitting disk makes it more plausible than the Keplerian alternative.

A disk-wind model has already been invoked by Weigelt et al. (2011) to model AMBER HR-K visibilities and phases measured on MWC297 as well as the spectral line profile. However, their AMBER data probed only a single position angle and a limited baseline length range (14-42 m), but was still used to constrain simultaneously the disk orientation as well as a complex 2D velocity field. Weigelt et al. (2011) found that their two disk-wind models with PAs of the projected polar axis of both 65 and 300° are approximately able to reproduce their observations (Sect. 4.4 and Figure 7 in their paper). Using their model

images we computed visibilities and differential phases for our new AMBER HR-K observations with better *uv*-coverage and show them in Figure 6.10.1 (further discussion in Section 6.10).

6.9 Conclusions

In this paper we investigated the kinematics of the Brγ-emitting gas at milliarcsecond scales with spectrally dispersed interferometry and spectro-astrometry. Our VLTI/AMBER (R=12 000) observations represent the most extensive data set that has so far been employed for studying the gas kinematics in the inner few AU around a young stellar object, while our VLT/CRIRES (R=100 000) data set allows us to measure the detailed line profile and the photocentre displacements in the line with very high SNR.

Analysing the combined data set allows us to draw the following conclusions:

1. Our AMBER observations at low spectral dispersion ($R = 35$) show that the NIR continuum is small (FWHM = 4.93mas), occupying a region $\sim$3.6 times more compact than the expected $\sim$3au dust sublimation radius for MWC297 (at $\sim$17.6mas). From the AMBER visibility measurements we determine that the disk has a major axis PA of $99.6^\circ \pm 4.8^\circ$ and an inclination of $32^\circ \pm 3^\circ$, consistent with the recent PIONIER observations by Lazareff et al. (2017). We model the wavelength-dependent visibilities from our AMBER HR observations across the Brγ line and find that the line-emitting region is $\sim$2.3 times more extended than the compact K-band continuum.

2. The 2D photocentre displacement vectors derived from the AMBER and CRIRES data indicate a velocity field that is dominated by rotation. We are able to place strong constraints on the position angle of the axis of motion and find consistent values for AMBER ($112^\circ \pm 10^\circ$) and CRIRES ($114^\circ \pm 3^\circ$). At low velocities, both data sets show a photocentre displacement to the north of the disk axis, indicative of the furthest parts of the disk being obscured by a strong milliarcsecond scale opacity gradient.

3. Our channel maps resolve the Brγ line at a spectral resolution of 12 000 and an angular resolution of 2 mas and represent the first velocity-resolved image obtained for a young star at infrared wavelengths. The individual channel maps, as well as the moment map, indicate a rotation-dominated velocity field and show brighter

emission from the northern side of the disk, consistent with the previously discussed opacity gradient.

4. In order to quantify the velocity field, we fit a Keplerian-disk model and find that this model provides a moderate fit to the observed visibilities, differential phases and spectro-astrometric signal. However, the derived gas-disk PA in this model is inconsistent with the orientation of the continuum disk on a 3σ-level, indicating the presence of a non-rotational velocity component.

5. In order to explain the significant PA difference between line photocentres and the continuum disk ($\Delta\theta = 14 \pm 3^\circ$), we extend the Keplerian disk model by including a poloidal velocity component, simulating a parameterised disk-wind model. We find that the discrepancies between the measured line and continuum PAs can be reconciled by a disk-wind model with an out-of-plane velocity of $0.14 \times v_k$. Our parametric disk-wind model is able to fit the Brγ line profile, as well as the high-resolution spectro-interferometry and spectro-astrometry data.

6. Through our disk-wind modelling, we discover that the PA difference between the disk major axis and the axis of motion $\Delta\theta$ constitutes a powerful diagnostic for detecting non-Keplerian velocity contributions, which could be exploited in future observational studies.

6.10 Outlook

6.10.1 Comparison with model from Weigelt et al. (2011)

We were able to obtain the MWC297 model frames published in the work of Weigelt et al. (2011) and used them to construct a comparison figure to the full AMBER HR-K data set that we analyse above (shown in Figure 6.10.1). Adopting their best-fit PA value of the polar axis of the disk (300°), we find that the model provides reasonable agreement to the observed visibilities with a reduced $\chi^2_{r,V} = 1.01$; although the shape of the visibility drop is systematically more narrow in wavelength than what is observed in our new data. However, the differential phases predicted by the model (with values up to $\pm 180^\circ$) are much stronger than observed (phases $\gtrsim \pm 60^\circ$), which leads to a poor $\chi^2_{r,\phi}$ of 10.1. Additionally, with a best-fit minor-axis PA of 300°, the Weigelt et al. (2011) model seems incompatible with measurements of the disk continuum geometry, both from PIONIER ($13.7 \pm 1.7^\circ$,

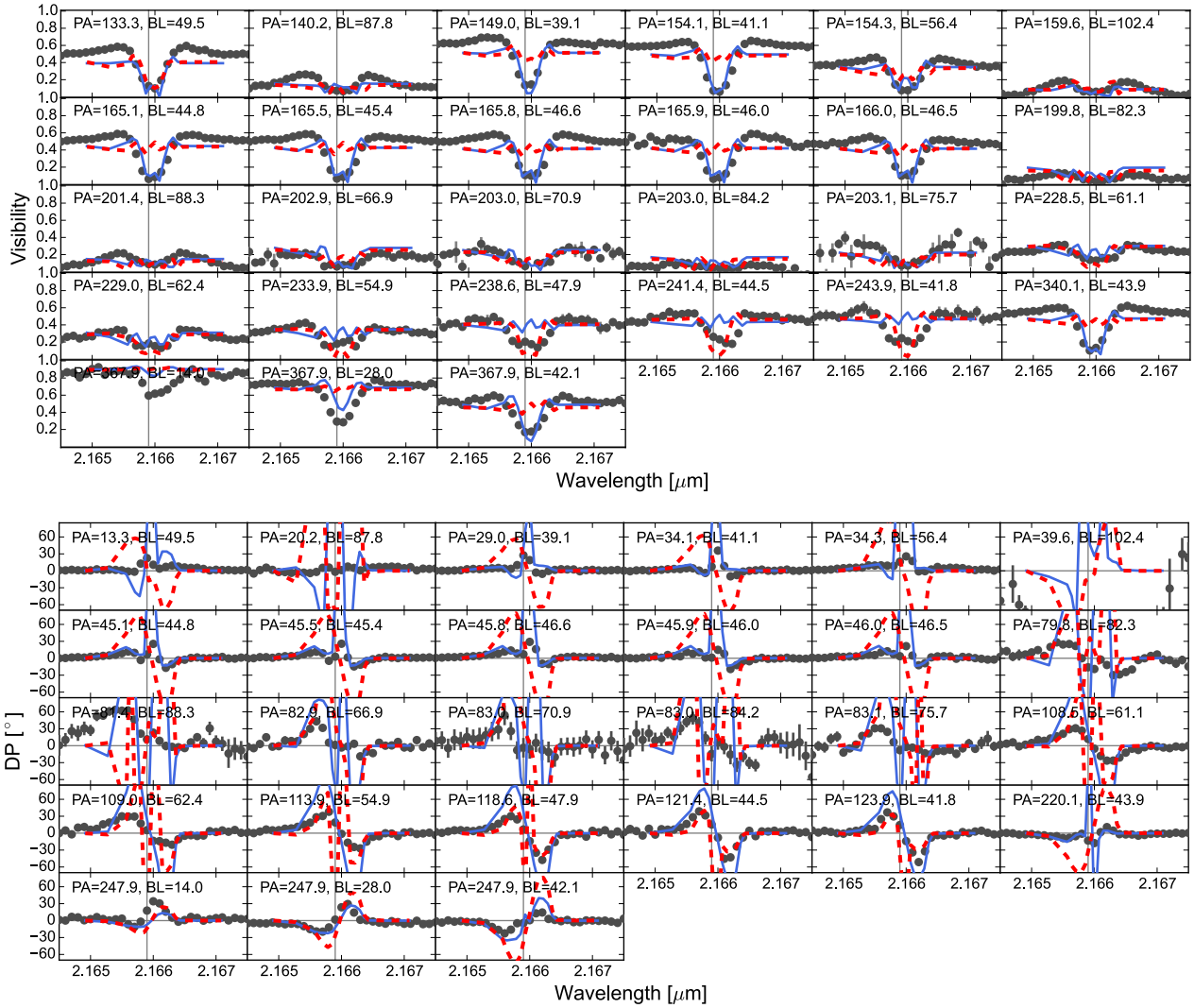

Figure 6.10.1: Visibilities (upper panel) and differential phases (lower panel) calculated from the MWC297 kinematic model from Weigelt et al. (2011) and compared to our observed AMBER data. The solid blue line represents the best-fit model ($\theta = 300°$) and the dashed red line represents the model with the best match to the continuum geometry ($\theta = 10°$). Data points are gray.

Lazareff et al., 2017) and our AMBER LR measurements ($9.6 \pm 4.8^{\circ}$). When we orient the model to match the measured continuum geometry of MWC297 (by adopting a PA value of 10°) we find that the χ^2_r value increases to 12.8 ($\chi^2_{r,V} = 1.33$, $\chi^2_{r,\phi} = 11.5$). Possibly, this significant difference between the measured disk geometry and the model orientation is linked to the effect that we explored previously in this section (and that are shown in Figure 6.8.1) where the out-of-plane velocity component distorts the perceived rotation angle. Therefore, this might indicate that the toroidal velocity component in the Weigelt et al. (2011) model is overestimated, causing the perceived axis of motion to differ from the model's continuum axis more than observed.

6.10.2 Testing the photocentre validity

I conducted additional studies into the validity of the theory of photocentre shifts and how they are affected by different *uv*-coverages. The equation for deriving photocentre shifts from differential phase measurements (Lachaume, 2003; Le Bouquin et al., 2009) is only valid for cases where the object is marginally resolved. In our study of MWC297, we used this equation to calculate photocentre shifts (see Section 6.4), despite the object being well resolved in the continuum and even more so across the Brγ line. The results of this photocentre study are similar to the results from CRIRES spectro-astrometry, indicating that the AMBER photocentres accurately trace the kinematics of the Brγ emission. Initially, I constructed a model of a simple Keplerian disk at a moderate inclination of 30°, a major axis PA of 90° and an outer radius of 10mas. I created a sample of synthesized interferometric data sets by generating a set of 100 interferometric arrays, each with a random *uv*-coverage, and synthesizing the differential phase for each array. I generated two distinct randomised data sets, one with three baselines and the other with twelve baselines. In order to compare the results, the elongation and PA of the synthesized interferometric beam were calculated by taking the Fourier transform of the *uv*-coverage.
Using this synthetic data, the photocentre shifts were calculated using the same approach that is outlined in Section 6.4. The best-fit rotational PA was calculated by combining the corresponding red and blue-shifted vectors, with any variations from the model disk major axis PA of 90° taken into account. I then compared the offset of the best-fit PA of the photocentre shifts to the eccentricity and PA of the beam, along with the maximum baseline of the *uv*-coverage. These comparisons can be seen in Figure 6.10.2. Using the method for calculating the rotational PA I found that for 87% of the synthesized three-baseline data sets the perceived PA is within one standard deviation of the model PA. For

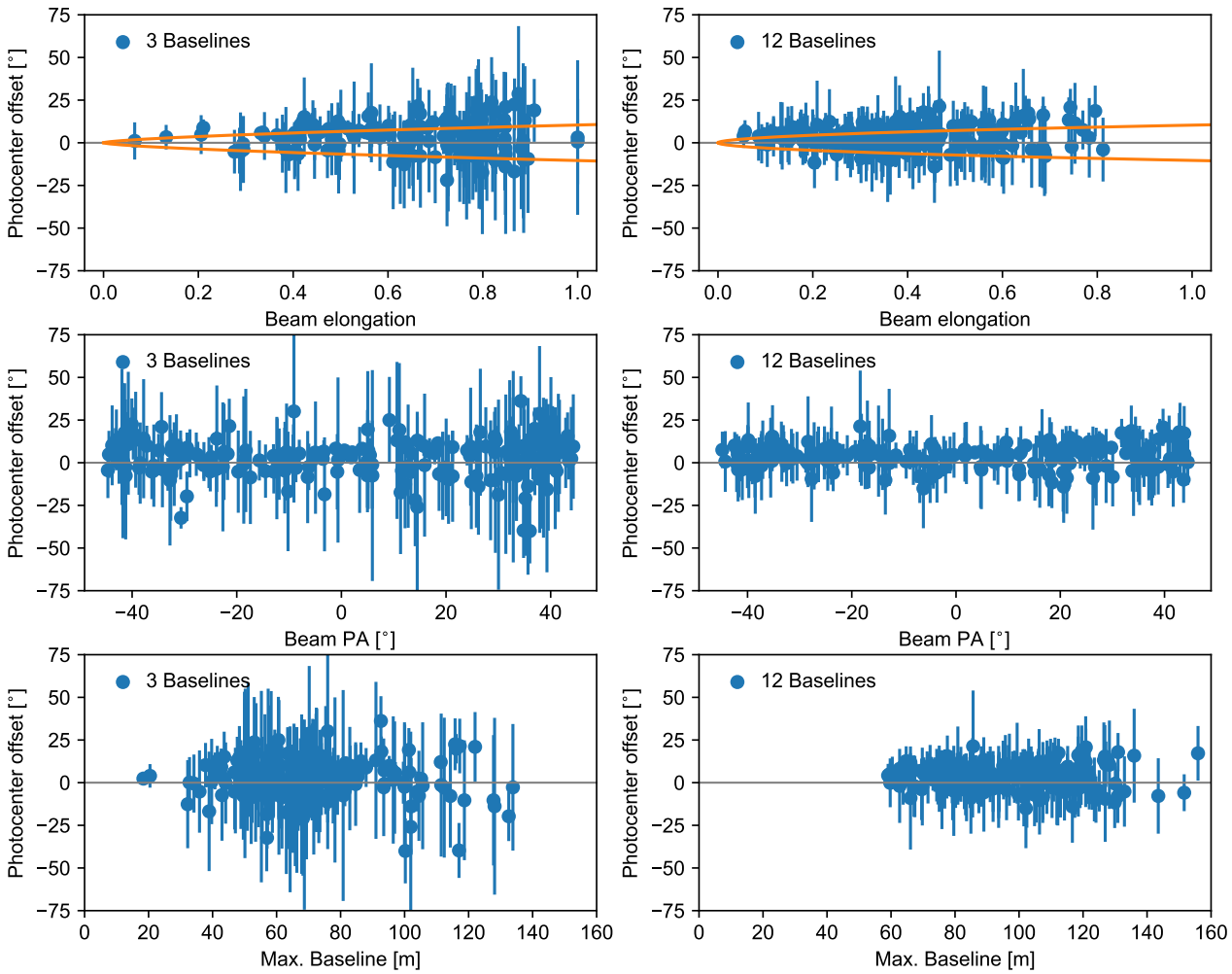

Figure 6.10.2: Top panel: Photocentre offset vs. beam elongation for three telescope and twelve telescope *uv*-coverages. The orange trend lines indicate how the mean photocentre offset (positive or negative) increases with the beam elongation. Middle panel: Photocentre offset vs. beam PA for three telescope and twelve telescope *uv*-coverages. Bottom panel: Photocentre offset vs. maximum baseline for three telescope and twelve telescope *uv*-coverages.

89.5% of the data sets with twelve baselines, the perceieved photocentre rotation axis is within one standard deviation of the model rotation axis.
The elongation of the beam is defined as the ratio of the beam's minor axis to it's major axis (where the beam is defined as an ellipse). The synthesized data with both three and twelve baselines showed an increase in the magnitude of the PA offset as the beam elongation increased. I did not detect any significant correlation between the beam PA and the PA offset.
Increasing the number of baselines from three to twelve yields a decrease in the mean angle offset of the photocentre displacements from 8.5° to 5.3°. Additionally, the mean uncertainty of the rotational PA decreases from 20.8° for three baselines to 13.2° for twelve. The accuracy of the photocentre displacements is most strongly affected when the beam elongation of the *uv*-coverage is increased. It is important to take this into account when attempting to obtain photocentre shifts in the future, and to minimize the elongation of the beam of the *uv*-coverage if possible. This is often more straightforward to manage with more baselines in the *uv*-coverage. I did not find a strong correlation between the maximum baseline of the *uv*-coverage and the accuracy of the photocentre rotation angle for this model case. This could suggest that how resolved an object is does not have a strong effect on the perceived rotation angle of the photocentre shifts, although smaller line-emitting regions could be modelled to confirm this.

6.10.3 Retrospective

The extent of the AMBER HR-K data set used in the work is unique for studies of young stellar objects, only compatible to the data set used by Weigelt et al. (2016) to study the Wolf-Rayet star η Car. The stark comparisons between this work and the previous work on MWC297 by Weigelt et al. (2011) show that obtaining the additionaly *uv*-points is essential to more fully understand the kinematics traced by the line-emitting material. Since the introduction of GRAVITY, which allows for four-telescope beam combination, compiling a similarly extensive *uv*-coverage is possible in half the number of observations. Despite this fact, the work above remains the most extensive high-spectral dispersion interferometric study of young star to date, but this should be expected to change withinin the next few years. Since publication this paper has been cited in works by Kreplin et al. (2018), Sanchez-Bermudez et al. (2018), Mortimer and Buscher (2018) and Berger (2018).
With AMBER now decommissioned, the maximum spectral resolution achievable with interferometry in the near-infrared has ben cut drastically from $R = 12,000$ to $R = 4,000$.

The work above demonstrates the importance of high-spectral dispersion when it comes to wavelength-dependent image reconstruction. The AMBER HR-K spectrum clearly shows that the Brγ line is spectrally resolved across $\approx$20 spectral channels, but we can only achieve good image reconstructions of the line emission for the central $\approx$6 channels. Reducing the spectral resolution by a factor of three (as has been done for GRAVITY) will present a problem for objects such as MWC297, which have relative narrow emission lines. It may be possible to image the Brγ emission as it differs from continuum but not possible to achieve the spectral resolution to distinguish between complex kinematic scenarios. Further studies focussed on spectrally-dispersed image reconstruction must be conducted with GRAVITY to demonstrate the instrument's capability in this field.

Chapter 7

Revealing the excitation and velocity structure of the MWC297 disk wind through multi-line spectro-interferometry

7.1 Introduction

Observations of young stellar objects (YSOs) are characterized by the presence of circumstellar accretion disks as well as astrophysical jets and outflows. These outflows, which range from the tightly collimated jets from T Tauri stars to the powerful winds from Herbig Ae/Be stars, influence future generations of star formation when they impact with molecular clouds in the interstellar medium (Heger et al., 2003; Lee et al., 2005). Despite their importance, there are many unanswered questions regarding the origins of these outflows and how they are launched from the compact inner regions of the disks which surround young stellar objects.

Spectro-interferometry of the Brγ line has emerged as a powerful tool for measuring the distribution and kinematics of outflowing gas from young stellar objects. This technique gives observers the ability to constrain the size of the line emission region as well as the kinematics of the line-emitting gas (in the case of observations with high spectral dispersion). The viability of this technique is demonstrated previously in this thesis in Chapter 6 and later in Chapter 8. Additionally, other studies by various authors employing spectro-interferometry of the Brγ line are discussed in Section 3.5.

While the existing Brγ data ($R = 12,000$) is well-suited to constrain the kinematics it

provides only limited constraints on the temperature, density, and excitation structure of the line-emitting gas. Bary et al. (2008) demonstrated how spectroscopic observations of various Hydrogen spectral lines can be compared to reveal information about the physical conditions of the line-emitting gas. Whilst the line emission strengths were found to vary for different objects and epochs, Bary et al. found that the ratios between the different emission lines remained the same, consistent with previous results by Muzerolle et al. (2001) and Natta et al. (2006). Bary et al. compared the measured line ratios to hydrogen recombination models for a range of temperatures and electron densities, finding that the Hydrogen gas is not in local thermodynamic equilibrium.

Conducting interferometric observations in multiple line transitions affords us the opportunity to constrain the physical conditions of the line-emitting gas, as each transition corresponds to a different excitation level and therefore traces a different temperature and density regime in the circumstellar environment. A precedent for this was set in an earlier study by Kraus et al. (2012c), who demonstrated with AMBER observations of a classical Be star that such multi-line transition observations help to place unique constraints on the physical conditions of the line-emitting gas. Kraus et al. constructed a simple radiative transfer model assuming local thermodynamic equilibrium, finding that the Brγ emission originates from a similar region to the Hα emission, more extended than the location of the Pfund lines. Multi-line spectro-interferometry has been previously achieved for a young stellar object by Koutoulaki et al. (2018), who observed the K-band and Pfund line emission from HD 50138. Koutoulaki et al. derived the angular size of the different line-emitting regions, concluding that each of the Pfund lines originated from the same region, similar in size to the Brγ emitting region and more compact than the continuum.

We employed AMBER's H-band medium resolution mode (MR-H) in order to spectrally and spatially resolve the line transitions of the hydrogen Brackett series in the wavelength range from 1.4 to 1.75 μm. This mode of AMBER has rarely been employed, likely due to its technical limitations requiring objects with correlated magnitudes brighter than 6.5 in the H-band, a very uncommon trait in YSOs. As such, no data using this observation mode has ever been published, making the study presented in this chapter unique. We fitted the wavelength-dependent visibilities using a simple two-component model to determine the characteristic sizes of the Brackett series lines relative to the continuum emitting disk. For each of the Brackett series lines observed we computed model-independent photocentre shifts and compared the results with the known orientation of the continuum emission. Finally we constructed a global kinematic model for MWC297, achieving a good fit to our AMBER MR-H data and compared this model to the similar model constructed as part

Table 7.2.1: Observation log for our MWC297 data taken with VLTI/AMBER's MR-H mode. For all observations the DIT is 0.3s.

Instrument	Date	Telescopes	UT	NDIT	Proj. baselines	PA	Calibrator
			[hh:mm]	#	[m]	[°]	
AMBER	2014-04-15	U1/U2/U4	09:52	3720	54.2/89.2/129.2	-151.0/-97.8/-117.4	HD 167768
MR-H	2017-07-07	U1/U3/U4	05:35	2520	127.1/53.7/102.4	-116.5/-245.4/-140.6	HD 167768
	2017-07-12	U1/U3/U4	03:35	5040	97.6/128.0/62.0	34.0/-118.0/-70.4	HD 164259

of the study in Chapter 6. We found that the Brackett series lines in the H-band originate from a region of the MWC297 disk wind close to the central star, with a poloidal velocity of $\sim$220kms^{-1}.

7.2 Observations and data reduction

We observed MWC297 once in 2014 and then again several times in 2017 at the Very Large Telescope Interferometer (VLTI) using the beam combining instrument AMBER (Petrov et al., 2007). The 2014 data was observed by Stefan Kraus in visitor mode as part the ESO program 093.C-0418 and the 2017 data was observed with service mode as part of the ESO program 097.C-0822, for which I was the principle investigator. Our VLTI/AMBER observations are outlined in Table 7.2.1 with the *uv*-coverage of these observations shown in Fig. 7.2.1. The different data sets use the UT1-UT2-UT4 and UT1-UT3-UT4 configurations which covers the maximum number of baselines and position angles that can be achieved with the VLTI Unit Telescopes (without taking earth-rotation synthesis into account). Due to the extremely resolved nature of MWC297 in the H-band we could not make use of the FINITO fringe

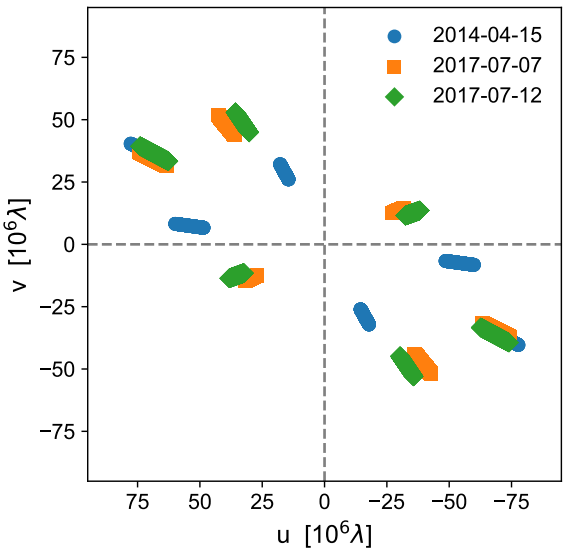

Figure 7.2.1: *uv*-coverage achieved with our VLTI/AMBER MR-H (R=1,500) interferometric observations of MWC297.

tracker, making it more difficult to obtain a high signal-to-noise ratio (SNR) for the differential interferometric quantities. However, this does allow us to directly measure the visibility without the visibility calibration bias that can be induced with FINITO.
For each science observation of MWC297 we also observed a calibrator star, with the stars HD167768 and HD164259 used as our calibrators (detailed in Table 7.2.1). The data was reduced with our own AMBER data-processing software package, making use of the pixel-to-visibility matrix algorithm P2VM (Tatulli et al., 2007; Chelli et al., 2009) to extract the visibility, differential phase, and closure phase for each spectral channel of the observed AMBER interferogram. Heliocentric line-of-sight velocities for each observation are obtained using the ESO Airmass tool and the data is subsequently corrected for the Heliocentric velocity. The photospheric absorption components were not subtracted from our model spectra.
Across the H-band we spectrally resolve multiple different H-band lines in the Brackett series, ranging from Br6 to Br12. For each of the resolved spectral lines we observe high-SNR wavelength-dependent visibility and differential phase signals. The wavelength-dependent visibility increases for each of the spectral lines, indicating that the line-emitting regions are more compact than the continuum. The shapes of the differential phase signals do not vary significantly for different spectral lines, with the amplitude of the signals varying between $\sim 20^{\circ}$ and $\sim 10^{\circ}$.

7.3 Visibility modelling

We initally model the wavelength-dependent visibilities of our AMBER MR-H data with a simple, single-component model of a Gaussian distribution, allowing the FWHM to vary with wavelength. The results of this first fit indicate that the characteristic size of the emission decreases by a similar amount across each of the Brackett series lines, suggesting that the line emission is more compact than the continuum emission. We improve our simple model by adding a second Gaussian component, fixing one component to match the size of the continuum emission whilst allowing the second component to vary in size with a normalised flux that matches the AMBER spectrum. The results of this fit indicate that the FWHM of the line emission steadily increases in size for lower-order lines, from $\approx$2mas for Br12 to $\approx$3.5mas for Br6. The results of this simple first-order fitting are shown in Figure 7.3.1.
Lazareff et al. (2017) determined the characteristic morphology of the H-band emission from MWC297 using PIONIER, modelling the visibilities with several geometric mod-

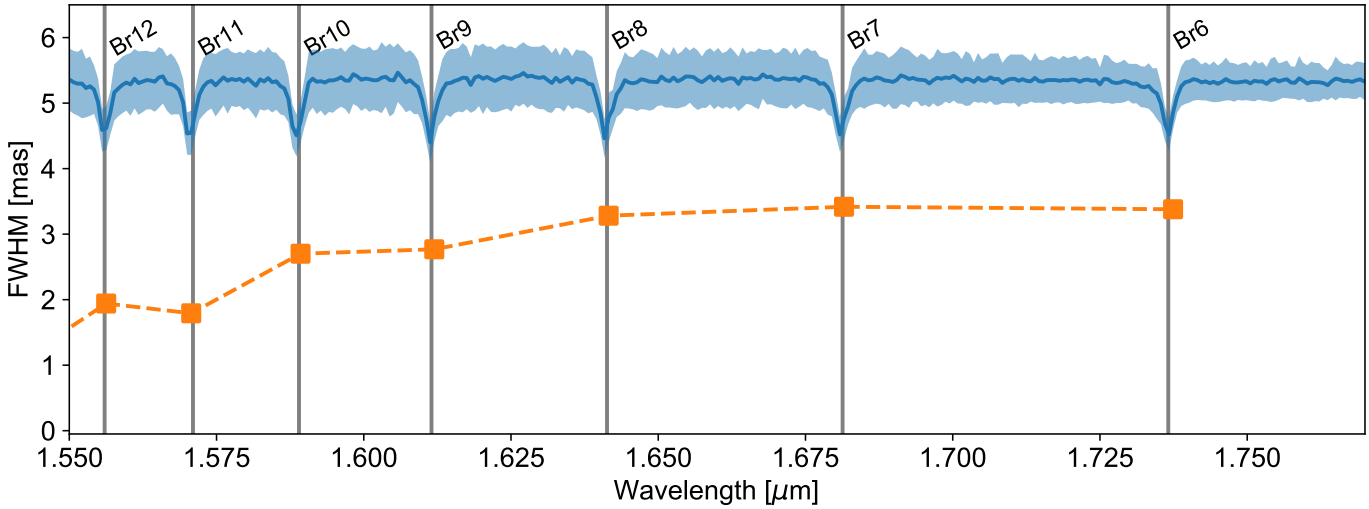

Figure 7.3.1: Wavelength dependent characteristic Gaussian FWHM size (blue line with shaded errors) calculated by modelling our AMBER MR-H spectrally dispersed visibilities. The orange points indicate the sizes of the pure line emission regions for each line, calculated using a two-component Gaussian model.

els and finding the best-fit with a ring model. Our own AMBER data effectively covers the entire H band with a much higher spectral resolution which illustrates clearly how the continuum visibility changes as a function of wavelength across the band. Additionally, the visibility levels that we observe were not compromised due to FINITO as we did not used the fringe tracker for our data acquisition. We adopt several of the best-fit parameters presented by Lazareff et al., namely the inclination, PA, and ring radius. The visibility clearly varies steadily across the H-band indicating that the morphology of the continuum-emission is wavelength dependent. Therefore, when modelling the continuum visibility the relative flux contributions of the star and disk, as well as the ring radius and width, are treated as wavelength dependent.

The stellar flux contribution varies steadily with wavelength between 20% at 1.55μm and 9% at 1.8μm. We find that the morphology of the disk also varies slightly with wavelength, with the ring radius decreasing with wavelength and the ring width increasing. The result of this is that the characteristic size of the emission remains similar, but that the ring becomes less "ring-like" and more "Gaussian-like" at longer wavelengths. This is consistent with the result discussed in Section 6.3, in which the MWC297 continuum emission is modelled with a Gaussian distribution in the longer-wavelength, K-band regime. The wavelength-dependence of the parameters was varied manually until a best-fit could be found for each, so it is likely that other variations of the parameters could be found that yield similarly good results. Having determined a good fit for the wavelength-

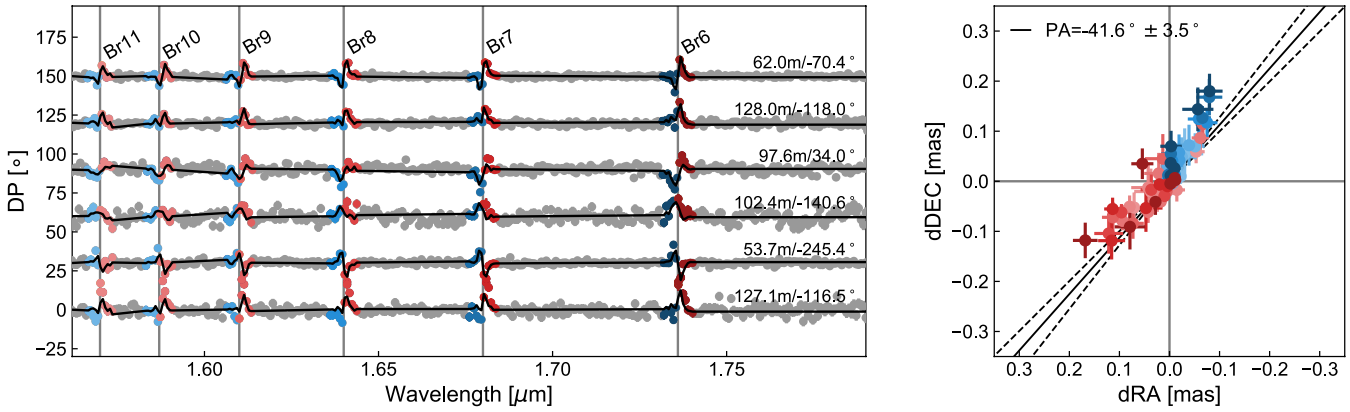

Figure 7.4.1: Right panel: Photocentre shifts for the Br-series lines + continuum determined from our AMBER MR-H data. The black line shows the best-fit position angle of the displacement between blue and red shifted vectors. Left panel: Differential phases for MWC297 observed with AMBER (circular points) compared with differential phases corresponding to the photocentre shifts shown in the right panel of this Figure (black lines). The grey points represent the continuum and the blue/red points represent the blue and red shifted photocentre shifts. The different shades of red and blue represent different Br-series lines as can be seen in the left panel.

dependence of the continuum emission we adopt this model later in Section 7.5 for use with our kinematic model.

7.4 Photocentre shifts

AMBER spectro-interferometry allows us to measure the differential phase, a quantity that provides the information of small scale physical displacements between material emitting in different spectral channels. By measuring the differential phase across a spectral line we can directly observe how the location of the line-emitting material differs from the location of the continuum emission across multiple spectral channels. We can calculate the photocentre displacement vector, $\vec{p}$, of a spectral channel by solving the set of linear equations put forward in Equation 6.5.1. We use the data of many baseline vectors simultaneously, finding the best-fit photocentre vector using the Nelder-Mead simplex algorithm. It is worth noting that the Eq. 6.5.1 is based on the assumption that the science target is marginally resolved which, given that MWC297 is fully resolved in the H-band, could mean that the photocentre approximation is inadequate in this case. For each of the line transitions in the Brackett series we split photocentre shifts to blue and red-shifted vectors relative to the line centre. The blue and red-shifted wings of each line extend to -750kms^{-1} and 750kms^{-1} respectively.

The resulting combined photocentre shifts for Br6-11 are shown in the right-hand panel of Figure 7.4.1 with the corresponding differential phases shown in the left-hand panel. We detect a clear displacement between the red- and blue-shifted vectors along a position angle of $\sim 41.6^{\circ}$, with the blue-shifted vectors to the North-west and the red-shifted vectors to the South-east. Additionally, several of the more displaced photocentres exhibit a slight shift to the North-east, perpendicular to the perceived angle of motion traced by the overall photocentre displacement pattern. This is a similar effect to the arc-like structures that were reported for MWC297 in Hone et al. (2017), as well as for other objects by Kraus et al. (2012a, b).

Having performed the same photocentre analysis for each of the Brackett series lines (Br6-11) we are able to compare the photocentre displacements patterns for each spectral line. We observe that the lower series lines (i.e Br6, Br7...) have larger spatial displacements than the higher-order lines (such as Br11). This is most likely due to the increased intensity of the Brγ emission from the lower-order lines leading to an increase of the amplitude of the differential phase. This could also be thought of as the higher-order lines having more contribution from the continuum emission shifting the lines towards zero displacement. Further discusson of the axis of motion PA traced by the photocentre shifts will be presented in Section 7.6.

7.5 Kinematic modelling

Using our kinematic modelling code we construct a model that is capable of modelling each of the emission lines in the Brackett series as well as the continuum emission, all varying as a function of wavelength. In order to do this it is necessary to analyse the line emission to determine how the relative line strength varies, either by wavelength or by the transition number. We find that the flux of the line emission relative to the continuum flux varies roughly linearly with wavelength (see Figure 7.5.2, left panel), following the relation $F_{\text{line}} = 2.5\lambda - 3.6$.

Our versatile kinematic modelling code (described in Section 4.5.1) allows us to model a range of kinematic scenarios including Keplerian rotation and disk winds without performing detailed physical calculations of the gas density or temperature. In Hone et al. (2017) we put forward the idea that a deviation in the perceived axis of rotation (as is traced by the photocentre shifts for the Brackett series, Figure 7.4.1) from the disk major axis can be caused by the presence of an additional out-of-plane velocity component, such as in a disk wind. We set up our model using the well constrained disk geometry deduced

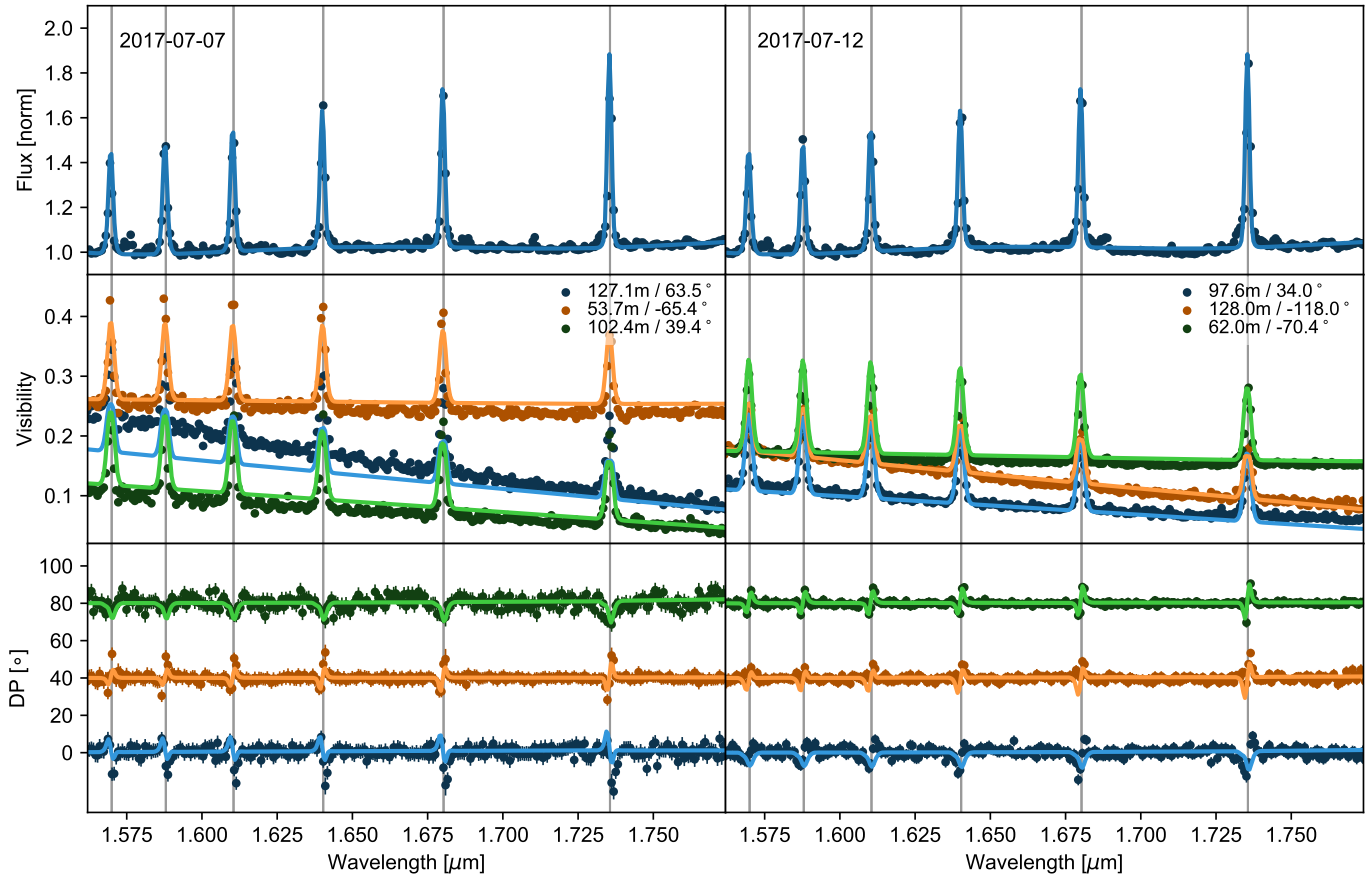

Figure 7.5.1: Comparison of our global kinematic model of the H-band with the VLTI/AMBER MR-H spectrum (top panels), wavelength-dependent visibilities (middle panels) and differential phases (bottom panels). The observed data is shown as dark-coloured points and the simulated data from the model is shown as light-coloured lines, with each corresponding colour matching to a different baseline.

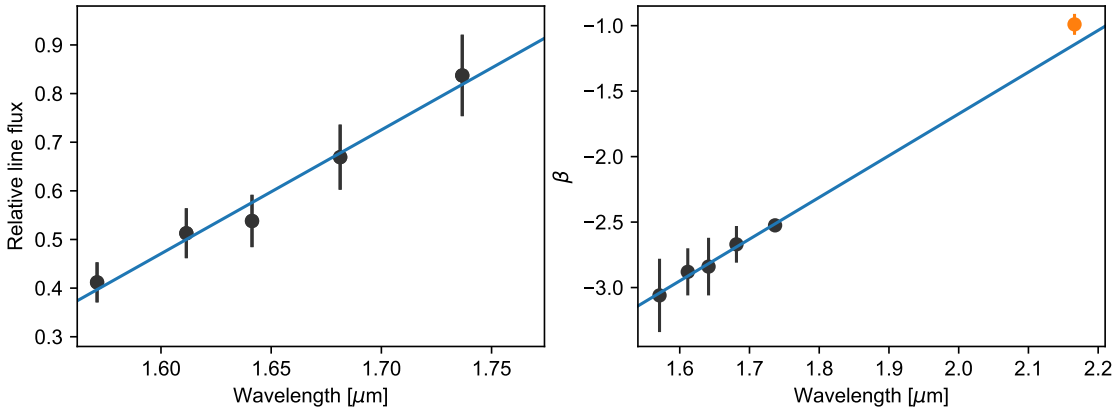

Figure 7.5.2: Left panel: best-fit line flux relative to continuum flux for Brackett series lines as a function of wavelength. The grey points are the best-fit parameters and the blue line represents a linear fit following the relation $F_{\text{line}} = 2.5\lambda - 3.6$. Right panel: best-fit radial intensity gradient β for Brackett series lines as a function of wavelength. The grey points are the best-fit parameters and the blue line represents a linear fit following the relation $F_{\text{line}} = 2.5\lambda - 3.6$. The orange point represents the best-fit β value obtained from our previous fitting of the Brγ emission from MWC297 in Section 6.7. For both panels Br10 and Br12 are omitted from the individual fits to speed up the fitting process.

by Lazareff et al. (2017), varying the size and intensity distribution of the line-emitting region as well as the out-of-plane velocity v_z. The inner and outer radius of the line-emitting region are defined by the opening angles of the wind acceleration streamlines (a schematic showing this is found in Figure 6.7.1).

We separate each of the line transitions and construct a series of kinematic models in order to determine the best-fitting parameters for each of the Brackett series lines. We vary the inner and outer radii (R_{in} and R_{out}) of the line-emitting region, along with its radial intensity index (β). For each of the lines in the Brackett series, the wavelength-dependent visibilities are best-fit with an inner line-emission radius of 0.1mas. Adopting the distance of 375.6pc calculated using GAIA DR2 parallax data (Gaia Collaboration et al., 2018; Bailer-Jones et al., 2018) and the stellar radius of $5.3R_{\odot}$ this angular separation corresponds to a distance of $1.5R_{\star}$. The inner radius found as the best-fit value is at the very limit of our model's spatial resolution, so it is possible that the inner edge of the line-emitting region extends closer to the central star in some cases. For all the Brackett series lines the best-fit radial intensity profile naturally rapidly decays to a negligible value inside the outer radius, similar to a Gaussian distribution. The visibility is strongly dependent on the line flux, so it is essential that the flux is fitted simultaneously with the other parameters.

As the disk position angle is fixed in our model, the differences in the differential phase

between our model and the data are accounted for by varying the disk wind's velocity. As has been previously discussed in Hone et al. (2017), the out-of-plane velocity of a disk wind causes a shift in the perceived direction of the motion traced by the differential phase. From our modelling in this case we find that the magnitude of this shift appears to change as a function of the disk inclination and the collimation of the wind. The offset of the disk wind source (see Figure 6.7.1) remains fixed to the same value (1.1mas) as was previously presented in Hone et al. (2017). As each Brackett series line shares the same inner radius of 0.1mas, this leads to a wind inner opening angle of $\approx 5^{\circ}$. In addition to a comparison between the model differential phase and the data, we use the data synthesised from our model images to calculate photocentre shifts and compare them to those presented in Section 7.4. We incrementally increase the v_z value of our model, testing the fit to the photocentre displacement angle and the differential phase, finding a best-fit v_z value of 220kms^{-1}.

We compare the best-fit parameters for each spectral line to determine which of the model features vary with wavelength. A different best-fit β value is found for each of the spectral lines in the Brackett series and we find that the variation of β is best described by a simple linear relation (Figure 7.5.2). We do not measure any significant difference in the best-fit inner radius of the line emission so it remains constant for each of the different emission lines.

To construct a global model for the whole H-band we calculate intensity maps for each of the wavelength channels. We sample the wavelengths with a high spectral dispersion before convolving the model to the spectral resolution of AMBER's MR mode. We take the linear fits for the line flux and β and implement them into our model as well as taking the best-fit parameters that do not vary as a function of wavelength. The resulting model is visualised in Figure 7.6.2 and a comparison between the model and the AMBER data is shown in Figure 7.5.1.

7.6 Discussion

We detect a variation in the size of the emission region for the different Brackett series lines across the H-band. For each of the Br-series transitions the emission region extends extremely close to the central star, with a best-fit inner radius of $\sim 1.5 R_{\star}$. As the observations do not fully resolve the inner edge of the emission it is possible that the line-emitting gas extends even closer to the stellar surface. For each of the lines we do

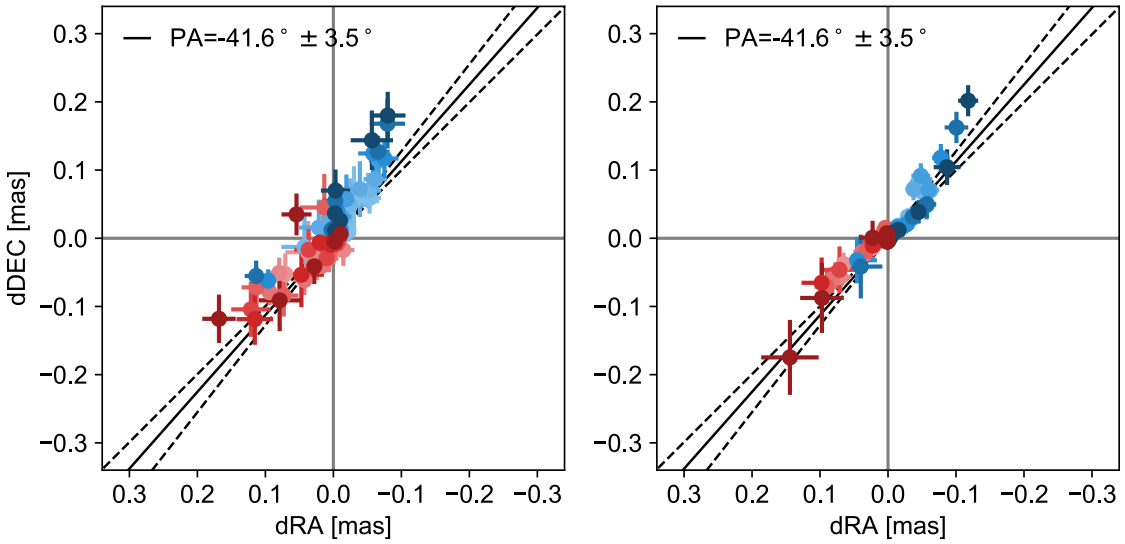

Figure 7.6.1: photocentre displacements calculated from our AMBER differential phase data (left panel) and our kinematic model (right panel). The model that produces photocentre shifts with a similar axis of motion to the data has an out-of-plane velocity (v_z) of 220kms^{-1}. The PA indicated in the top left of each figure is the best-fit axis-of-motion PA for the AMBER photocentre shifts.

not detect a strong "bounce" in the second lobe of the visibilities, indicating that the line emission region has no hard outer edge. In our model, the changing size of the emission region is modelled by changing the power-law of the radial brightness distribution. The intensity of line emission radially decays at a different rate for each line (Figure 7.5.2, right panel), with the decay rate decreasing as the wavlength increases.

Each of the Brackett series lines are emitted by hydrogen gas under different physical conditions, such as density and temperature. Analysing the line emission regions of each spectral line, we can infer the thermodynamic structure of the inner regions of the disk. Several works exist (e.g. Bary et al., 2008; Kwan and Fischer, 2011; Edwards et al., 2013) which aim to utilise the ratios between different emission lines to yield information about the temperature and density of the line-emitting material. Combining this approach with spatially-resolved, interferometric observations of the line-emitting material is an exciting prospect, but remains out of the scope of this study as it is presented in this thesis and will be presented as part of a peer-reviewed paper in the future.

Calculating the photocentre displacement vectors from the differential phase is extremely useful, as it provides model-independent insights into the kinematics traced by an emission line. Obtaining the photocentre shifts for many different lines tracing similar kinematics allows us to constrain the displacement angle between the blue- and red-shifted emission with greater significance. This displacement appears along a position angle of

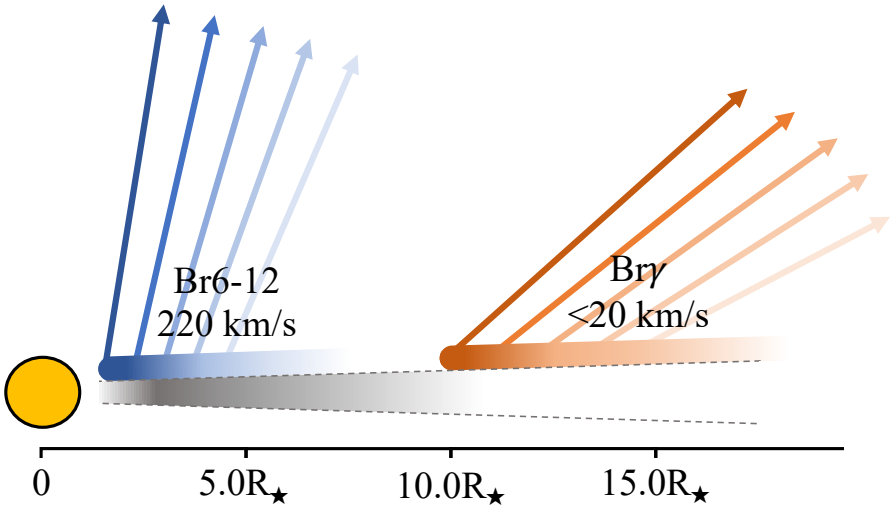

Figure 7.6.2: A schematic of the inner region of the MWC297 disk, incorporating results from this study as well as the study previously discussed in Chapter 6. The H-band Brackett series lines trace a collimated disk wind with a poloidal velocity of 220kms^{-1} originating from a compact region close to the central star, whilst the Brγ emission traces a less collimated disk wind with a poloidal velocity of $\sim$20kms^{-1} that is more extended than the continuum emitting disk.

$-41.6^{\circ} \pm 3.5^{\circ}$, a value that is displaced from the continuum position angle of $\sim 104^{\circ}$ (or -76°) by $\sim 34^{\circ}$. A similar displacement in the Brγ emission was noted in Hone et al. (2017), with the perceived rotation along an axis of $\sim 114^{\circ}$ differing from the K-band continuum major axis ($\sim 100^{\circ}$) by an angle of $\sim 14^{\circ}$. Here we can see that the displacement angle of the perceived rotation is different for Brγ than it is for the other Brackett series lines in the H-band. This difference suggests that the effect causing the displacement of the perceived axis of motion is comparatively stronger for the higher order Brackett series lines than it is for Brγ, alternatively the different line trace a significantly different velocity field.

As was previously discussed in this section, the increased line strength for lower-order lines is due to, at least in part, the increased size of the line-emitting region at longer wavelengths. Due to its location further out in the disk this material exhibits much lower velocity, both rotationally and in the out-of-plane direction. In the case of a disk where the out-of-plane velocity increases with decreasing radius, material further out in the disk exhibits a velocity field that is closer to Keplerian rotation. In this case it follows that the stronger emission lines, which contain more material further out in the disk, would have a perceived rotational PA that is closer to the disk major axis PA.

We do not see a significant change in the PA of the axis of motion for each of the different

lines from Br6 to Br12. In the previous study of the Brγ emission (Hone et al., 2017) the difference between the perceived rotation axis and the disk PA was shown to be $\sim$10°, whereas for the H-band Brackett lines the displacement angle is $\sim$34°. The strength of the Brγ line is $\sim$550% of the continuum flux, whereas the H-band Brackett lines have strengths that vary from $\sim$80% to $\sim$40% of the continuum flux. We can estimate from this that the motion axis difference between Br6 and Br12 will be approximately:

$$\frac{80\% - 40\%}{550\% - 80\%} \times (34^\circ - 10^\circ) = 0.085 \times 24^\circ = \sim 2^\circ. \tag{7.6.1}$$

This value is smaller than the uncertainty in the H-band Brackett series axis of motion, 3.5° (see Figure 7.4.1), demonstrating why we do not see a significant change in the PA of the axis of motion across Brackett series lines in the H-band. In the future, it will be useful to test the connection between the H-band Brackett lines and Brγ by observing Br4 and Br5 with spectro-astrometry or spectro-interferometry. However, the wavelengths of these lines are in a region of high atmospheric absorption and so must be observed from space, where there are currently no instruments that can achieve this.

Hone et al. (2017) noted the presence of a looping, arc-like structure in the photocentre shifts traced by the Brγ line. This structure also appears in the photocentre displacements of the Brackett series lines, illustrated in Figure 7.4.1, although to a lesser extent than for Brγ. The arc in the photocentre shifts was previously interpreted as an obscuration of the more distant region of the disk, possibly caused by optically thick material being ejected out of the disk plane in a wind. As the H-band traces a much more compact region of the disk than the K-band, it follows that the obscuring effect is stronger in the more extended regions of the disk that are not traced by these lines. Our observations of the outflowing velocity field suggest that this obscuring material is the likely caused by the ejection of dust in a disk wind (Bans and Königl, 2012) rather than a dusty magnetically supported atmosphere (Turner et al., 2014).

Using our kinematic modelling code we derive the properties of the MWC297 disk wind velocity field in the H-band and compare our results to previous studies of the same object in the K-band. The differential phases synthesized from our kinematic model frames are a good match to the observed AMBER data. By observing with AMBER's medium spectral dispersion mode we sacrifice the ability to resolve the kinematics of the line-emitting gas in favour of covering a wide range of wavelengths. Additionally, our uv-coverage spans only $\sim$50% of the full range of angles available, insufficient for fully fitting the velocity field of a kinematic model. By calculating photocentre shifts from the synthesized data we introduce another point of comparison between the model and data, made possible by

the model-independent nature of the photocentre shifts (see Figure 7.6.1 for a comparison of the photocentre shifts calculated from our data and the kinematic model). We find that the compact region of the disk wind traced by the Br6-12 lines exhibits an out-of-plane velocity of $\sim$220kms^{-1}, an order of magnitude faster than the out-of-plane velocity of the model for Brγ ($\sim$20kms^{-1}). An overall schematic of the inner regions of the MWC297 disk is shown in Figure 7.6.2. This feature of the data is mirrored in theories of jet formation (Ferreira et al., 2006; Romanova et al., 2009), which indicate that outflows have multiple components, including compact fast axial jets and more extended slow conical winds. Other models of the jet-launching region of T Tauri star suggest that the azimuthal magnetic field is stronger closer to the central star, leading to increased acceleration out of the disk plane in this region (Goodson et al., 1997; Romanova and Owocki, 2015). The direct detection of the poloidal velocity of the disk wind decreasing with radius is a unique and profound result that has significant implications for the study of jet launching from young stars.

7.7 Outlook

The study above represents a unique opportunity to conduct a detailed study of a young stellar object across multiple line transitions. I have demonstrated how such studies can provide novel insights into the star formation process and the launching of outflows from the inner regions of circumstellar disks. The data analysed in this chapter was among the last taken with AMBER, which was decomissioned in 2018. This means that the study can not be repeated with any of the current generation of beam combiners, and replicating the study for other objects will not be possible until a new instrument with this capability is commissioned. By publishing this work I hope to demonstrate the effectiveness of multi-line spectro-interferometry for studies of the jet-launching region of young stellar objects.

An interesting technique that I implemented in this work is the construction of photocentre shifts from the model data and the subsequent comparison of the model photocentre shifts with the AMBER photocentre shifts. This extra comparison point proved vital to determining the poloidal velocity of the wind. The true impact of the poloidal velocity only became evident when comparing the photocentre shifts of the model and the data, demonstrating the usefulness of such "second-order" comparisons. Any adverse effects of the sparse *uv*-coverage are also taken into account when photocentre shifts are calculated meaning that comparison between the model and data is fair.

Chapter 8

A compact gaseous accretion disk in Keplerian rotation around MWC147

This chapter is based on a paper that was published by Hone et al. (2019) in Astronomy & Astrophysics Volume 623 (Article 38).

8.1 Introduction

In this chapter, I present the resuts of the second major project that I undertook during my PhD, in which I studied MWC147 with interferometry and spectroscopy. The target was selected based on interesting properties that had been detected in previous studies, such as the double-peaked Brγ line profile detected with CRIRES and the evidence for continuum emission from the inner gaseous disk presented by Kraus et al. (2008b). High-spectral resolution ($R = 12,000$) interferometry data has only so far been presented for a handful of YSOs, so this MWC147 data set represents an exciting opportunity to provide new physical insights into the dynamic processes in the inner disk. The initial MWC147 data set was much much smaller than the MWC297 data set, only containing one HR-K observation with sufficient SNR along with two MR-K observations and some CRIRES spectroscopic data. This presented its own challenge, as kinematic modelling becomes a process that yields many degenerate results, especially considering that the AMBER HR-K data has considerably lower SNR than the MWC297 HR-K data set discussed in the last chapter, reflecting the lower apparent brightness of MWC147. During the project, the opportunity was presented to use some CHARA data, allowing me to focus on modelling

the inner disk continuum emission along with the analysis of the Brγ.
In this Chapter I will analyse data taken for MWC147 using AMBER spectro-interferometry (with a variety of spectral dispersions), CHARA interferometry and CRIRES spectroscopy. In Section 8.2 I will present the different data sets, along with the data reduction processes that were performed for each data set. In Section 8.3.1 the AMBER LR and CHARA/CLIMB data sets are analysed by fitting the visibilities with geometric models. The AMBER MR and HR data are interpreted in Section 8.3.2 by measuring the 2D photocentre displacements across the Brγ line. In Section 8.4 I will present kinematic modelling of the AMBER MR and HR data using a model of a compact gaseous disk in Keplerian rotation. Analysing the full data set revealed the presence of line-emitting gas in the same region as the continuum emission, close to the central star.

8.1.1 Previous studies of MWC147

MWC147 (HD 259431) is a $6.6 M_{\odot}$ Herbig Be star (spectral type B6) which is host to a circumstellar accretion disk (Hillenbrand et al., 1992; Polomski et al., 2002). Hernández et al. (2004) determined that MWC147 has a luminosity of $10^{3.19} L_{\odot}$ ($1549 L_{\odot}$) and is at a distance of 800 pc, however we adopt the new distance of 711 ± 24 pc measured by Gaia DR2 (Gaia Collaboration et al., 2016, 2018) using the more robust geometric distance calculation of Bailer-Jones et al. (2018). Bouret et al. (2003) used the FUSE UV spectrograph to examine the far-UV line emission originating from MWC147 and determined the stellar radial velocity to $V_{rad} = 43$ km/s. The first in-depth interferometric view of the disk around MWC147 was provided by Kraus et al. (2008b), using PTI, IOTA, VLTI/MIDI, and VLTI/AMBER data. Kraus et al. used the measured visibilities to determine the size and geometry of the disk around MWC147 across K band and N band, combining their visibility measurements with a fit to the SED. These authors found that the best-fit to the SED and the interferometry data was achieved using a model of a dust disk with an optically thick gaseous component inside the dust sublimation radius. This model suggests that the K-band emission is dominated by the accretion luminosity from the active, gaseous inner disk, whilst the mid-infrared (MIR) emission still contains the flux contributions from the irradiated dust of the disk rim.
Bagnoli et al. (2010) obtained optical spectroscopy on MWC147 in several emission lines including forbidden and permitted OI and MgII transitions. The highly symmetric, double-peaked [OI] line profiles suggest that the emission arises from a rotating circumstellar disk. By deconvolving the line profiles and determining the radial intensity profile of the line-emitting gas these authors determined that the disk transitions from a gaseous

disk to a dusty disk at radii of $\sim 2-3$ au, corresponding to the expected dust sublimation radius predicted by Kraus et al. (2008b). Similar analysis of the Mg[II] emission lines suggested an inner radius of the gas disk at ~ 0.1 au, close to the expected co-rotation radius.

Ilee et al. (2014) observed CO bandhead emission around several Herbig Ae/Be stars, including MWC147, using the XSHOOTER and CRIRES instruments at the VLT. They found that the CO emission was located in a disk ranging from 0.89 to 4.3 au with an inclination of 52°, in good agreement with the result from Kraus et al. (2008b). A recent interferometric study by Lazareff et al. (2017) used the VLTI/PIONIER instrument in the H band to analyse the circumstellar environment around several Herbig B[e] stars including MWC147. They were able to construct a detailed geometric model of the near-infrared emission, finding that it arose from a disk orientated with an inclination of $23 \pm 10°$, i.e. more face-on than the earlier estimates. Lazareff et al. also estimated a disk major-axis position angle (PA) of 44°. However, with an uncertainty of 42°, they were unable to place strong constraints on this value, a problem that is possibly compounded by the low (close to face-on) disk inclination.

The large-scale structures around MWC147 were studied by Li et al. (2014) who utilized deep MIR imaging to observe the surrounding diffuse nebula. In their study, Li et al. found that the shape of the nebula is highly asymmetric, with a bow-like structure extending from the central star along a PA of $\sim 120°$. Li et al. discussed the possibility that these complex filamentary structures could trace the inner walls of the cavity carved out by a bipolar outflow.

Using a variety of techniques, we aim to resolve the innermost regions of the protoplanetary disk of MWC147, determine the nature of the continuum emission, and probe the origins of the Brγ emission that arises in the inner disk. Combining interferometry data from multiple instruments we achieve the highest angular resolution interferometric observations of the MWC147 disk so far, interpreting our data with a geometric disk model to measure the orientation of the MWC147 disk system. We also combine medium- and high-resolution (MR; HR) spectro-interferometry with CRIRES spectroscopy to build a picture of the origin and kinematics of the Brγ-emitting gas, using a model-independent photocentre shift analysis as well as our kinematic modelling code.

Table 8.2.1: Observation log for our MWC147 data taken with VLTI/AMBER and VLT/CRIRES. The numbers in the calibrator column correspond to the following stars with their K-band uniform disk diameters in parentheses: (1) HD 53510 (2.049 mas), (2) HD 43023 (0.940 mas), (3) HD 47127 (0.411 mas), (4) HD 50277 (0.356 mas), (5) HD 47157 (0.276 mas), (6) HD 52456 (0.271 mas), (7) HD 47575 (0.225 mas), (8) HD 45638 (0.262 mas), and (9) HD 48977 (0.119 mas). The NDIT/Pointings column gives the NDIT for all observations except for CHARA/CLIMB, where it gives the number of pointings taken on the night. The baseline and PA columns give the average value across all pointings.

Instrument	UTC Date	Telescopes	UT	DIT	NDIT/Pointings	Proj. baselines	PA	Calibrator
			[h:m]	[ms]	#	[m]	[°]	
AMBER HR-K	2010-12-18	U2/U3/U4	06:15	1000	2100	43.5 / 59.2 / 89.2	-133.5 / -73.4 / -98.4	1
AMBER MR-K	2008-12-14	U1/U3/U4	07:29	500	1560	54.6 / 82.1 / 128.5	-144.2 / -103.3 / -119.4	2
	2009-12-04	U2/U3/U4	07:58	500	840	46.2 / 84.2 / 50.7	-133.5 / -102.3 / -74.1	3
AMBER LR-K	2008-12-15	U1/U3/U4	07:38	26	6000	101.0 / 47.2 / 128.0	-139.5 / -73.9 / -119.9	4
CHARA/CLIMB	2010-12-01	S2/W2/E2	-	21	3	162.5/218.8/154.6	20.6/-114.5/-246.6	5,6
	2010-12-22	S2/W1/E2	-	16	4	223.5/304.3/247.0	-14.8/-227.3/-76.4	5
	2012-11-28	S2/W2/E2	-	20	3	218.3/304.9/120.2	2.8/-195.8/-51.1	7,8
CRIRES	2010-10-26	U1	06:40	60000	36	N/A	N/A	9

8.2 Observations and data reduction

8.2.1 VLTI/AMBER interferometry

We observed MWC147 between 2008 and 2010 using the AMBER instrument at the VLTI. AMBER (Petrov et al., 2007) is a three-telescope beam combiner capable of obtaining spectrally dispersed interferometric data with a range of spectral resolutions ($R = 30$ to $R = 12\,000$). Our VLTI/AMBER observations are outlined in Table 8.2.1 and the *uv*-coverage of these observations is shown in Fig. 8.2.1 (left panel).

Two of our data sets were taken with the HR ($R = 12\,000$) mode of AMBER in the K band, which allows us to spectrally and spatially resolve the Brγ line from MWC147. Both of our AMBER HR-K data sets use the UT1-UT2-UT4 telescope triplet, which covers a range of baseline lengths from $\sim$56 m to $\sim$130 m. The first data set (2009-12-31, UT1-UT2-UT4) was recorded without external fringe tracking, but resulted only in a poor S/N. Therefore, we rejected this data set from further analysis. For the second observation (2010-02-18, UT2-UT3-UT4) we used the FINITO fringe tracker (Le Bouquin et al., 2009) to correct for atmospheric turbulence, which enabled integration times up to 1 second and resulted in a higher S/N. In addition to the high spectral dispersion observations we also used data taken with AMBER's medium-resolution ($R = 1\,500$, for which we also used FINITO) and low-resolution (LR; $R = 30$) mode.

Data reduction was performed using the same AMBER data processing software package as discussed in Section 6.2. We corrected for heliocentric line-of-sight velocities using the ESO Airmass tool. The visibility level of the continuum emission is calibrated using the best geometric model discussed in Section 8.3.1. This is a necessary step because of the unreliability of visibilities that are observed with FINITO. We detected a strong Brγ line ($\sim$70% above the continuum flux level), which causes the error bars in the line to be smaller than those in the continuum and as a result the continuum region has a poor S/N for our AMBER HR-K observations.

8.2.2 CHARA/CLIMB interferometry

The three-telescope beam combiner, CLIMB (ten Brummelaar et al., 2013), of the centre for High Angular Resolution Astronomy (CHARA) Array, was used to obtain *K*-band continuum interferometry (see Table 8.2.1). An array of six 1 m class telescopes, CHARA has operational baselines between 34 and 331 m (ten Brummelaar et al., 2005). Observing MWC147 with the CHARA baselines gives us the opportunity to better resolve the continuum emission and achieve a better estimate of the inclination angle and PA of the

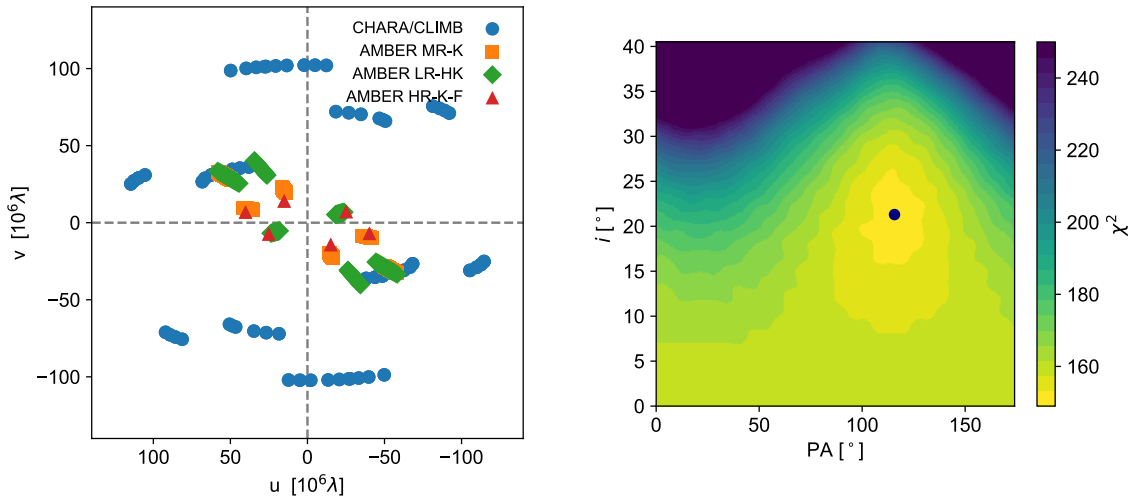

Figure 8.2.1: Left panel: *uv*-coverage achieved with our interferometric observations of MWC147 with both VLTI/AMBER and CHARA/CLIMB. Right panel: Two-dimensional χ^2 map showing the dependence between the best-fit model PA and the inclination of our ring model. The colour scale illustrates the total χ^2 for each value of the PA and inclination and the best-fit model values are indicated by the blue data point.

continuum disk, quantities that offer an important comparison with the perceived rotation angle of the Brγ-emitting gas (see Section 6.8). MWC147 was observed on five separate occasions with CLIMB between 2010 December and 2012 November, achieving a maximum baseline length of $\sim$300 m (corresponding to an angular resolution of $\sim$0.75 mas). The data were reduced using a pipeline developed at the University of Michigan that is well-suited to recovering faint fringes for low-visibility targets. Standard stars not known to be members of binary or multiple systems were observed before and/or after each science observation and used to calibrate the visibilities and closure phases (see Table 8.2.1 for the names and uniform disk [UD] diameters of the calibrators used[1]). A further inspection of the closure phase signals of the calibrators observed more than once was undertaken to check for the presence of binary signatures and none were found.

8.2.3 VLT/CRIRES spectroscopy

In addition to our interferometry data we also obtained HR ($R = 100\,000$) spectra for MWC147 in the K band using the VLT/CRIRES instrument (Kaeufl et al., 2004). Using CRIRES allows us to spectrally resolve the Brγ line with the best possible spectral dispersion, allowing us to resolve the finer structure of the line. This is crucial to distinguish between different kinematic line-emission scenarios. Our observations of MWC147 were

[1]UD diameters were retrieved from JMMC SearchCal (Bonneau et al., 2006, 2011)

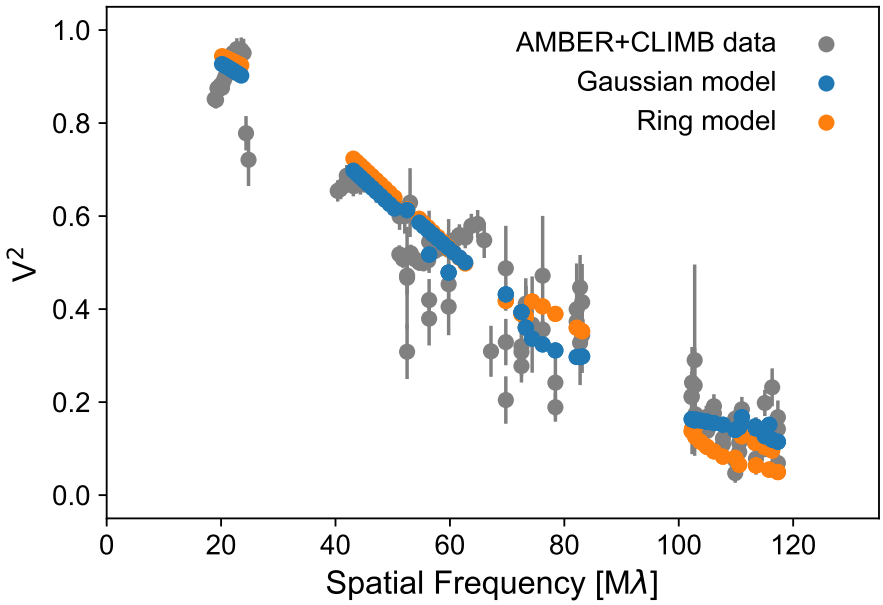

Figure 8.3.1: Visibility squared vs. spatial frequency (baseline length) for our VLTI/AMBER and CHARA/CLIMB data for MWC147. The observed data with uncertainties are shown in grey, whereas the results of our inclined Gaussian and ring models are shown in blue and orange, respectively.

taken using a slit width of 0.2”, 60-second integrations and using both the "nodding" and "jittering" techniques. The nodding technique involves taking an integration on the object at an initial telescope position A, moving (or nodding) the telescope to a second position B and taking two more integrations, then moving the telescope back to position A for a final integration. Jittering involves adding a small random offset to each of the nodding offsets. These techniques combine to remove sky emission, detector dark current and thermal noise as well as correcting for bad pixels and decreasing systematic errors. The raw data was reduced using the standard ESO pipeline in which the raw images are combined, spectra are extracted, and the wavelength is calibrated. We correct for intrinsic Brγ absorption in our calibrator (HD48977) before dividing the science spectrum by the calibrator spectrum.

8.3 Analysis of interferometric data

8.3.1 Geometric modelling of continuum emission

To determine the size and shape of the K-band continuum-emitting region we combined our CHARA/CLIMB and AMBER low spectral dispersion visibility data and interpret

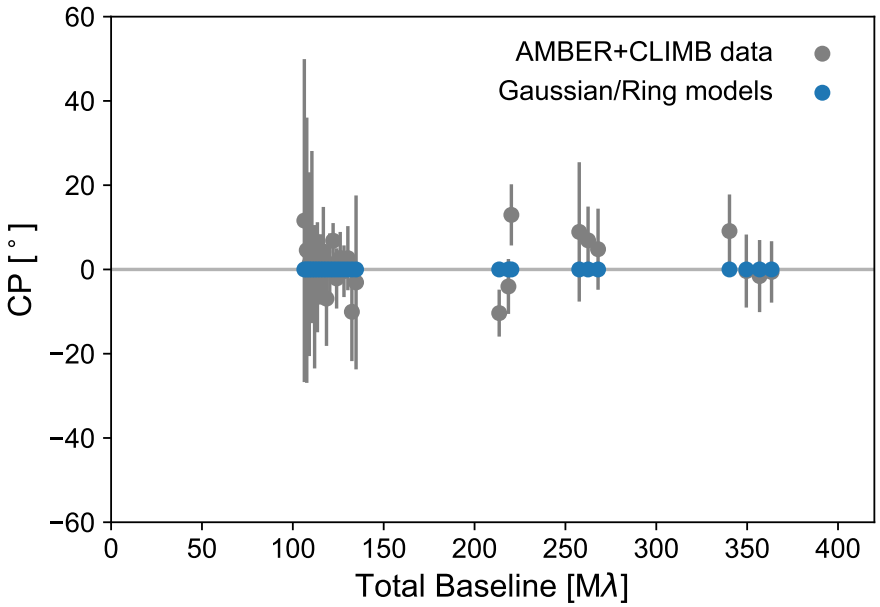

Figure 8.3.2: Closure phase vs. combined baseline length for our VLTI/AMBER and CHARA/CLIMB data for MWC147. The combined baselines length is calculated by summing the baselines for each closure phase triangle. The observed data with uncertainties are shown in grey, whereas the results of our inclined Gaussian and ring models are both shown in blue as they both have the same closure phase.

Table 8.3.1: Parameters for our best-fit geometric model featuring a star and inclined Gaussian or ring brightness distribution. The parameter θ indicates the PA of the major axis of the disk. The χ^2_r shown is calculated only using visibility data.

Parameter	Range	Gaussian value	Ring value
$F_\star$	-	17%±6%	16%
$F_{\rm disk}$	0 – 20	83%±6%	84%
FWHM	0 - 5 mas	1.21±0.1 mas	-
R	0 - 5 mas	-	0.60 ± 0.03 mas
dR	0 - 5 mas	-	0.2R
i	0° - 90°	21.3±6.4°	26.7°±4.7°
θ	0° - 360°	25.7±15.7°	42.4°±15.0°
χ^2_r	-	1.53	2.45

these data sets with a simple geometric model. Both CHARA and AMBER can also measure the closure phase (see Section 3.2). The closure phase is a useful observable for detecting the presence of asymmetries in the measured brightness distribution (e.g. Monnier, 2003) and is an important component for obtaining higher order information from interferometric observations. However, we find that the measured data from AMBER and CLIMB is consistent with zero closure phase, and very few data points exhibit a deviation from zero greater than 1σ and zero deviations greater than 2σ (see Figure 8.3.2). As such we model the visibilities and closure phases from AMBER and CLIMB with centrosymmetric geometric models and yield a χ^2_r of 0.5 for our CP data.

Using the Rayleigh criterion, $\theta = \frac{\lambda}{2B}$, we determine that our maximum baseline allows us to achieve an angular resolution of 0.68 mas. A two-dimensional elliptical Gaussian model is sufficient for our initial fitting where we focus on estimating inclination and PA; the precise geometry is not important for this goal as our baseline range only covers the first lobe of the visibility function (model parameters shown in Table 8.3.1). In addition we fit a simple ring model to our visibility data in order to compare the modelled ring radius with the expected dust sublimation radius. The uncertainties of our best-fit parameters are determined via bootstrapping (for a full description of this process see Davies et al., 2018).

In our Gaussian model we vary the FWHM, the disk major axis PA (θ), inclination (i), and the relative flux between the disk and star. We find that our best-fit model has a FWHM of 1.21 ± 0.10mas, which corresponds to 0.84 ± 0.074 au assuming a distance of 711 pc. We find that there is a loose dependence between the best-fit PA and inclination (illustrated by the χ^2 map in Figure 8.2.1, right panel). The χ^2 map in figure 8.2.1 (right panel) also shows a strong degeneracy in the PA value at low inclinations, possibly due to the low inclination that we observe for the disk. Our best-fit model has a stellar flux contribution ($F_\star/F_{\rm Tot}$) of $17\% \pm 6\%$, which is consistent with the stellar flux contribution value of 16% determined from the SED in Millan-Gabet et al. (2001); Kraus et al. (2008b).

We also modelled our VLTI+CHARA visibility data set with a two-dimensional ring brightness distribution. This model has the same use of the inclination, PA and disk flux parameters, but with the ring radius R as free parameter and constant ring width of $0.2R$ (Monnier et al., 2005). The fit yields a ring radius of $R = 0.84$ mas and an (unrealistically) high stellar flux contribution (49% of the total flux). We also fit the visibility data with a ring model in which we allow the relative width of the ring to vary, which results in similar values for the best-fit PA and inclination as the model with fixed ring width (within 1σ). However, it is clear that the algorithm does not favour a ring-like brightness distribution,

with a ring radius of 0.12 mas, a ring width of $9.9R$ ($\sim$ 1.2 mas), and a stellar flux contribution of $\sim 42\%$. Both of the aforementioned models appear to strongly overestimate the stellar flux contribution compared to analyses that tried to separate the star/disk flux contributions from the SED (16% Millan-Gabet et al., 2001; Kraus et al., 2008b). This is likely due to a well-known degeneracy that exists between the best-fit ring radius and stellar flux contribution when fitting visibility data in the first lobe of the visibility function (Lachaume, 2003; Lazareff et al., 2017). Therefore, we also conducted fits where we fix the stellar flux contribution to the SED value. Assuming again a fixed-width ring of $0.2R$, we derive a ring radius of 0.60 ± 0.01 mas (see Table 8.3.1 for full list of best-fit parameters). We adopt this model as our best-fit ring model, although it is important to note that this model does not account for any other potential sources of flux other than the ring and therefore can only be considered an approximation to the true brightness distribution. Our best-fit ring radius of 0.60 ± 0.01 mas corresponds to a physical distance of 0.39 ± 0.01 au assuming that the distance to MWC147 is 711 pc. This region of the disk is 3.9 times more compact than the expected MWC147 dust sublimation radius of 1.52 au assuming a dust sublimation temperature of 1800 K. Our Gaussian model achieves a better fit to the visibilities than our ring model (see the χ^2_r values in Table 8.3.1), although both models feature similar values for inclination and PA; this means that each model finds a similar best-fit disk orientation. The improved χ^2_r for our Gaussian model is reflected by the results of our variable-width ring fit, which tends towards a Gaussian-like brightness distribution, suggesting that we are marginally resolving the brightness distribution. Our best estimate for the orientation of the MWC147 system is an inclination of $19.2 \pm 1.7^\circ$ and a major axis PA of $12.7 \pm 12.1^\circ$; these parameters are derived from our kinematic model, but are also consistent with our geometric modelling of the system.

8.3.2 Photocentre analysis of Brγ emission

We detect that for many of our observed baselines the differential phase deviates from zero in the Brγ line (such as can be seen in Figure 8.4.2), an effect that is caused by the centre of the emission in a particular wavelength channel deviating from the centre of the continuum emission. By qualitatively analysing the differential phase patterns across the Brγ line we can glean information about the differing kinematic scenarios traced by the line emission. The "S-shaped" differential phases that we can see for several of our baselines (see Figure 8.3.3, right panel) are an indicator of rotation, as we see that the blue-shifted emission is symmetrically displaced opposite to the red-shifted emission. By

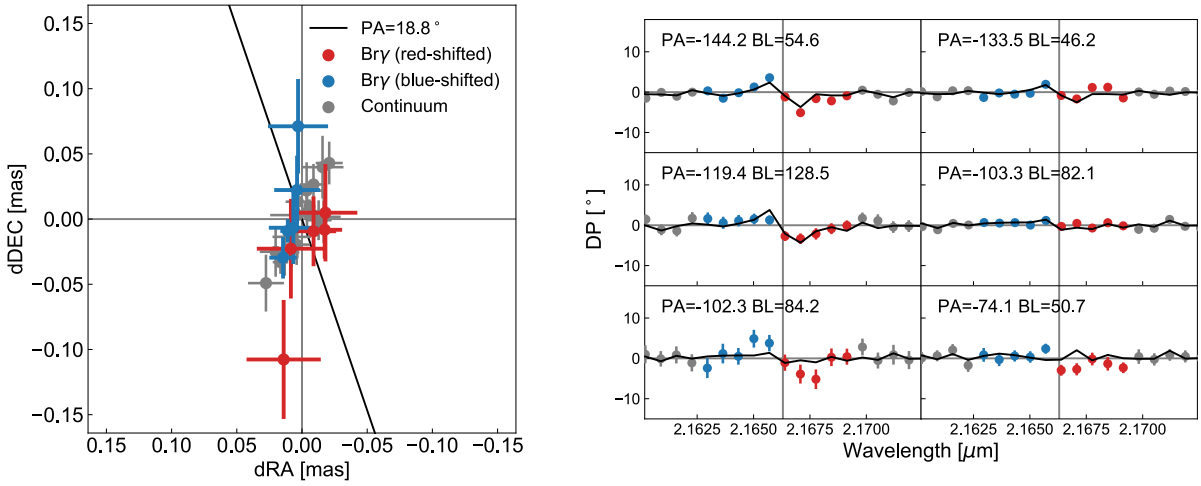

Figure 8.3.3: Left: Derived 2D photocentre displacement vectors for the Brγ line + continuum determined from our AMBER MR-K data. The black line shows an estimated PA for the displacement between blue- and red-shifted vectors. Right: Differential phase (DP) data for MWC147 observed with AMBER's MR-K mode (points) compared with differential phases calculated from the photocentre shifts shown in the right panel of this Figure (black lines). The baseline label in the upper corner gives the PA in degrees and the baseline (BL) in metres. The line (red and blue) and continuum (grey) points from the left panel correspond to the similar coloured points in the right panel.

combining the differential phases for multiple baselines and PAs we can derive a two-dimensional photocentre displacement profile which reveals the PA of the rotation traced by the line emission. These photocentre displacements can be compared with the continuum disk geometry that we measure in the previous section and can help to constrain the PA of the disk major axis.

To derive the wavelength-dependent photocentre shifts from our differential phase data we use the fitting method outlined in Section 6 based on equation 6.5.1. Examining our photocentre displacement vectors, we see a displacement between the blue- and red-shifted vectors along a PA of $\sim$18.8° (see Figure 8.3.3). This angle is estimated by determining the mean displacement for the blue-shifted and red-shifted vectors and calculating the displacement angle between the two mean vectors. The extension of the data points in the north-south direction is caused by the non-uniform uv-coverage, and is orientated along the direction of least resolution (see Figure 8.2.1, left panel). Our geometric model of the continuum disk indicates a disk major axis PA of 25.7$\pm$15.7° for the continuum-emitting disk which is consistent with the estimated rotation angle derived from our photocentres. In the next section we use a kinematic model to construct a more detailed interpretation of both the differential phases and visibilities of the AMBER MR and HR data.

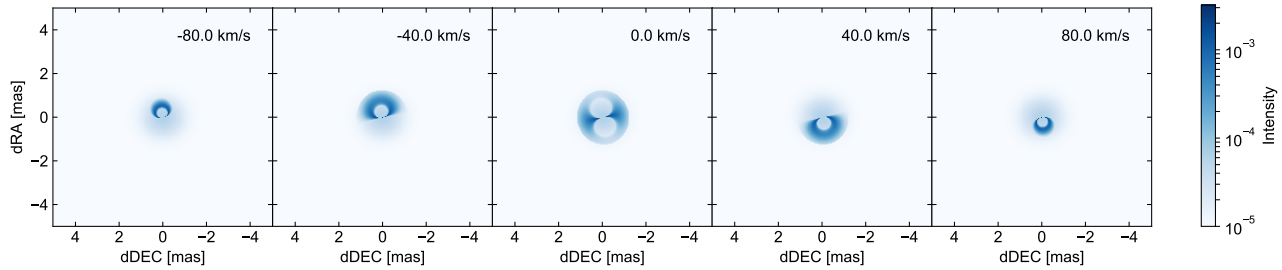

Figure 8.4.1: Synthetic model images calculated for our Keplerian accretion disk model for five spectral channels across the Brγ line. We use an arbitrary logarithmic colour scale to show the flux distribution with more detail. The parameters for this model can be found in Table 8.4.1.

8.4 Kinematic modelling

In order to constrain the gas velocity field around MWC147 we fit a kinematic model to our AMBER MR and HR data, as well as the CRIRES spectra. We use the kinematic modelling code that we have already used for modelling spectro-interferometric observations for a range of evolved (Weigelt et al., 2007; Kraus et al., 2012a) and young objects (Kraus et al., 2012c; Hone et al., 2017). Based on an analytic description of 3D velocity fields and the radial brightness distribution, this code allows us to compute synthetic spectra and synthetic images for different velocity channels in a spectral line. This type of modelling is a useful tool to explore how different disk morphologies and variations of the velocity field fit the observed visibilities and differential phases.

Using our kinematic modelling code we compute synthetic intensity distribution frames for each spectral channel that include contributions from both a continuum-emitting disk and Brγ-emitting component. The continuum emission is modelled as an inclined two-dimensional Gaussian identical to the one determined in Section 8.3.1. The line-emitting region extends from an inner radius, R_{in}, to an outer radius, R_{out}, and has a radial brightness following the power-law $\propto r^{\beta}$, where r is the radius and β is a power-law exponent. The disk major-axis PA (θ) and inclination (i) are treated as free parameters with starting values taken from our fitting of the continuum disk. To avoid unphysical sharp edges in our model images we use a Fermi-type smoothing function to model the edges of the disk (see Kraus et al., 2008b). We adopt the stellar parameters (mass $M_{\star}$ and distance d) quoted in Sect. 8.1. From the resulting 3D image cube we compute the wavelength-dependent interferometric quantities for the uv-coordinates covered by our data.

In order to determine which kinematic scenarios to explore we evaluated our observed AMBER and CRIRES data. We do not see a significant variation in visibility across

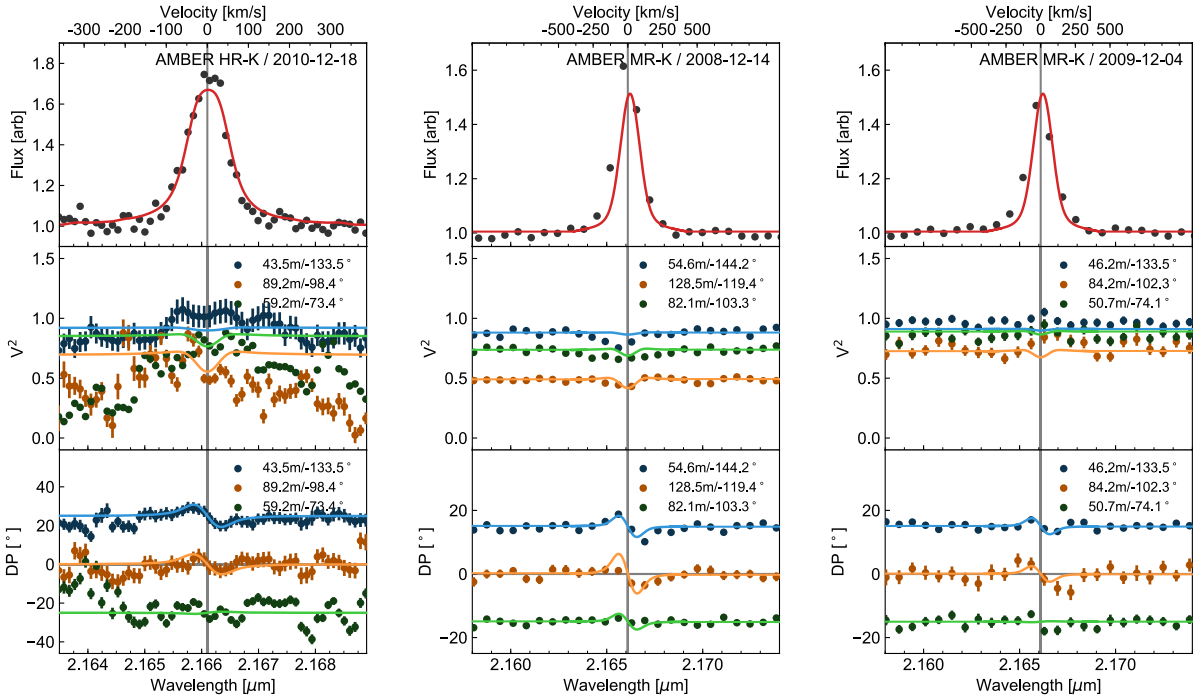

Figure 8.4.2: Comparisons of our observed interferometric data (coloured points) with synthesised data from our kinematic model (solid lines). Our AMBER HR data is shown in the left panel; our two AMBER MR epochs are shown in the middle and right panels. Each plot shows the spectrum (top), squared visibilities (middle), and differential phases (lower) calculated from our kinematic model and compared to our observed VLTI/AMBER data. The different coloured lines correspond to the different observed baselines, which are labelled in the upper right corner of the panel.

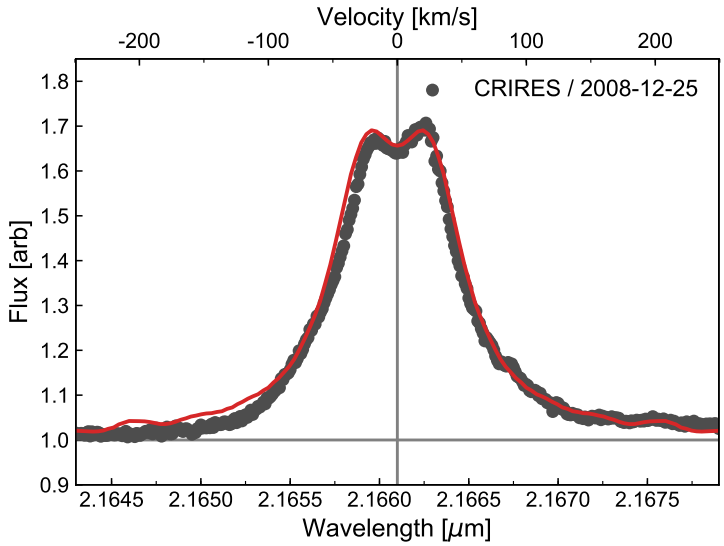

Figure 8.4.3: Spectrum calculated from our kinematic model and compared to our observed VLT/CRIRES data for the Brγ line. The solid red line represents the model spectrum and the grey points represent the observed CRIRES spectrum.

the line, indicating that the Brγ emission originates in a similar compact region as the continuum disk. The innermost stream lines of the disk wind region (and the X-wind region) may be located near the corotation radius ($\sim$0.1au), therefore the measured radius of $\sim$1au of the Brγ-emitting region is consistent with the expected emission region of a disk wind. Additionally, the observed CRIRES spectrum (shown in Figure 8.4.3) shows a highly symmetric, double-peaked Brγ line profile which is indicative that the line emission arises in a velocity field that is either purely rotational or does not contain a significant out-of-plane velocity component. This suggests that the emission arises from the disk surface or a region very close to it, where material ejected by a possible disk wind is not yet significantly accelerated and therefore the velocity field is still approximately Keplerian. Taking our conclusions from analysis of this data, we elect to model the Brγ emission around MWC147 with the simpler case of a gaseous disk in Keplerian rotation. Our model is at first calculated with a spectral resolution comparable to that of CRIRES (as it is our highest spectral resolution data). To compare our model quantities to our lower spectral resolution AMBER data we convolve our model to spectral resolutions of AMBER's HR and MR modes with a simple Gaussian kernel. Taking the results from Table 8.3.1 as initial values for our kinematic model parameters we construct a series of model grids, taking the model with the lowest χ^2_r as our best-fit model, the parameter values of which are shown in Table 8.4.1. The best-fit model brightness distribution for five velocity channels can be seen in Figure 8.4.1 and the comparison between

our observations and the synthesised observables from the model can be seen in Figures 8.4.2 and 8.4.3. After modelling the continuum disk with the same parameters from our AMBER/CLIMB fitting in Section 8.3.1, we tweak the parameters of the line-emitting region to find the best possible fit to the observed CRIRES spectrum and AMBER spectrum/visibilities. The precise shape of the model spectrum is highly sensitive to the disk inclination as well as the radial brightness distribution of the line-emitting region. By adjusting these parameters of our kinematic model we can match the full width of the high velocity spectral line wings as well as the double-peak structure that we see at very low velocities (in the line centre, see Figure 8.4.3). We alter the disk PA to best recreate the patterns we see in the differential phase data. The uncertainties of our model variables are calculated using the χ^2 method. Our kinematic model can reproduce the observed CRIRES spectrum with a reduced χ^2_r of 1.44 and the parameters of the model are listed in Table 8.4.1.

The differential phase measurements from our AMBER MR and HR data are reproduced with moderate success by our kinematic model. In particular, the overall shape of the model differential phase patterns is a good match to the observed data, but the magnitude of the phase is marginally too high or low for some baselines. The visibility levels for the two MR data sets are well reproduced (Figure 8.4.2, middle and right panels), although the changes in visibility across the line (whilst very small) are not well matched for our 2009-12-14 data. This could be due to inconsistencies between the data sets caused by intrinsic variability of the source, which we do not account for in our models. This is also reflected by the different line strengths shown in the two MR data sets. Our model achieves a χ^2_r of 0.56 for the visibilities ($\chi^2_{r,V}$) and a χ^2_r of 0.33 for the differential phases ($\chi^2_{r,\phi}$) leading to a total χ^2_r of 0.89. Whilst our model is a good match to the differential phases of our AMBER HR data set (Figure 8.4.2, left panel), the visibilities for this data set have a very low S/N and there are few coherent patterns visible for our model to replicate. The strength, width, and fine structure of the observed CRIRES ($R = 100\,000$) spectrum is very well reproduced by our kinematic model, but the slight variation that we see in the line strength for our different AMBER MR and HR data sets mean that the fit to the AMBER spectra is good but not perfect.

8.5 Discussion

Based on the measured bolometric luminosity of $1549\,L_\odot$ (Hernández et al., 2004), we expect that the dust sublimation radius should be located at ~ 1.52 au (assuming a subli-

Table 8.4.1: Ranges and best-fit values for our kinematic model parameters. The reduced χ^2 values (calculated using our AMBER HR data) for each of our best-fit kinematic models are also shown.

Parameter	Range	Best-fit value
R_{in}	0 - 5 mas	0.1±0.04 mas
R_{out}	0 - 10 mas	2.1±0.5 mas
θ	-180° - 180°	12.7±12.1°
i	0° - 90°	19.2±1.7°
β	−2.0 - 0.0	−0.8±0.1
$\chi^2_{r,V}$	-	0.56
$\chi^2_{r,\phi}$	-	0.33
χ^2_r	-	0.89

mation temperature of 1800K and grey dust opacities), corresponding to an angular diameter of ∼4 mas at the distance of 711 pc. Our findings show that the K-band continuum is much more compact, which suggests that the emission does not originate from the dust sublimation rim, but an alternate source located about 3.4 times closer in. This occurrence of undersized Herbig Be stars has been observed in several other high-luminosity objects in the size-luminosity study of Monnier and Millan-Gabet (2002). The compact nature of these objects has been interpreted in several ways, including an inner gaseous component that shields stellar radiation to let dust survive closer to the central star (Monnier and Millan-Gabet, 2002; Eisner et al., 2004; Weigelt et al., 2011) or additional emission components such as highly refractory dust grains (Benisty et al., 2010).

In the specific case of MWC147, Kraus et al. (2008b) suggested that the K-band continuum traces optically thick gas from a compact, viscously heated accretion disk. Kraus et al. combined near-infrared and mid-infrared interferometric data for MWC147 and found that models with a passive dust sublimation front were not able to reproduce the measured steep increase in the characteristic size of the continuum-emitting region (factor ~ 10 between 1 and 12 μm). However, they were able to obtain a good fit to the visibilities, closure phase, and SED by including an optically thick, gaseous accretion disk inside the dust sublimation rim. Measurements of the differential visibility do not show a consistent, significant variation across the Brγ line, suggesting that the line emission originates from a similar region to the K-band continuum. The presence of line-emitting gas that is

co-located with the continuum emission is strong evidence that the continuum traces an active, gaseous accretion disk inside the dust sublimation radius (as suggested by Kraus et al., 2008b; Bagnoli et al., 2010), rather than an irradiated disk wall or highly refractory dust grains.

Combining our geometric and kinematic models we attempt to obtain a precise estimate for the disk PA, a quantity which has been poorly constrained by previous studies using geometric models (Kraus et al., 2008b; Lazareff et al., 2017), possibly due to the close to face-on inclination of the disk. We construct a model-independent photocentre displacement profile using our AMBER MR differential phase data to determine the rotation angle of the Brγ-emitting gas. Our photocentre vectors show displacement from the central continuum region along an estimated PA of $\sim$18.8°, in a similar direction to the major axis PA of our best-fit geometric model (25.7$\pm$15.7°). Using our kinematic model, we derive a disk inclination of 19.2$\pm$1.7° for the inner gas disk around MWC147, which is consistent with our estimate for the inclination of the continuum-emitting disk (21.3$\pm$5.8°), derived from our geometric modelling of the continuum-emitting disk using AMBER/CLIMB visibility data. Our kinematic model of the gas disk has a major axis PA of 12.7$\pm$12.1°. Our best-fit major axis PA for the continuum-emitting disk is $25.7 \pm 15.7°$, which is consistent with the value determined by our best-fit kinematic model of the gas disk; this indicates that the Brγ emission traces Keplerian rotation in a gas disk, which lies in the same plane as the continuum-emitting disk. Our best disk PA (determined from our kinematic model of the gas disk) of 12.7°$\pm$12.1 gives the most robust estimate of the disk PA yet. Using AMBER differential phases and the long CHARA baselines we can significantly improve on the constraints from Lazareff et al. (2017), who estimated the major axis PA to be between 2° and 86°.

Using CRIRES spectroscopy we spectrally resolve the Brγ line from MWC147 with very high resolution, examining the fine structure and comparing the line profile with similar objects to learn more about the origin of the line emission. The shape and width of the Brγ line that we observe is very similar to the shape and width of the [OI] optical transitions observed by Bagnoli et al. (2010), suggesting that the two different species are present in a similar region of the disk. Our CRIRES data ($R = 100,000$) reveals that the line has a highly symmetric double-peaked structure with line wings that extend out to velocities of $\pm$200 km/s. This provides an interesting comparison point to our previous study of MWC297 (Hone et al., 2017), which has a similar disk geometry ($i = \approx 30°$) albeit around a more massive object. Typically, emission lines that arise from rotating disks exhibit double-peaked lines at moderate-to-high inclinations ($i \gtrsim 20°$) with the line

becoming single-peaked at inclinations below $\sim$20°.

In our 2017 paper, the CRIRES spectroscopy showed that MWC297 has a slightly asymmetric single-peaked Brγ line despite having an inclination of $\sim$23°, similar to the 24.8° inclination of MWC147. MWC297 has a wider Brγ line, which would be expected for a more inclined object; the line is single peaked, suggesting emission process of the Brγ line is different for MWC297 and MWC147 and that simple inclination effects cannot account for the differences in the line emission for the two objects. The asymmetric line profile of MWC297 was well reproduced by a more complex disk-wind model whereas, for MWC147, the strongly symmetrical observed Brγ line suggests that the emission arises in a rotating circumstellar disk or a region of a disk wind near the disk surface where material has not been significantly accelerated. The differences between these two scenarios are subtle (as discussed in Hone et al., 2017) and it is likely only possible to distinguish between the two cases if there is a more significant out-of-plane velocity component present in the velocity field traced by the Brγ emission. Such out-of-plane velocities are found in disk wind scenarios in the outer regions where material is more accelerated but also more diffuse, leading to a much smaller contribution to the overall line emission. We find that our model of a Keplerian disk is able to reproduce accurately the observed CRIRES Brγ spectrum (with a reduced χ^2 of 1.44). It is important to note that with the AMBER HR spectral resolution ($R = 12,000$) the differences between these two line shapes would be indistinguishable from each other, highlighting the importance of using HR spectroscopy in conjunction with spectro-interferometry when modelling the line emission from YSOs.

Since the Brγ line is in emission, we can infer that the optically thick gas is located in the disk plane without a bright emission source behind it, since we do not see any absorption. The emission component likely arises at higher scale height in the disk, where the gas becomes optically thin. Our interpretation of the Brγ emission originating from a gaseous accretion disk is only a good explanation if it can be demonstrated that accretion is able to heat the gas in the disk to temperatures of $\sim 6000 - 10000$K, hot enough to emit in the Brγ line. This question was addressed by Tambovtseva et al. (2016), who investigated whether a gaseous accretion disk could contribute to the Brγ emission in addition to a disk wind and magnetosphere. Six disk models were computed with varying sizes, temperatures, and accretion rates, and the outcome of this modelling demonstrates the viability of the gaseous accretion disk scenario that we employ for our study of MWC147.

8.6 Conclusions

In this paper we observed the inner regions of the protoplanetary disk around MWC147 with high spectral and spatial resolution. Using VLTI/AMBER and CHARA/CLIMB interferometry, we constructed a picture of the inner disk ranging from the morphology of the continuum-emitting disk to the kinematics traced by the gaseous line-emitting disk. We complemented our interferometric data with very high resolution VLT/CRIRES spectroscopy of the Brγ line. We computed a multi-component kinematic model of an active gaseous accretion disk that provides a good fit to our AMBER and CRIRES data.

Using VLTI and CHARA interferometry, we probed the K-band continuum of MWC147 with an angular resolution that is two times higher than ever before, detecting a very compact continuum-emitting disk; this corroborates the findings of previous works by Kraus et al. (2008b) and Lazareff et al. (2017). Our ring model for the continuum emission has a radius of 0.60 mas (0.39 au), which is $\sim$3.9 times more compact than the expected dust sublimation radius of 1.52 au. By observing the rotation traced by the Brγ emission from the gas disk and comparing the rotation axis with the observed PA of the continuum-emitting disk, we are able to place the strongest constraints yet on the orientation of the MWC147 system. Additionally, comparing the perceived Brγ (gas-disk) rotation angle with the continuum-disk PA suggests that the two disks lie in the same plane, which is consistent with the model of the disk in Keplerian rotation rather than a more complex kinematic scenario such as a disk wind.

We were able to achieve a very good fit to the double-peaked CRIRES Brγ spectrum and the differential interferometric observables from our AMBER data with a kinematic model of a gaseous disk in Keplerian rotation. We found that both the gas emission and continuum emission arise from a compact region inside the expected dust sublimation radius. The presence of this gas in the same location as the continuum emission strongly suggests that the compact K-band continuum emission arises from an active, viscous, gaseous accretion disk. These findings provide direct evidence for compact gaseous accretion disks as an explanation for the phenomena of undersized Herbig Be stars. In the future, other undersized Herbig Be stars should be studied with spectro-interferometry to determine whether line-emitting gas is co-located with the compact continuum emission similarly to MWC147. In order to more accurately measure the complex shape and morphology of the MWC147 K-band continuum emission, optical interferometry with baselines longer than $\sim$ 330m must be achieved to sample the second lobe of the visibility function. Additionally, with the introduction of the GRAVITY instrument at VLTI, a four-telescope spectro-interferometric beam combiner, the line emission around

MWC147 can be resolved with twice as many baselines simultaneously and possibly a *uv*-coverage sufficient for spectrally resolved image reconstruction can be achieved.

8.7 Outlook

In this study we find evidence of an optically thick gaseous disk around MWC147, interior to the dust sublimation radius. This discovery is an important piece of evidence to explain the phenomenon of "undersized" Herbig stars, objects similar to MWC147 where the K-band continuum is more compact that the expected dust-sublimation radius. Multiple explanations have been put forward to explain the compact continuum emission, including the presence of optically thick gas inside the dust sublimation radius. The results of our study suggest that this explanation is valid for the compact emission around MWC147, but more observations for different objects must be conducted to determine the validity of this explanation for other objects. Going forward, it is important to determine tests for each of the possible scenarios suggested in Section 2.4 in order to determine the nature of such "undersized" objects.

This study of MWC147 does not directly detect evidence of mass outflow from the inner region of the disk, in contrast to the previous study of MWC297 in Chapter 6. Multiple previous spectro-interometric studies of the Brγ emission from young stars have revealed similar Keplerian-like velocity fields (such as in Kraus et al., 2012b; Mendigutía et al., 2015; Kurosawa et al., 2016). However, the theoretical study by Tambovtseva et al. (2016) into the origin of Brγ emission suggested that the hot layers of an inner accretion disk are not able to contribute significantly to the Brγ emission, finding that the disk wind is the dominant contributor to the emission. Therefore, it is worth noting that the Keplerian velocity field is consistent with material at the base of the disk wind that has not been significantly accelerated, similar to the result from Kurosawa et al. (2016).

Chapter 9

Observing the jet-launching region of T Tauri stars

9.1 Introduction

Observations of protostellar jets in star forming regions have shown that the star formation process is associated as much with outflowing material as it is about infalling material on to young stars. Such jets are important to the star formation process for a variety of reasons. At small scales, they are critical to the removal of excess angular momentum from the circumstellar disk, permitting the accretion of material from the disk onto the star. At large scales, the protostellar jets impact the surrounding interstellar medium at high velocity, producing Herbig-Haro shocks which can influence the formation of new stars at macroscopic scales.

It is clear that these jets originate very close to the central protostar, which means that very high angular resolution is needed to discern between the different outflow launching mechanisms. The only way to observe with the angular resolution required to resolve the jet-launching region is with long-baseline interferometry. Spectrally dispersed interferometry is also essential to detect the jet launching mechanism, as it allows the observer to resolve line-emitting material at different velocities. Tambovtseva et al. (2016) recently proposed that in the case of Herbig Ae/Be stars, the Brγ emission line was primarily linked to mass ejection scenarios such as disk winds. Using spectro-interferometry to spatially and spectrally resolve Brγ emission is the perfect tool to observe the dynamic inner regions of protoplanetary disks, where the jet launching process takes place. Spectro-interferometry has previously been successfully employed to observe the dynamic environments in the inner regions of protoplanetary disks.

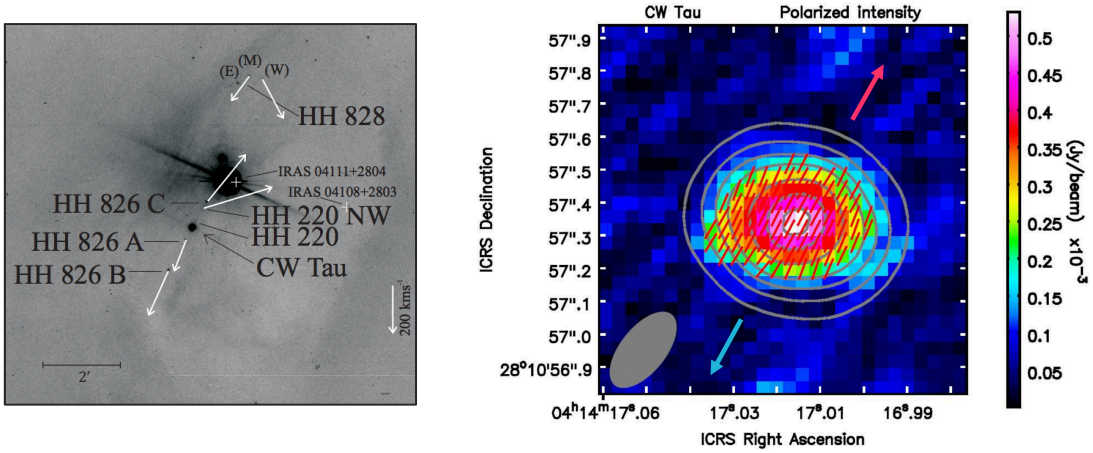

Figure 9.1.1: Left panel: Figure from McGroarty et al. (2007) showing the presence of the Herbig Haro objects associated with CW Tau (indicated with black arrows) as well as the directions of their proper motion (shown as white arrows.) Right panel: Figure from Bacciotti et al. (2018) showing the CW Tau disk as observed by ALMA (Band 9). The polarisation angle is shown by red bars, with the blue and red arrows indicating the respective directions of the blue- and red-shifted lobes of the jet.

So far, spectro-interferometric studies of young stellar objects have been confined to the higher-mass Herbig Ae/Be stars rather than the more typical, lower mass T Tauri stars. This is mainly due to the increased size and brightness of the Herbig stars, which makes them a more viable target for interferometry. In such studies, spectro-interferometric data has been combined effectively with kinematic modelling to reveal that the Brγ emission can exhibit Keplerian rotation (Kraus et al., 2012b; Mendigutía et al., 2015) and disk wind-like (Hone et al., 2017; Garcia Lopez et al., 2015; Caratti o Garatti et al., 2015) velocity fields. Whilst studies of these objects can provide interesting insights, they are rarely associated with the kind of collimated jets (such as in Figure 1.0.1) that cause Herbig-Haro shocks, meaning we are unable to further our understanding of how these jets are launched. The introduction of VLTI/GRAVITY represents a significant advancement in this field, allowing us to reach faint enough magnitudes to conduct a detailed study into the T Tauri stars which are responsible for the spectacular Herbig Haro shocks seen in star forming regions. Additionally, as a 4-telescope beam combiner GRAVITY can achieve twice the number of baselines as AMBER in the same amount of time, making it easier to achieve a good *uv*-coverage.

At a distance of $\sim$140pc the Taurus molecular cloud is one of the closest active star forming regions to Earth, containing a dense population of T Tauri stars and Herbig Haro objects, making it a perfect subject for this study. I selected interferometric science targets based on several factors: a stellar spectral type later than A, an association with a jet

or Herbig Haro knot(s), a K-band magnitude acceptable for study with GRAVITY ($\lesssim 9$) and a Brγ emission line. Several of these targets were the subject of a study by Beck et al. (2010) which examined the spatial extent of the Brγ emission from these objects. The study found that for those objects which did display extended Brγ emission, that emission was localised along a similar axis to nearby Herbig Haro knots, indicating a connection between the Brγ emission and T Tauri jets. Due to the constraints of observation, only half of the proposed targets were observed with GRAVITY and of those only two, CW Tau and DP Tau, had observable interferometric fringes. The work in this chapter focusses primarily on the data obtained for CW Tau, with the remaining DP Tau data possibly making up part of a future paper for this project.

CW Tau has been the subject of multiple unique scientific investigations in the past, giving us the ability to contextualise our GRAVITY observations without having to obtain additional data ourselves. The mass ($M_\star$) and radius ($R_\star$) of CW Tau have been measured as $1.21 M_\odot$ and $1.46 R_\odot$ respectively (Davies et al., 2014, and references within). The object was studied with ALMA by Bacciotti et al. (2018), who were able to place strong constraints on the orientation of the protoplanetary disk, with a measured inclination of $\sim 59^\circ$ and major axis PA of $60.7^\circ \pm 1.9^\circ$. Bacciotti et al. also used polarimetry to measure the polarization fraction of the CW Tau disk, finding likely cause of the polarisation to be the self-scattering of thermal dust emission. Multiple observations of CW Tau have shown the presence of a jet emerging towards the south-east of the disk along a PA of $\sim 150^\circ$ (Gomez de Castro, 1993; Hirth et al., 1994; Hartigan et al., 2004; McGroarty et al., 2007).

9.2 Observations and data reduction

In 2018 we used VLTI/GRAVITY's high spectral dispersion ($R = 4000$) mode to observe three T Tauri stars, each with closely associated jets or Herbig Haro objects. The observations took place on 2018-11-20, with GV Tau observed from 04:43, CW Tau observed from 04:59 and DP Tau observed from 06:07. For CW Tau and DP Tau we obtained moderate-to-good quality interference fringes, however GV Tau was at the very limit of the instrument's capabilities and only a small amount of poor-quality data was obtained. Wavelength dependent interferometric quantities were extracted from the raw data using the GRAVITY data reduction software (Lapeyrere et al., 2014). The DP Tau GRAVITY data does not show a strong Brγ feature and, as such, does not exhibit any change in squared visibility or differential phase as a function of wavelength. For this reason we fo-

cus primarily on the CW Tau data, which does exhibit a Brγ emission line and detectable differential phase data. The *uv*-coverage for CW Tau is shown in Figure 9.2.1 (due to the proximity of the objects and the small time difference between the observations the differences between each object's *uv*-coverage are negligible).
By targeting these T Tauri stars we tested the limitations of the GRAVITY instrument and as such we were forced to use the baseline configuratons made up from the 8.2m fixed UTs instead of the smaller 1.8m movable ATs. This means that whilst we achieve higher sensitivity we sacrifice the ability of our baselines to fill out the *uv*-coverage. As a result our *uv*-coverage spans a small range of angles, with the PA range from $\sim$65% of the angular coverage completely unsampled, making it extremely difficult to place strong constraints on the geometry of the disk.

9.3 Morphology of the disk

We fit our GRAVITY visibility data with a multi-component, two-dimensional brightness distribution. Our model is comprised of delta function to simulate the unresolved central star, a ring to simulate the inner rim of the dusty disk, and an extended Gaussian distribution to simulate the drop in visibility that is infered at short baselines. We fix the Gaussian component of our model to be face-on, as we do not have any baseline coverage that is sensitive to the morphology of the extended material. Additionally, because our *uv*-coverage is not comprehensive we adopt the inclination $i = 59°$ and position angle $\theta = 60.7 \pm 1.9°$ measured using ALMA by Bacciotti et al. (2018). We use our GRAVITY visibility data to constrain the size of the K-band continuum. The resulting best-fit parameters of our model are shown in Table 9.3.1. The best-fit ring radius of our model (0.56±0.20mas) corresponds to a physical distance of 0.074±0.03au or

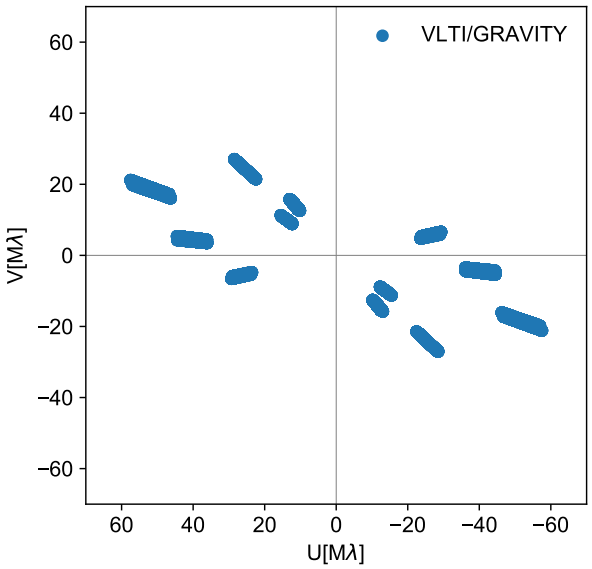

Figure 9.2.1: *uv*-coverage for our CW Tau obsvervations with VLTI/GRAVITY.

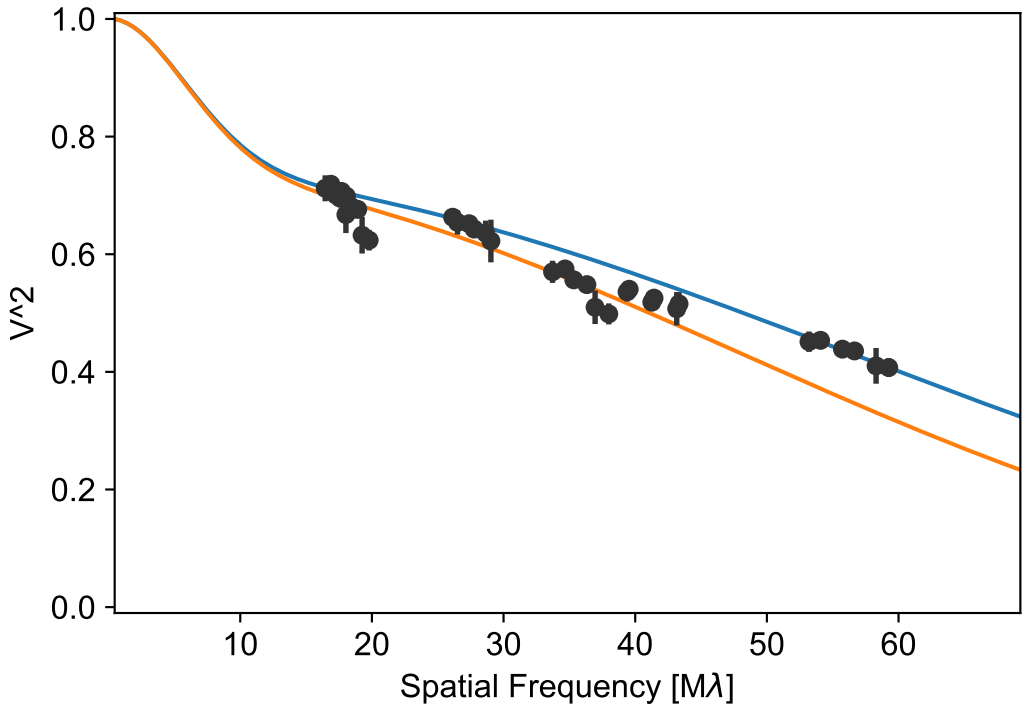

Figure 9.3.1: Visibility squared vs spatial frequency for CW Tau. GRAVITY data is shown as dark grey points. The major axis visibility of our best-fit geometric model is shown as a blue line, with the minor axis as an orange line.

$10.9 \pm 4.1 R_\star$. In Section 9.5 I analyse this result, discussing what it implies about the physical properties of the CW Tau system.

9.4 Kinematics traced by differential phase

As part of our high spectral dispersion GRAVITY data we obtained differential phases for six distinct baselines, with two object integrations for each baseline. By combining the integrations of similar baselines we improve the SNR of our differential phase data. Having done this, we detect a weak differential phase signal across the Brγ line, with the magnitude of the strongest data points being on the order of 1 or 2 degrees (see Figure 9.4.1). This is much smaller than the differential phases that we analyse previously in Chapters 6, 8 and 7. This is expected, considering that CW Tau has a much weaker emission line than the previous objects and, as a T Tauri star, has a much more compact inner disk region.

We use our differential phase data to calculate model-independent photocentre shifts,

Table 9.3.1: Parameters for our best-fit, multi-component geometric model. The parameter θ indicates the PA of the major axis of the disk. Uncertainty values are not obtained for the relative flux contributions of the different components of the model.

Parameter	Range	Best-fit value
$F_\star$	$0-100\%$	17%
$F_{\rm ring}$	$0-100\%$	65%
$F_{\rm Gauss}$	$0-100\%$	18%
R	$0.1-10$ mas	0.56 ± 0.20 mas
i	$0-90^\circ$	$51.3\pm5.6^\circ$
θ	$0-180^\circ$	$76.4\pm6.4^\circ$

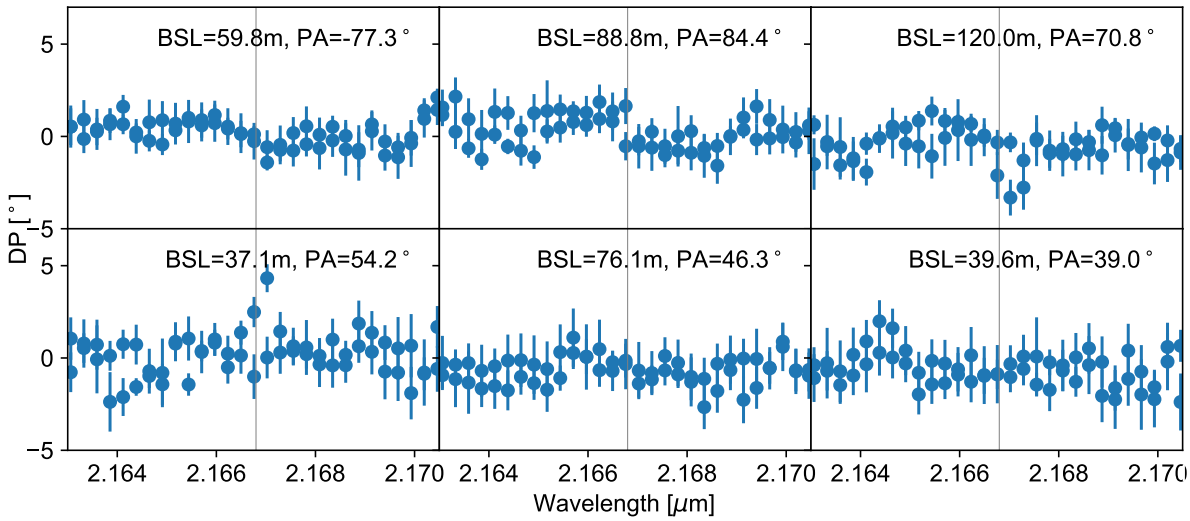

Figure 9.4.1: Differential phase vs wavelength for each of the baseline measurements taken of CW Tau. The two object integrations that were taken for each baseline are plotted over each other in each frame of the figure.

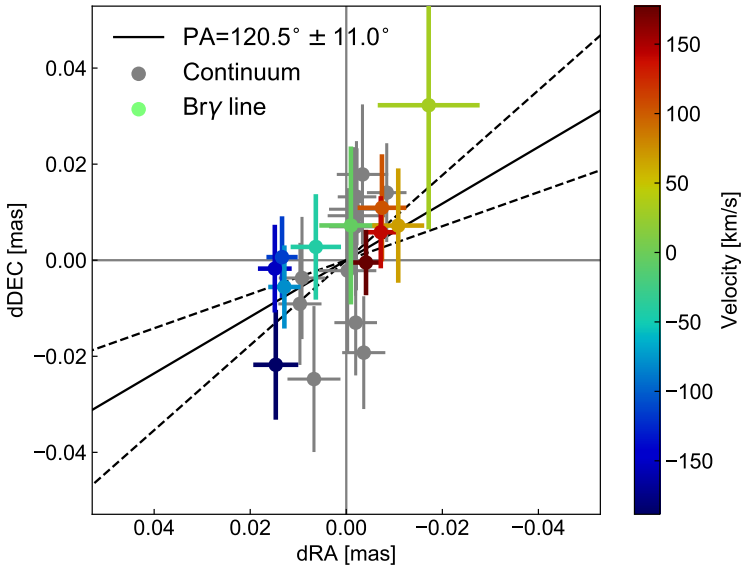

Figure 9.4.2: Photocentre displacement vectors across the Brγ line for CW Tau. The solid line represents the best-fit offset angle between red-and blue shifted vectors and the dashed line indicates the uncertainty of this values.

tracing the displacement of the centroid as a function of wavelength. To derive the wavelength-dependent photocentre vectors we adopt the same fitting method outlined in Hone et al. (2017) based on equation 6.5.1. Despite the weak differential phase signal, the photocentre displacement vectors reveal a clear displacement between red-shifted and blue-shifted material. We calculate the angle of this displacement by determing the angle of the displacement between corresponding velocity channels (i.e. -30kms^{-1} and 30kms^{-1}), taking the mean value as our displacement angle and the standard deviation as the uncertainty of this value. This reveals an offset angle between the red and blue shifted emission of 120.5°±11°, shown in Figure. 9.4.2. As we cannot be certain of the sign of the differential phase, this value could be flipped by 180°. The physical implications of the photocentre displacement profile is discussed in greater depth in Section 9.5.

9.5 Discussion

The GRAVITY visibility data is fitted using a ring model with a best-fit radius corresponding to a physical distance of 10.9±4.1 $R_\star$. For a T Tauri star such as CW Tau it is expected that the K-band continuum traces the irradiated inner rim of the dust disk (Muzerolle et al., 2003). Due to the lower luminosity of the central star, the dust rim is not located at the sublimation radius but where the disk is truncated by the magnetic field

(Königl, 1991). Taking the truncation radius equation from Bouvier et al. (2007b) and adapting it to solve for the stellar magnetic field strength $B_\star$, we obtain the relation:

$$B_\star = 0.0324 \times (R_\mathrm{T})^{\frac{7}{4}} \dot{M}^{-\frac{1}{2}} \left(2M_\star\right)^{-\frac{1}{4}} \left(\frac{R_\star}{2}\right)^{-\frac{5}{4}}, \tag{9.5.1}$$

where $B_\star$ is measured in kG, $R_\star$ is the stellar radius in $R_\odot$, R_T is the truncation radius in units of stellar radii, $M_\star$ is the stellar mass in $M_\odot$ and $\dot{M}$ is the accretion rate in $10^{-8} M_\odot \mathrm{yr}^{-1}$. For the truncation radius I use the best-fit ring radius of $10.9 R_\star$, determined with geometric modelling in Section 9.3. Additionally I adopt the CW Tau stellar parameter values from the work of Davies et al. (2014), namely the stellar mass $M_\star = 1.21 M_\odot$, the accretion rate $\dot{M} = 1.99 \times 10^{-8} M_\odot \mathrm{yr}^{-1}$ and the stellar radius $R_\star = 1.46 R_\odot$. These values correspond to a stellar magnetic field of 5.5kG.

The analysis of the photocentre displacement vectors yields a best-fit axis-of-motion PA of $120.5 \pm 11.0°$. We can compare this value with both the PA of the major-axis of the disk measured by ALMA (Bacciotti et al., 2018) along with the PA of the jet axis traced by the associated Herbig Haro flow (McGroarty et al., 2007). The axis of motion traced by the photocentre shifts closer to the minor axis of the ALMA disk (150.7°) than the major axis (60.7°), suggesting that the Brγ emission of CW Tau does not trace a rotational velocity field. The closeness of the photocentre PA to the minor-axis of the ALMA disk, as well as the PA of the associated Herbig Haro objects, is indicative that the line-emitting gas predominantly exhibits motion out of the disk plane. This could suggest a number of different physical mechanisms that could be traced by the Brγ emission, from the launching of a jet via any of the mechanisms discussed in Section 2.4.2, or even the motion of material being carried along magnetospheric accretion columns.

Without a more comprehensive *uv*-angle coverage, the true velocity field is impossible to directly measure from the differential phase, so it becomes important to take into account information about the location of the line emission relative to the K-band continuum. We do not detect a significant change in the visibility level across the line which suggests that the line emission originates from a similar region to the continuum. This is consistent with the hypothesis of magnetospheric accretion, or with an outflow being launched from the region where the stellar magnetic field interacts with the disk.

The GRAVITY visibilities for CW Tau show evidence of a sharp decrease ($\sim$15%) at short baselines ($\lesssim$15Mλ), indicating the presence of extended, K-band emitting material that we cannot place constraints on without shorter baselines in our *uv*-coverage. Anthonioz et al. (2015) detected similar features in a sample of T Tauri stars that were observed with PIONIER, suggesting that the visibility drop was caused by scattered light, in agreement

with models made by Pinte et al. (2008).

9.6 Outlook

From a simple first-look analysis of the CW Tau GRAVITY spectro-interferometry data it is clear that the kinematics traced in the Brγ line differ significantly from the previous studies of Herbig Ae/Be stars. However, there remains a substantial amount of analysis that can still be achieved for this data, particularly by modelling the differential quantities using a kinematic model. As part of a future publication using this data, I aim to construct a kinematic model using simmap, which can simultaneously recreate the spectrum, visibilities and differential phases that were observed with GRAVITY. Additionally, the Torus code (Harries, 2000) has been successfully used to model the line profiles of T Tauri stars and will provide an interesting comparison with the simmap model.
The CW Tau Brγ photocentre shifts trace motion that is closer to the jet axis than the disk major axis. In the studies of MWC297 from Chapter 6 and Chapter 7 we show that the perceived photocentre displacement angle is further from the disk major axis for a higher-velocity, more collimated region of the disk wind. This suggests that the velocity field traced by the Brγ emission from CW Tau is closer to that shown for the H-band Brackett series lines of MWC297 (Chapter 7) than for the Brγ emission of MWC297 (Chapter 6).

Chapter 10

Conclusions

The aim of my PhD was to discover more about the mechanism through which jets are launched from young stars by observing the jet-launching region with high angular and spectral resolution. I analysed spectro-interferometric data for several young stellar objects covering a wide range of stellar parameters. Each of the studies presented in this thesis revealed different velocity fields traced by the observed line emission. This diversity of velocities demonstrates that the way in which material in the jet-launching region is accelerated changes drastically as it approaches the central star. In this chapter I will discuss the results of each of the studies presented in this thesis and contextualise them within the larger framework of this thesis.

10.1 Observing the disk-wind launching region of MWC297

In this study I interpreted our specto-interferometric and spectroscopic data of the MWC297 Brγ emission, finding evidence of a disk wind with a poloidal velocity of $\lesssim$20kms^{-1}. This conclusion is supported through analysis of model-independent photocentre shifts, velocity-resolved image reconstruction and kinematic modelling. Due to the small poloidal velocity, the differences between the disk wind velocity field and the Keplerian velocity field are subtle, and could only be disentangled by combining multiple forms of analysis. In particular, the difference between the perceived axis of rotation traced by the photocentre shifts and the disk major axis was used to detect the presence of the poloidal velocity component. This analysis was used for later projects and a direct comparison was made during the study of MWC297 in a different wavelength regime (Chapter 7).
The presence of hydrogen gas hot enough to emit Brγ ($\sim$8000K) further away from the star than the K-band continuum ($\sim$2000K) in MWC297 is an interesting result, and sup-

ports the idea that the material accelerated in the disk wind is heated by ambipolar diffusion. The extended nature of the Brγ-emitting disk wind is a key comparison point for our later study of MWC297 in the H-band (discussed further in Section 10.2). MWC297 is the most massive object that is studied in this thesis and so provides an interesting comparison with the other objects studied in this thesis, particularly the lower-mass T Tauri star CW Tau. Whilst our study of MWC297 revealed detailed information about the launching of its disk wind, achieving spectro-interferometry for different spectral lines with different excitation energies could reveal more regions of the global disk-wind velocity field, allowing us to place stronger constraints on the physics of the outflow-launching process.

10.2 Multi-line spectro-interferometry of MWC297

In Chaper 7, I presented the results of medium spectral-dispersion interferometry for MWC297, spectrally and spatially resolving several of the Hydrogen Brackett series lines in the H-band. The photocentre displacement vectors for each of the observed Br-series lines do not show significant variation in the velocity field, but the velocity field of the H-band lines is significantly different from the Brγ velocity field from Chapter 6. The results of the kinematic modelling of the H-band Brackett series line suggests a poloidal velocity component of $\sim$220kms^{-1}.

The high-velocity outflow traced by the H-band lines originates from a much more compact region than the Brγ emission, even more compact than the continuum emission. The H-band lines have higher excitation energies than Brγ, so the gas in the compact, high-velocity region is hotter than the more extended, low-velocity gas. This investigation, coupled with the previous study in Chapter 6, provides unprecedented physical insight into the outflow launching region of a young stellar object. However, in order to learn more about the jet-launching process as a whole it is important to observe multiple different objects with different stellar properties.

10.3 Observing MWC147's compact Keplerian disk

In Chapter 8 I interpreted interferometric data of the Herbig Be star MWC147, finding evidence for the presence of a compact gaseous accretion disk inside of the expected dust sublimation radius. Whilst the spectro-interferometric data is consistent with a Keplerian velocity field, the quality and quantity of the data was insufficient for me to place strong constraints on the precise velocity field. Therefore, it is possible that the Brγ emission

traced the hot gas at the base of a disk wind, before it has been significantly accelerated in the poloidal direction.
MWC147, along with MWC297, is an example of an undersized Herbig Be star, with the VLTI and CHARA interferometry data indicating the presence of continuum emission much more compact than the expected dust-sublimation radius. Due to the presence of line-emitting hydrogen gas in the same location as the continuum emission, I suggest that the K-band continuum emission may be emitted by optically thick gas in a compact accretion disk orbiting the central young star. In this study the Brγ-emitting gas does not show a strong poloidal velocity component, but it is difficult to rule out a disk-wind scenario considering previous theoretical studies that suggest Brγ cannot be emitted solely from the accretion disk (Tambovtseva et al., 2016).

10.4 Observing the launching region of the CW Tau jet

The first three studies in this thesis (Chapters 6, 7 and 8) focused on intermediate-to-high mass Herbig Ae/Be stars, but that changed with our study of the T Tauri star CW Tau. The photocentre shifts traced by the Brγ emission indicate motion along an angle close to the jet axis, as opposed to the rotation-like velocity fields exhibited in previous chapters. The Brγ emission tracing a high-velocity outflow component shows a clear difference from the similar emission from MWC297 and MWC147. The velocity field traced by the H-band lines in Chapter 7 shows a similar high-poloidal velocity, but at much hotter temperatures.
CW Tau, as a T Tauri star, is less luminous and has a much stronger stellar magnetic field, which has been previously shown to be of vital importance to the outflow-launching process (Ferreira et al., 2006). The high poloidal velocities exhibited by the Brγ emission suggest that the material in the jet only becomes hot enough to emit in the Brγ line after it has been significantly accelerated out of the disk plane. Observing an object with a lower mass demonstrates the diversity of velocity fields in the jet-launching regions of young stars. By taking into account the different stellar properties of our target objects, we can gain insight into the physics of the jet-launching process and how it relates to the properties of the individual young star.

10.5 Final conclusions

Each of the studies presented in this thesis present a new insight into the jet-launching region of young stellar objects. By observing with high-spatial and high-spectral resolution we were able to place strong physical constraints on the morphology and velocity fields of the jet-launching regions in young stars. The discovery of compact, high-velocity jet-launching regions along with more extended, low-velocity winds provides observational eveidence that aligns with with published jet-launching theories (Romanova et al., 2005; Ferreira et al., 2006; Romanova et al., 2009), . The insights gained about the exctitation structure of protostellar jets from the studies in this thesis demonstrate the importance of observing the jet-launching region at different wavelengths. New interferometric instruments with the capability to observe in the J-band will unlock the ability to detect the presence of outflowing material with even higher velocities. Futher interferometric studies of the jet-launching region should focus on obtaining more spectral coverage at shorter wavelengths, more comprehensive *uv*-coverages for individual objects and the observation of large object samples, in order to find a physical description of how the physical processes in the inner disk vary as a function of stellar properties.

Chapter 11

Publications

A compact gaseous accretion disk in Keplerian rotation around MWC147; E. Hone, S. Kraus, C. L. Davies, A. Kreplin, J. D. Monnier, F. Baron, R. Millan-Gabet, K. Hofmann, D. Schertl, J. Sturmann, L. Sturmann, T. Ten Brummelaar and G. Weigelt; *2019, A&A 623, A38*

Imaging the disc rim and a moving close-in companion candidate in the pre-transitional disc of V1247 Orionis; M. Willson, S. Kraus, J. Kluska, J. D. Monnier, M. Cure, M. Sitko, A. Aarnio, M. J. Ireland, A. Rizzuto, E. Hone, A. Kreplin, S. Andrews, N. Calvet, C. Espaillat, M. Fukagawa, T. J. Harries, S. Hinkley, S. Kanaan, T. Muto and D. J. Wilner; *2019, A&A 621, A7*

Probing the origin of UX Ori-type variability in the YSO binary CO Ori with VLTI/GRAVITY; C. L. Davies, A. Kreplin, J. Kluska, E. Hone and S. Kraus; *2018, MNRAS 474, 5406*

VLTI Imaging of a High-Mass Protobinary System: Unveiling the Dynamical Processes in High-Mass Star Formation; S. Kraus, J. Kluska, A. Kreplin, M. Bate, T. J. Harries, K.-H. Hofmann, E. Hone, J. D. Monnier, G. Weigelt, A. Anugu, W. J. de Wit and M. Wittkowski *2017, The Messenger vol.170, 45*

Gas dynamics in the inner few AU around the Herbig B[e] star MWC297. Indications of a disk wind from kinematic modeling and velocity-resolved interferometric imaging; E. Hone, S. Kraus, A. Kreplin, K. Hofmann, G. Weigelt, J. Kluska and T. J. Harries; *2017, A&A 607, A17*

A High-mass Protobinary System with Spatially Resolved Circumstellar Accretion Disks and Circumbinary Disk; S. Kraus, J. Kluska, A. Kreplin, M. Bate, T. J. Harries, K.-H. Hofmann, E. Hone, J. D. Monnier, G. Weigelt, A. Anugu, W. J. de Wit and M. Wittkowski *2017, ApJ Letters 835:L5*

References

Acke, B., Verhoelst, T., van den Ancker, M. E., Deroo, P., Waelkens, C., Chesneau, O., Tatulli, E., Benisty, M., Puga, E., Waters, L. B. F. M., Verhoeff, A., and de Koter, A. (2008). MWC 297: a young high-mass star rotating at critical velocity. *A&A* , 485:209–221.

Adams, F. C., Lada, C. J., and Shu, F. H. (1987). Spectral Evolution of Young Stellar Objects. *ApJ* , 312:788.

Adams, F. C., Lada, C. J., and Shu, F. H. (1988). The Disks of T Tauri Stars with Flat Infrared Spectra. *ApJ* , 326:865.

ALMA Partnership, Brogan, C. L., Pérez, L. M., Hunter, T. R., et al. (2015). The 2014 ALMA Long Baseline Campaign: First Results from High Angular Resolution Observations toward the HL Tau Region. *ApJ* , 808:L3.

an der Marel, N., Williams, J. P., and Bruderer, S. (2018). Rings and Gaps in Protoplanetary Disks: Planets or Snowlines? *ApJ* , 867:L14.

Anderson, J. M., Li, Z.-Y., Krasnopolsky, R., and Blandford, R. D. (2003). Locating the Launching Region of T Tauri Winds: The Case of DG Tauri. *ApJ* , 590:L107–L110.

Anthonioz, F., Ménard, F., Pinte, C., Le Bouquin, J. B., Benisty, M., Thi, W. F., Absil, O., Duchêne, G., Augereau, J. C., Berger, J. P., Casassus, S., Duvert, G., Lazareff, B., Malbet, F., Millan-Gabet, R., Schreiber, M. R., Traub, W., and Zins, G. (2015). The VLTI/PIONIER near-infrared interferometric survey of southern T Tauri stars. I. First results. *A&A* , 574:A41.

Arsenault, R., Alonso, J., Bonnet, H., Brynnel, J., Delabre, B., Donaldson, R., Dupuy, C., Fedrigo, E., Farinato, J., and Hubin, N. N. (2003). MACAO-VLTI: An Adaptive Optics system for the ESO VLT interferometer. In Wizinowich, P. L. and Bonaccini,

D., editors, *Adaptive Optical System Technologies II*, volume 4839 of *Society of Photo-Optical Instrumentation Engineers (SPIE) Conference Series*, pages 174–185.

Aso, Y., Ohashi, N., Saigo, K., Koyamatsu, S., Aikawa, Y., Hayashi, M., Machida, M. N., Saito, M., Takakuwa, S., Tomida, K., Tomisaka, K., and Yen, H.-W. (2015). ALMA Observations of the Transition from Infall Motion to Keplerian Rotation around the Late-phase Protostar TMC-1A. *ApJ* , 812(1):27.

Audard, M., Ábrahám, P., Dunham, M. M., Green, J. D., Grosso, N., Hamaguchi, K., Kastner, J. H., Kóspál, Á., Lodato, G., Romanova, M. M., Skinner, S. L., Vorobyov, E. I., and Zhu, Z. (2014). Episodic Accretion in Young Stars. In Beuther, H., Klessen, R. S., Dullemond, C. P., and Henning, T., editors, *Protostars and Planets VI*, page 387.

Bacciotti, F., Girart, J. M., Padovani, M., Podio, L., Paladino, R., Testi, L., Bianchi, E., Galli, D., Codella, C., and Coffey, D. (2018). ALMA Observations of Polarized Emission toward the CW Tau and DG Tau Protoplanetary Disks: Constraints on Dust Grain Growth and Settling. *ApJ* , 865(2):L12.

Bacciotti, F., Mundt, R., Ray, T. P., Eislöffel, J., Solf, J., and Camezind, M. (2000). Hubble Space Telescope STIS Spectroscopy of the Optical Outflow from DG Tauri: Structure and Kinematics on Subarcsecond Scales. *ApJ* , 537:L49–L52.

Bagnoli, T., van Lieshout, R., Waters, L. B. F. M., van der Plas, G., Acke, B., van Winckel, H., Raskin, G., and Meerburg, P. D. (2010). An Inner Gaseous Disk Around the Herbig Be Star MWC 147. *ApJ* , 724:L5–L8.

Bailer-Jones, C. A. L., Rybizki, J., Fouesneau, M., Mantelet, G., and Andrae, R. (2018). Estimating Distance from Parallaxes. IV. Distances to 1.33 Billion Stars in Gaia Data Release 2. *AJ* , 156:58.

Balbus, S. A. and Hawley, J. F. (1991). A Powerful Local Shear Instability in Weakly Magnetized Disks. I. Linear Analysis. *ApJ* , 376:214.

Bans, A. and Königl, A. (2012). A Disk-wind Model for the Near-infrared Excess Emission in Protostars. *ApJ* , 758:100.

Barsony, M. (1994). Class 0 Protostars. In Clemens, D. P. and Barvainis, R., editors, *Clouds, Cores, and Low Mass Stars*, volume 65 of *Astronomical Society of the Pacific Conference Series*, page 197.

Bary, J. S., Matt, S. P., Skrutskie, M. F., Wilson, J. C., Peterson, D. E., and Nelson, M. J. (2008). Physical Conditions of Accreting Gas in T Tauri Star Systems. *ApJ* , 687(1):376–388.

Bastian, U., Finkenzeller, U., Jaschek, C., and Jaschek, M. (1983). The definition of T Tauri and Herbig Ae/Be stars. *A&A* , 126:438.

Bate, M. R., Bonnell, I. A., and Bromm, V. (2003). The formation of a star cluster: predicting the properties of stars and brown dwarfs. *MNRAS* , 339:577–599.

Beck, T. L., Bary, J. S., and McGregor, P. J. (2010). Spatially Extended Brackett Gamma Emission in the Environments of Young Stars. *ApJ* , 722(2):1360–1372.

Beckers, J. M. (1982). Differential speckle interferometry. *Optica Acta*, 29:361–362.

Beckwith, S. V. W., Sargent, A. I., Chini, R. S., and Guesten, R. (1990). A Survey for Circumstellar Disks around Young Stellar Objects. *AJ* , 99:924.

Benisty, M., Natta, A., Isella, A., Berger, J. P., Massi, F., Le Bouquin, J. B., Mérand, A., Duvert, G., Kraus, S., Malbet, F., Olofsson, J., Robbe-Dubois, S., Testi, L., Vannier, M., and Weigelt, G. (2010). Strong near-infrared emission in the sub-AU disk of the Herbig Ae star HD 163296: evidence of refractory dust? *A&A* , 511:A74.

Berger, J.-P. (2018). Protoplanetary environments at the astronomical unit scale: the contribution of long baseline interferometry. In *Optical and Infrared Interferometry and Imaging VI*, volume 10701, page 107011L. International Society for Optics and Photonics.

Berger, J. P. and Segransan, D. (2007). An introduction to visibility modeling. *New Astron. Rev.* , 51:576–582.

Bergin, E. A., Goldsmith, P. F., Snell, R. L., and Langer, W. D. (1997). The Chemical Composition and Evolution of Giant Molecular Cloud Cores: A Comparison of Observation and Theory. *ApJ* , 482:285–297.

Bik, A. and Thi, W. F. (2004). Evidence for an inner molecular disk around massive Young Stellar Objects. *A&A* , 427:L13–L16.

Bjerkeli, P., van der Wiel, M. H. D., Harsono, D., Ramsey, J. P., and Jørgensen, J. K. (2016). Resolved images of a protostellar outflow driven by an extended disk wind. *Nature* , 540(7633):406–409.

Blandford, R. D. and Payne, D. G. (1982). Hydromagnetic flows from accretion discs and the production of radio jets. *MNRAS* , 199:883–903.

Blitz, L. and Shu, F. H. (1980). The origin and lifetime of giant molecular cloud complexes. *ApJ* , 238:148–157.

Bodenheimer, P. (1995). Angular Momentum Evolution of Young Stars and Disks. *ARA&A* , 33:199–238.

Bonneau, D., Clausse, J.-M., Delfosse, X., Mourard, D., Cetre, S., Chelli, A., Cruzalèbes, P., Duvert, G., and Zins, G. (2006). SearchCal: a virtual observatory tool for searching calibrators in optical long baseline interferometry. I. The bright object case. *A&A* , 456:789–789.

Bonneau, D., Delfosse, X., Mourard, D., Lafrasse, S., Mella, G., Cetre, S., Clausse, J.-M., and Zins, G. (2011). SearchCal: a Virtual Observatory tool for searching calibrators in optical long-baseline interferometry. II. The faint-object case. *A&A* , 535:A53.

Bouret, J.-C., Martin, C., Deleuil, M., Simon, T., and Catala, C. (2003). Far UV spectroscopy of the circumstellar environment of the Herbig Be stars HD 259431 and HD 250550. *A&A* , 410:175–188.

Bouvier, J., Alencar, S. H. P., Harries, T. J., Johns- Krull, C. M., and Romanova, M. M. (2007a). Magnetospheric Accretion in Classical T Tauri Stars. In Reipurth, B., Jewitt, D., and Keil, K., editors, *Protostars and Planets V*, page 479.

Bouvier, J., Alencar, S. H. P., Harries, T. J., Johns-Krull, C. M., and Romanova, M. M. (2007b). Magnetospheric Accretion in Classical T Tauri Stars. *Protostars and Planets V*, pages 479–494.

Bouvier, J., Covino, E., Kovo, O., Martin, E. L., Matthews, J. M., Terranegra, L., and Beck, S. C. (1995). COYOTES II: SPOT properties and the origin of photometric period variations in T Tauri stars. *A&A* , 299:89.

Burrows, C. J., Stapelfeldt, K. R., Watson, A. M., Krist, J. E., Ballester, G. E., Clarke, J. T., Crisp, D., Gallagher, John S., I., Griffiths, R. E., Hester, J. J., Hoessel, J. G., Holtzman, J. A., Mould, J. R., Scowen, P. A., Trauger, J. T., and Westphal, J. A. (1996). Hubble Space Telescope Observations of the Disk and Jet of HH 30. *ApJ* , 473:437.

Caratti o Garatti, A., Tambovtseva, L. V., Garcia Lopez, R., Kraus, S., Schertl, D., fn, V. P., Weigelt, G., Hofmann, K.-H., Massi, F., Lagarde, S., Vannier, M., and Malbet, F. (2015). AMBER/VLTI high spectral resolution observations of the Brγ emitting region in HD 98922. A compact disc wind launched from the inner disc region. *A&A* , 582:A44.

Cesaroni, R., Galli, D., Lodato, G., Walmsley, C. M., and Zhang, Q. (2007). Disks Around Young O-B (Proto)Stars: Observations and Theory. In Reipurth, B., Jewitt, D., and Keil, K., editors, *Protostars and Planets V*, page 197.

Chelli, A., Utrera, O. H., and Duvert, G. (2009). Optimised data reduction for the AMBER/VLTI instrument. *A&A* , 502:705–709.

Chiang, E. I. and Goldreich, P. (1997). Spectral Energy Distributions of T Tauri Stars with Passive Circumstellar Disks. *ApJ* , 490:368–376.

Chiang, E. I., Joung, M. K., Creech-Eakman, M. J., Qi, C., Kessler, J. E., Blake, G. A., and van Dishoeck, E. F. (2001). Spectral Energy Distributions of Passive T Tauri and Herbig Ae Disks: Grain Mineralogy, Parameter Dependences, and Comparison with Infrared Space Observatory LWS Observations. *ApJ* , 547:1077–1089.

Cieza, L. A., Casassus, S., Pérez, S., Hales, A., Cárcamo, M., Ansdell, M., Avenhaus, H., Bayo, A., Bertrang, G. H. M., Cánovas, H., Christiaens, V., Dent, W., Ferrero, G., Gamen, R., Olofsson, J., Orcajo, S., Osses, A., Peña-Ramirez, K., Principe, D., Ruíz-Rodríguez, D., Schreiber, M. R., van der Plas, G., Williams, J. P., and Zurlo, A. (2017). ALMA Observations of Elias 2-24: A Protoplanetary Disk with Multiple Gaps in the Ophiuchus Molecular Cloud. *ApJ* , 851:L23.

Collier Cameron, A. and Campbell, C. G. (1993). Rotational evolution of magnetic T Tauri stars with accretion discs. *A&A* , 274:309.

Cooper, H. D. B., Lumsden, S. L., Oudmaijer, R. D., Hoare, M. G., Clarke, A. J., Urquhart, J. S., Mottram, J. C., Moore, T. J. T., and Davies, B. (2013). The RMS survey: near-IR spectroscopy of massive young stellar objects. *MNRAS* , 430:1125–1157.

Copernicus, N. (1519). *Commentariolus*. LIVRARIA DA FISICA.

Copernicus, N. (1543). *De Revolutionibus orbium coelestium*. Roskam's Boeken Verkoop Kantoor.

Davies, C. L., Gregory, S. G., and Greaves, J. S. (2014). Accretion discs as regulators of stellar angular momentum evolution in the ONC and Taurus-Auriga. *MNRAS* , 444(2):1157–1176.

Davies, C. L., Kraus, S., Harries, T. J., Kreplin, A., Monnier, J. D., Labdon, A., Kloppenborg, B., Acreman, D. M., Baron, F., Millan-Gabet, R., Sturmann, J., Sturmann, L., and Ten Brummelaar, T. A. (2018). Simultaneous Spectral Energy Distribution and Near-infrared Interferometry Modeling of HD 142666. *ApJ* , 866:23.

Dipierro, G., Price, D., Laibe, G., Hirsh, K., Cerioli, A., and Lodato, G. (2015). On planet formation in HL Tau. *MNRAS* , 453:L73–L77.

Dobbs, C. L. and Pringle, J. E. (2013). The exciting lives of giant molecular clouds. *MNRAS* , 432:653–667.

Dominik, C., Dullemond, C. P., Waters, L. B. F. M., and Walch, S. (2003). Understanding the spectra of isolated Herbig stars in the frame of a passive disk model. *A&A* , 398:607–619.

Dorn, R. J., Aller-Carpentier, E., Andolfato, L., Berger, J. P., Delplancke-Ströbele, F., Dupuy, C., Fedrigo, E., Gitton, P., Hubin, N., and Le Louarn, M. (2014). NAOMI — A New Adaptive Optics Module for Interferometry. *The Messenger*, 156:12–15.

Drew, J. E., Busfield, G., Hoare, M. G., Murdoch, K. A., Nixon, C. A., and Oudmaijer, R. D. (1997). MWC 297, B1.5Ve: a zero-age main-sequence star in the Aquila Rift. *MNRAS* , 286:538–548.

Dullemond, C. P., Dominik, C., and Natta, A. (2001). Passive Irradiated Circumstellar Disks with an Inner Hole. *ApJ* , 560:957–969.

Dullemond, C. P., Hollenbach, D., Kamp, I., and D'Alessio, P. (2007). Models of the Structure and Evolution of Protoplanetary Disks. In Reipurth, B., Jewitt, D., and Keil, K., editors, *Protostars and Planets V*, page 555.

Dullemond, C. P. and Monnier, J. D. (2010). The Inner Regions of Protoplanetary Disks. *Annual Review of Astronomy and Astrophysics*, 48:205–239.

Edwards, S., Hartigan, P., Ghandour, L., and Andrulis, C. (1994). Spectroscopic Evidence for Magnetospheric Accretion in Classical T Tauri Stars. *AJ* , 108:1056.

Edwards, S., Kwan, J., Fischer, W., Hillenbrand , L., Finn, K., Fedorenko, K., and Feng, W. a. (2013). Interpreting Near-infrared Hydrogen Line Ratios in T Tauri Stars. *ApJ* , 778(2):148.

Eisner, J. A., Hillenbrand, L. A., White, R. J., Akeson, R. L., and Sargent, A. I. (2005). Observations of T Tauri Disks at Sub-AU Radii: Implications for Magnetospheric Accretion and Planet Formation. *ApJ* , 623(2):952–966.

Eisner, J. A., Lane, B. F., Hillenbrand, L. A., Akeson, R. L., and Sargent, A. I. (2004). Resolved Inner Disks around Herbig Ae/Be Stars. *ApJ* , 613:1049–1071.

Eisner, J. A., Monnier, J. D., Woillez, J., Akeson, R. L., Millan-Gabet, R., Graham, J. R., Hillenbrand, L. A., Pott, J.-U., Ragland, S., and Wizinowich, P. (2010). Spatially and Spectrally Resolved Hydrogen Gas within 0.1 AU of T Tauri and Herbig Ae/Be Stars. *ApJ* , 718:774–794.

Enoch, M. L., Corder, S., Duchêne, G., Bock, D. C., Bolatto, A. D., Culverhouse, T. L., Kwon, W., Lamb, J. W., Leitch, E. M., Marrone, D. P., Muchovej, S. J., Pérez, L. M., Scott, S. L., Teuben, P. J., Wright, M. C. H., and Zauderer, B. A. (2011). Disk and Envelope Structure in Class 0 Protostars. II. High-resolution Millimeter Mapping of the Serpens Sample. *ApJS* , 195(2):21.

Event Horizon Telescope Collaboration, Akiyama, K., Alberdi, A., Alef, W., Asada, K., Azulay, R., Baczko, A.-K., Ball, D., Baloković, M., Barrett, J., and et al. (2019a). First M87 Event Horizon Telescope Results. I. The Shadow of the Supermassive Black Hole. *ApJ* , 875(1):L1.

Event Horizon Telescope Collaboration, Akiyama, K., Alberdi, A., Alef, W., Asada, K., Azulay, R., Baczko, A.-K., Ball, D., Baloković, M., Barrett, J., and et al. (2019b). First M87 Event Horizon Telescope Results. IV. Imaging the Central Supermassive Black Hole. *ApJ* , 875(1):L4.

Fairlamb, J. R., Oudmaijer, R. D., Mendigutía, I., Ilee, J. D., and van den Ancker, M. E. (2015). A spectroscopic survey of Herbig Ae/Be stars with X-shooter - I. Stellar parameters and accretion rates. *MNRAS* , 453:976–1001.

Fedele, D., Tazzari, M., Booth, R., Testi, L., Clarke, C. J., Pascucci, I., Kospal, A., Semenov, D., Bruderer, S., Henning, T., and Teague, R. (2018). ALMA continuum observations of the protoplanetary disk AS 209. Evidence of multiple gaps opened by a single planet. *A&A* , 610:A24.

Ferreira, J. (2007). *MHD Disc Winds*, page 181.

Ferreira, J., Dougados, C., and Cabrit, S. (2006). Which jet launching mechanism(s) in T Tauri stars? *A&A* , 453:785–796.

Filho, M. E., Garcia, P., Duvert, G., Duchene, G., Thiebaut, E., Young, J., Absil, O., Berger, J.-P., Beckert, T., Hoenig, S., Schertl, D., Weigelt, G., Testi, L., Tatuli, E., Borkowski, V., de Becker, M., Surdej, J., Aringer, B., Hron, J., Lebzelter, T., Chiavassa, A., Corradi, R., and Harries, T. (2008). Phase referencing in optical interferometry. In *Proc. SPIE* , volume 7013 of *Society of Photo-Optical Instrumentation Engineers (SPIE) Conference Series*, page 70131F.

Fizeau, H. (1854). Idee zur Messung der Umlaufsbewegung der Erde. *Annalen der Physik*, 168(8):652–655.

Frank, A., Ray, T. P., Cabrit, S., Hartigan, P., Arce, H. G., Bacciotti, F., Bally, J., Benisty, M., Eislöffel, J., Güdel, M., Lebedev, S., Nisini, B., and Raga, A. (2014). Jets and Outflows from Star to Cloud: Observations Confront Theory. In Beuther, H., Klessen, R. S., Dullemond, C. P., and Henning, T., editors, *Protostars and Planets VI*, page 451.

Gai, M., Menardi, S., Cesare, S., Bauvir, B., Bonino, D., Corcione, L., Dimmler, M., Massone, G., Reynaud, F., and Wallander, A. (2004). The VLTI fringe sensors: FINITO and PRIMA FSU. In Traub, W. A., editor, *New Frontiers in Stellar Interferometry*, volume 5491 of *Proc. SPIE* , page 528.

Gaia Collaboration, Brown, A. G. A., Vallenari, A., Prusti, T., de Bruijne, J. H. J., Babusiaux, C., and Bailer-Jones, C. A. L. (2018). Gaia Data Release 2. Summary of the contents and survey properties. *ArXiv e-prints*, page arXiv:1804.09365.

Gaia Collaboration, Prusti, T., de Bruijne, J. H. J., et al. (2016). The Gaia mission. *A&A* , 595:A1.

Galilei, G. (1610). *Sidereus nuncius, or, The Sidereal messenger*.

Gammie, C. F. and Johnson, B. M. (2005). Theoretical Studies of Gaseous Disk Evolution around Solar Mass Stars. In Krot, A. N., Scott, E. R. D., and Reipurth, B., editors, *Chondrites and the Protoplanetary Disk*, volume 341 of *Astronomical Society of the Pacific Conference Series*, page 145.

Garcia, P. J. V., Ferreira, J., Cabrit, S., and Binette, L. (2001). Atomic T Tauri disk winds heated by ambipolar diffusion. I. Thermal structure. *A&A* , 377:589–608.

Garcia Lopez, R., Tambovtseva, L. V., Schertl, D., Grinin, V. P., Hofmann, K.-H., Weigelt, G., and Caratti o Garatti, A. (2015). Probing the accretion-ejection connection with VLTI/AMBER. High spectral resolution observations of the Herbig Ae star HD 163296. *A&A* , 576:A84.

Ghosh, P. and Lamb, F. K. (1979). Accretion by rotating magnetic neutron stars. II. Radial and vertical structure of the transition zone in disk accretion. *ApJ* , 232:259–276.

Gillessen, S., Eisenhauer, F., Perrin, G., Brand ner, W., Straubmeier, C., Perraut, K., Amorim, A., Schöller, M., Araujo-Hauck, C., and Bartko, H. (2010). GRAVITY: a four-telescope beam combiner instrument for the VLTI. In *Optical and Infrared Interferometry II*, volume 7734 of *Society of Photo-Optical Instrumentation Engineers (SPIE) Conference Series*, page 77340Y.

Gomez de Castro, A. I. (1993). Subarcsecond Images of CW Tauri: Constraints on Disk Size and Jet Formation. *ApJ* , 412:L43.

Goodman, A. A., Benson, P. J., Fuller, G. A., and Myers, P. C. (1993). Dense Cores in Dark Clouds. VIII. Velocity Gradients. *ApJ* , 406:528.

Goodson, A. P., Böhm, K.-H., and Winglee, R. M. (1999). Jets from Accreting Magnetic Young Stellar Objects. I. Comparison of Observations and High-Resolution Simulation Results. *ApJ* , 524:142–158.

Goodson, A. P., Winglee, R. M., and Böhm, K.-H. (1997). Time-dependent Accretion by Magnetic Young Stellar Objects as a Launching Mechanism for Stellar Jets. *ApJ* , 489(1):199–209.

GRAVITY Collaboration, Abuter, R., Accardo, M., et al. (2017). First Light for GRAVITY: Phase Referencing Optical Interferometry for the Very Large Telescope Interferometer. *ArXiv e-prints*.

Gravity Collaboration, Abuter, R., Amorim, A., Anugu, N., Bauböck, M., Benisty, M., Berger, J. P., Blind, N., Bonnet, H., and Brandner, W. (2018a). Detection of the gravitational redshift in the orbit of the star S2 near the Galactic centre massive black hole. *A&A* , 615:L15.

Gravity Collaboration, Abuter, R., Amorim, A., Bauböck, M., Berger, J. P., Bonnet, H., Brand ner, W., Clénet, Y., Coudé Du Foresto, V., and de Zeeuw, P. T. (2018b). Detection

of orbital motions near the last stable circular orbit of the massive black hole SgrA*. *A&A* , 618:L10.

Grinin, V. P. and Tambovtseva, L. V. (2011). Disk wind in the radiation of young intermediate-mass stars. *Astronomy Reports*, 55(8):704–717.

Güdel, M., Eibensteiner, C., Dionatos, O., Audard, M., Forbrich, J., Kraus, S., Rab, C., Schneider, C., Skinner, S., and Vorobyov, E. (2018). ALMA detects a radial disk wind in DG Tauri. *A&A* , 620:L1.

Guenther, E. W., Lehmann, H., Emerson, J. P., and Staude, J. (1999). Measurements of magnetic field strength on T Tauri stars. *A&A* , 341:768–783.

Hager, W. W. and Zhang, H. (2005). A new conjugate gradient method with guaranteed descent and an efficient line search. *SIAM Journal on Optimization*, 16:170–192.

Hager, W. W. and Zhang, H. (2006). A new active set algorithm for box constrained optimization. *SIAM Journal on Optimization*, 17:526–557.

Harries, T. J. (2000). Synthetic line profiles of rotationally distorted hot-star winds. *MNRAS* , 315:722–734.

Hartigan, P., Edwards, S., and Pierson, R. (2004). Going Slitless: Images of Forbidden-Line Emission Regions of Classical T Tauri Stars Observed with the Hubble Space Telescope. *ApJ* , 609(1):261–276.

Hartmann, L., Calvet, N., Gullbring, E., and D'Alessio, P. (1998). Accretion and the Evolution of T Tauri Disks. *ApJ* , 495(1):385–400.

Heger, A., Fryer, C. L., Woosley, S. E., Langer, N., and Hartmann, D. H. (2003). How Massive Single Stars End Their Life. *ApJ* , 591(1):288–300.

Henning, T. and Semenov, D. (2013). Chemistry in Protoplanetary Disks. *Chemical Reviews*, 113:9016–9042.

Herbig, G. H. (1960). The Spectra of Be- and Ae-Type Stars Associated with Nebulosity. *The Astrophysical Journal Supplement Series*, 4:337.

Herbig, G. H. (1962). The properties and problems of T Tauri stars and related objects. *Advances in Astronomy and Astrophysics*, 1:47–103.

Herczeg, G. J. and Hillenbrand, L. A. (2008). UV Excess Measures of Accretion onto Young Very Low Mass Stars and Brown Dwarfs. *ApJ* , 681(1):594–625.

Hernández, J., Calvet, N., Briceño, C., Hartmann, L., and Berlind, P. (2004). Spectral Analysis and Classification of Herbig Ae/Be Stars. *AJ* , 127:1682–1701.

Hill, H. G. M. and Nuth, J. A. (2003). The Catalytic Potential of Cosmic Dust: Implications for Prebiotic Chemistry in the Solar Nebula and Other Protoplanetary Systems. *Astrobiology*, 3:291–304.

Hillenbrand, L. A., Strom, S. E., Vrba, F. J., and Keene, J. (1992). Herbig Ae/Be Stars: Intermediate-Mass Stars Surrounded by Massive Circumstellar Accretion Disks. *ApJ* , 397:613.

Hirth, G. A., Mundt, R., and Solf, J. (1994). Jet flows and disk winds from T Tauri stars: the case of CW Tau. *A&A* , 285:929–942.

Hofmann, K. H. and Weigelt, G. (1993). Iterative image reconstruction from the bispectrum. *A&A* , 278:328–339.

Hofmann, K.-H., Weigelt, G., and Schertl, D. (2014). An image reconstruction method (IRBis) for optical/infrared interferometry. *A&A* , 565:A48.

Högbom, J. A. (1974). Aperture Synthesis with a Non-Regular Distribution of Interferometer Baselines. *A&AS* , 15:417.

Hone, E., Kraus, S., Davies, C. L., Kreplin, A., Monnier, J. D., Baron, F., Millan-Gabet, R., Hofmann, K.-H., Schertl, D., Sturmann, J., Sturmann, L., Ten Brummelaar, T., and Weigelt, G. (2019). Compact gaseous accretion disk in Keplerian rotation around MWC 147. *A&A* , 623:A38.

Hone, E., Kraus, S., Kreplin, A., Hofmann, K.-H., Weigelt, G., Harries, T., and Kluska, J. (2017). Gas dynamics in the inner few AU around the Herbig B[e] star MWC297. Indications of a disk wind from kinematic modeling and velocity-resolved interferometric imaging. *A&A* , 607:A17.

Huang, J., Andrews, S. M., Cleeves, L. I., Öberg, K. I., Wilner, D. J., Bai, X., Birnstiel, T., Carpenter, J., Hughes, A. M., Isella, A., Pérez, L. M., Ricci, L., and Zhu, Z. (2018). CO and Dust Properties in the TW Hya Disk from High-resolution ALMA Observations. *ApJ* , 852:122.

Hueso, R. and Guillot, T. (2005). Evolution of protoplanetary disks: constraints from DM Tauri and GM Aurigae. *A&A* , 442:703–725.

Huygens, C. (1690). *Traité de la lumière, où sont expliquées les causes de ce qui luy arrive dans la réflexion, et dans la réfraction, et particulièrement dans l'étrange réfraction du cristal d'Islande: Avec un discours de la cause de la pesanteur*. Pierre van der Aa.

Ilee, J. D., Cyganowski, C. J., Nazari, P., Hunter, T. R., Brogan, C. L., Forgan, D. H., and Zhang, Q. (2016). G11.92-0.61 MM1: a Keplerian disc around a massive young proto-O star. *MNRAS* , 462:4386–4401.

Ilee, J. D., Fairlamb, J., Oudmaijer, R. D., Mendigutía, I., van den Ancker, M. E., Kraus, S., and Wheelwright, H. E. (2014). Investigating the inner discs of Herbig Ae/Be stars with CO bandhead and Brγ emission. *MNRAS* , 445:3723–3736.

Isella, A. and Natta, A. (2005). The shape of the inner rim in proto-planetary disks. *A&A* , 438:899–907.

Jeans, J. H. (1902). The Stability of a Spherical Nebula. *Philosophical Transactions of the Royal Society of London Series A*, 199:1–53.

Jennison, R. C. (1958). A phase sensitive interferometer technique for the measurement of the Fourier transforms of spatial brightness distributions of small angular extent. *MNRAS* , 118:276.

Johns-Krull, C. M., Valenti, J. A., and Koresko, C. (1999). Measuring the Magnetic Field on the Classical T Tauri Star BP Tauri. *ApJ* , 516:900–915.

Kaeufl, H.-U., Ballester, P., Biereichel, P., Delabre, B., Donaldson, R., Dorn, R., Fedrigo, E., Finger, G., Fischer, G., Franza, F., Gojak, D., Huster, G., Jung, Y., Lizon, J.-L., Mehrgan, L., Meyer, M., Moorwood, A., Pirard, J.-F., Paufique, J., Pozna, E., Siebenmorgen, R., Silber, A., Stegmeier, J., and Wegerer, S. (2004). CRIRES: a high-resolution infrared spectrograph for ESO's VLT. In Moorwood, A. F. M. and Iye, M., editors, *Ground-based Instrumentation for Astronomy*, volume 5492 of *Proc. SPIE* , pages 1218–1227.

Kawamura, A., Mizuno, Y., Minamidani, T., Filipović, M. D., Staveley-Smith, L., Kim, S., Mizuno, N., Onishi, T., Mizuno, A., and Fukui, Y. (2009). The Second Survey of the Molecular Clouds in the Large Magellanic Cloud by NANTEN. II. Star Formation. *The Astrophysical Journal Supplement Series*, 184:1–17.

Kenyon, S. J. and Hartmann, L. (1987). Spectral Energy Distributions of T Tauri Stars: Disk Flaring and Limits on Accretion. *ApJ* , 323:714.

Kirchhoff, G. (1860). Ueber das Verhältniss zwischen dem Emissionsvermögen und dem Absorptionsvermögen der Körper für Wärme und Licht. *Annalen der Physik*, 185(2):275–301.

Knigge, C., Woods, J. A., and Drew, J. E. (1995). The application of Monte Carlo methods to the synthesis of spectral line profiles arising from accretion disc winds. *MNRAS* , 273(2):225–248.

Königl, A. (1991). Disk Accretion onto Magnetic T Tauri Stars. *ApJ* , 370:L39.

Konigl, A. and Pudritz, R. E. (2000). Disk Winds and the Accretion-Outflow Connection. In Mannings, V., Boss, A. P., and Russell, S. S., editors, *Protostars and Planets IV*, page 759.

Koutoulaki, M., Garcia Lopez, R., Natta, A., Caratti o Garatti, A., Coffey, D., Sanchez-Bermudez, J., and Ray, T. P. (2018). The circumstellar environment of HD 50138 revealed by VLTI/AMBER at high angular resolution. *A&A* , 614:A90.

Kratter, K. and Lodato, G. (2016). Gravitational Instabilities in Circumstellar Disks. *Annual Review of Astronomy and Astrophysics*, 54:271–311.

Kraus, S. (2015). The interferometric view of Herbig Ae/Be stars. *Ap&SS* , 357:97.

Kraus, S., Calvet, N., Hartmann, L., Hofmann, K.-H., Kreplin, A., Monnier, J. D., and Weigelt, G. (2012a). On the Nature of the Herbig B[e] Star Binary System V921 Scorpii: Discovery of a Close Companion and Relation to the Large-scale Bipolar Nebula. *ApJ* , 746:L2.

Kraus, S., Calvet, N., Hartmann, L., Hofmann, K.-H., Kreplin, A., Monnier, J. D., and Weigelt, G. (2012b). On the Nature of the Herbig B[e] Star Binary System V921 Scorpii: Geometry and Kinematics of the Circumprimary Disk on Sub-AU Scales. *ApJ* , 752:11.

Kraus, S., Hofmann, K.-H., Benisty, M., Berger, J.-P., Chesneau, O., Isella, A., Malbet, F., Meilland, A., Nardetto, N., Natta, A., Preibisch, T., Schertl, D., Smith, M., Stee, P., Tatulli, E., Testi, L., and Weigelt, G. (2008a). The origin of hydrogen line emission for five Herbig Ae/Be stars spatially resolved by VLTI/AMBER spectro-interferometry. *A&A* , 489:1157–1173.

Kraus, S., Hofmann, K.-H., Menten, K. M., Schertl, D., Weigelt, G., Wyrowski, F., Meilland, A., Perraut, K., Petrov, R., Robbe-Dubois, S., Schilke, P., and Testi, L. (2010). A hot compact dust disk around a massive young stellar object. *Nature* , 466:339–342.

Kraus, S., Monnier, J. D., Che, X., Schaefer, G., Touhami, Y., Gies, D. R., Aufdenberg, J. P., Baron, F., Thureau, N., ten Brummelaar, T. A., McAlister, H. A., Turner, N. H., Sturmann, J., and Sturmann, L. (2012c). Gas Distribution, Kinematics, and Excitation Structure in the Disks around the Classical Be Stars β Canis Minoris and ζ Tauri. *ApJ* , 744:19.

Kraus, S., Preibisch, T., and Ohnaka, K. (2008b). Detection of an Inner Gaseous Component in a Herbig Be Star Accretion Disk: Near- and Mid-Infrared Spectrointerferometry and Radiative Transfer modeling of MWC 147. *ApJ* , 676:490–508.

Kreplin, A., Tambovtseva, L., Grinin, V., Kraus, S., Weigelt, G., and Wang, Y. (2018). On the Brγ line emission of the Herbig Ae/Be star MWC 120. *MNRAS* , 476(4):4520–4526.

Krumholz, M. R., Klein, R. I., McKee, C. F., Offner, S. S. R., and Cunningham, A. J. (2009). The Formation of Massive Star Systems by Accretion. *Science*, 323:754.

Kurosawa, R., Harries, T. J., and Symington, N. H. (2006). On the formation of Hα line emission around classical T Tauri stars. *MNRAS* , 370:580–596.

Kurosawa, R., Kreplin, A., Weigelt, G., Natta, A., Benisty, M., Isella, A., Tatulli, E., Massi, F., Testi, L., Kraus, S., Duvert, G., Petrov, R. G., and Stee, P. (2016). Probing the wind-launching regions of the Herbig Be star HD 58647 with high spectral resolution interferometry. *MNRAS* , 457:2236–2251.

Kwan, J. and Fischer, W. (2011). Origins of the H, He I and Ca II line emission in classical T Tauri stars. *MNRAS* , 411(4):2383–2425.

Lachaume, R. (2003). On marginally resolved objects in optical interferometry. *A&A* , 400:795–803.

Lada, C. J. (1987). Star formation: from OB associations to protostars. In Peimbert, M. and Jugaku, J., editors, *Star Forming Regions*, volume 115 of *IAU Symposium*, page 1.

Lamers, H. J. G. L. M. and Cassinelli, J. P. (1999). *Introduction to Stellar Winds*.

Lapeyrere, V., Kervella, P., Lacour, S., Azouaoui, N., Garcia-Dabo, C. E., Perrin, G., Eisenhauer, F., Perraut, K., Straubmeier, C., Amorim, A., and Brandner, W. (2014).

GRAVITY data reduction software. In *Optical and Infrared Interferometry IV*, volume 9146 of *Proc. SPIE* , page 91462D.

Larson, R. B. (1969). Numerical calculations of the dynamics of collapsing proto-star. *MNRAS* , 145:271.

Larson, R. B. (2003). The physics of star formation. *Reports on Progress in Physics*, 66:1651–1697.

Lazareff, B., Berger, J.-P., Kluska, J., Le Bouquin, J.-B., Benisty, M., Malbet, F., Koen, C., Pinte, C., Thi, W.-F., Absil, O., Baron, F., Delboulbé, A., Duvert, G., Isella, A., Jocou, L., Juhasz, A., Kraus, S., Lachaume, R., Ménard, F., Millan-Gabet, R., Monnier, J. D., Moulin, T., Perraut, K., Rochat, S., Soulez, F., Tallon, M., Thiébaut, E., Traub, W., and Zins, G. (2017). Structure of Herbig AeBe disks at the milliarcsecond scale . A statistical survey in the H band using PIONIER-VLTI. *A&A* , 599:A85.

Le Bouquin, J.-B., Absil, O., Benisty, M., Massi, F., Mérand, A., and Stefl, S. (2009). The spin-orbit alignment of the Fomalhaut planetary system probed by optical long baseline interferometry. *A&A* , 498:L41–L44.

Le Bouquin, J.-B., Bauvir, B., Haguenauer, P., Schöller, M., Rantakyrö, F., and Menardi, S. (2008). First result with AMBER+FINITO on the VLTI: the high-precision angular diameter of V3879 Sagittarii. *A&A* , 481:553–557.

Lee, C.-F., Ho, P. T. P., Li, Z.-Y., Hirano, N., Zhang, Q., and Shang, H. (2017). A rotating protostellar jet launched from the innermost disk of HH 212. *Nature Astronomy*, 1:0152.

Lee, H.-T., Chen, W. P., Zhang, Z.-W., and Hu, J.-Y. (2005). Triggered Star Formation in the Orion Bright-rimmed Clouds. *ApJ* , 624:808–820.

Li, D., Mariñas, N., and Telesco, C. M. (2014). The Immediate Environments of Two Herbig be Stars: MWC 1080 and HD 259431. *ApJ* , 796:74.

Long, F., Pinilla, P., Herczeg, G. J., et al. (2018). Gaps and Rings in an ALMA Survey of Disks in the Taurus Star-forming Region. *ApJ* , 869:17.

Lorén-Aguilar, P. and Bate, M. R. (2015). Toroidal vortices and the conglomeration of dust into rings in protoplanetary discs. *MNRAS* , 453:L78–L82.

Lynden-Bell, D. and Pringle, J. E. (1974). The evolution of viscous discs and the origin of the nebular variables. *MNRAS* , 168:603–637.

Maeder, A. and Meynet, G. (2000). Stellar evolution with rotation. VI. The Eddington and Omega -limits, the rotational mass loss for OB and LBV stars. *A&A* , 361:159–166.

Malbet, F., Benisty, M., de Wit, W.-J., et al. (2007). Disk and wind interaction in the young stellar object MWC 297 spatially resolved with AMBER/VLTI. *A&A* , 464:43–53.

McGroarty, F., Ray, T. P., and Froebrich, D. (2007). Proper motion studies of outflows from Classical T Tauri stars. *A&A* , 467(3):1197–1207.

Mendigutía, I., de Wit, W. J., Oudmaijer, R. D., Fairlamb, J. R., Carciofi, A. C., Ilee, J. D., and Vieira, R. G. (2015). High-resolution Br γ spectro-interferometry of the transitional Herbig Ae/Be star HD 100546: a Keplerian gaseous disc inside the inner rim. *MNRAS* , 453:2126–2132.

Mérand, A., Alberdid, A., Kluska, J., Tallon-Bosc, I., Tallon, M., Thiébaut, É., Sánchez-Bermudez, J., Schödel, R., Soulez, F., and Young, J. (2018). Optical interferometry image reconstruction contest VIII. In *Proc. SPIE* , volume 10701 of *Society of Photo-Optical Instrumentation Engineers (SPIE) Conference Series*, page 107011U.

Michelson, A. A. (1891). Measurement of Jupiter's Satellites by Interference. *Nature* , 45(1155):160–161.

Michelson, A. A. and Pease, F. G. (1921). Measurement of the Diameter of α Orionis with the Interferometer. *ApJ* , 53:249–259.

Millan-Gabet, R., Schloerb, F. P., and Traub, W. A. (2001). Spatially Resolved Circumstellar Structure of Herbig AE/BE Stars in the Near-Infrared. *ApJ* , 546:358–381.

Millour, F. (2014). Interferometry concepts. In *EAS Publications Series*, volume 69-70 of *EAS Publications Series*, pages 17–52.

Millour, F., Meilland, A., Chesneau, O., Stee, P., Kanaan, S., Petrov, R., Mourard, D., and Kraus, S. (2011). Imaging the spinning gas and dust in the disc around the supergiant A[e] star HD 62623. *A&A* , 526:A107.

Miura, R. E., Kohno, K., Tosaki, T., Espada, D., Hwang, N., Kuno, N., Okumura, S. K., Hirota, A., Muraoka, K., Onodera, S., Minamidani, T., Komugi, S., Nakanishi, K.,

Sawada, T., Kaneko, H., and Kawabe, R. (2012). Giant Molecular Cloud Evolutions in the Nearby Spiral Galaxy M33. *ApJ* , 761:37.

Monnier, J. D. (2003). Optical interferometry in astronomy. *Reports on Progress in Physics*, 66:789–857.

Monnier, J. D. and Millan-Gabet, R. (2002). On the Interferometric Sizes of Young Stellar Objects. *ApJ* , 579:694–698.

Monnier, J. D., Millan-Gabet, R., Billmeier, R., Akeson, R. L., Wallace, D., Berger, J.-P., Calvet, N., D'Alessio, P., Danchi, W. C., Hartmann, L., Hillenbrand, L. A., Kuchner, M., Rajagopal, J., Traub, W. A., Tuthill, P. G., Boden, A., Booth, A., Colavita, M., Gathright, J., Hrynevych, M., Le Mignant, D., Ligon, R., Neyman, C., Swain, M., Thompson, R., Vasisht, G., Wizinowich, P., Beichman, C., Beletic, J., Creech-Eakman, M., Koresko, C., Sargent, A., Shao, M., and van Belle, G. (2005). The Near-Infrared Size-Luminosity Relations for Herbig Ae/Be Disks. *ApJ* , 624:832–840.

Monnier, J. D., Zhao, M., Pedretti, E., Thureau, N., Ireland, M., Muirhead, P., Berger, J. P., Millan-Gabet, R., Van Belle, G., ten Brummelaar, T., McAlister, H., Ridgway, S., Turner, N., Sturmann, L., Sturmann, J., and Berger, D. (2007). Imaging the Surface of Altair. *Science*, 317(5836):342.

Morbidelli, A., Chambers, J., Lunine, J. I., Petit, J. M., Robert, F., Valsecchi, G. B., and Cyr, K. E. (2000). Source regions and time scales for the delivery of water to Earth. *Meteoritics and Planetary Science*, 35:1309–1320.

Mortimer, D. and Buscher, D. (2018). Prototyping fourier: the first generation near-infrared science beam combiner at the mroi. In *Optical and Infrared Interferometry and Imaging VI*, volume 10701, page 107010C. International Society for Optics and Photonics.

Mouschovias, T. C. (1977). A connection between the rate of rotation of interstellar clouds, magnetic fields, ambipolar diffusion, and the periods of binary stars. *ApJ* , 211:147–151.

Mouschovias, T. C. (1991). Magnetic Braking, Ambipolar Diffusion, Cloud Cores, and Star Formation: Natural Length Scales and Protostellar Masses. *ApJ* , 373:169.

Murillo, N. M., Lai, S.-P., Bruderer, S., Harsono, D., and van Dishoeck, E. F. (2013). A Keplerian disk around a Class 0 source: ALMA observations of VLA1623A. *A&A* , 560:A103.

Murray, N. (2011). Star Formation Efficiencies and Lifetimes of Giant Molecular Clouds in the Milky Way. *ApJ* , 729:133.

Muzerolle, J., Calvet, N., and Hartmann, L. (2001). Emission-Line Diagnostics of T Tauri Magnetospheric Accretion. II. Improved Model Tests and Insights into Accretion Physics. *ApJ* , 550:944–961.

Muzerolle, J., Calvet, N., Hartmann, L., and D'Alessio, P. (2003). Unveiling the Inner Disk Structure of T Tauri Stars. *ApJ* , 597(2):L149–L152.

Muzerolle, J., D'Alessio, P., Calvet, N., and Hartmann, L. (2004). Magnetospheres and Disk Accretion in Herbig Ae/Be Stars. *ApJ* , 617:406–417.

Muzerolle, J., Hartmann, L., and Calvet, N. (1998a). A Brgamma Probe of Disk Accretion in T Tauri Stars and Embedded Young Stellar Objects. *AJ* , 116(6):2965–2974.

Muzerolle, J., Hartmann, L., and Calvet, N. (1998b). Emission-Line Diagnostics of T Tauri Magnetospheric Accretion. I. Line Profile Observations. *AJ* , 116(1):455–468.

Myers, P. C. and Ladd, E. F. (1993). Bolometric temperatures of young stellar objects. *ApJ* , 413:L47–L50.

Najita, J., Carr, J. S., and Mathieu, R. D. (2003). Gas in the Terrestrial Planet Region of Disks: CO Fundamental Emission from T Tauri Stars. *ApJ* , 589:931–952.

Nakamoto, T. and Nakagawa, Y. (1994). Formation, Early Evolution, and Gravitational Stability of Protoplanetary Disks. *ApJ* , 421:640.

Natta, A., Prusti, T., Neri, R., Wooden, D., Grinin, V. P., and Mannings, V. (2001). A reconsideration of disk properties in Herbig Ae stars. *A&A* , 371:186–197.

Natta, A., Testi, L., and Randich, S. (2006). Accretion in the ρ-Ophiuchi pre-main sequence stars. *A&A* , 452(1):245–252.

Ostriker, E. C. and Shu, F. H. (1995). Magnetocentrifugally Driven Flows from Young Stars and Disks. IV. The Accretion Funnel and Dead Zone. *ApJ* , 447:813.

Padgett, D. L., Brandner, W., Stapelfeldt, K. R., Strom, S. E., Terebey, S., and Koerner, D. (1999). HUBBLE SPACE TELESCOPE/NICMOS Imaging of Disks and Envelopes around Very Young Stars. *AJ* , 117:1490–1504.

Petrov, R. G., Malbet, F., Weigelt, G., et al. (2007). AMBER, the near-infrared spectro-interferometric three-telescope VLTI instrument. *A&A* , 464:1–12.

Pinte, C., Ménard, F., Berger, J. P., Benisty, M., and Malbet, F. (2008). The Inner Radius of T Tauri Disks Estimated from Near-Infrared Interferometry: The Importance of Scattered Light. *ApJ* , 673(1):L63.

Pinte, C., Price, D. J., Ménard, F., Duchêne, G., Dent, W. R. F., Hill, T., de Gregorio-Monsalvo, I., Hales, A., and Mentiplay, D. (2018). Kinematic Evidence for an Embedded Protoplanet in a Circumstellar Disk. *ApJ* , 860(1):L13.

Pinte, C., van der Plas, G., Menard, F., Price, D. J., Christiaens, V., Hill, T., Mentiplay, D., Ginski, C., Choquet, E., Boehler, Y., Duchene, G., Perez, S., and Casassus, S. (2019). Kinematic detection of a planet carving a gap in a protoplanetary disc. *arXiv e-prints*, page arXiv:1907.02538.

Polomski, E. F., Telesco, C. M., Piña, R., and Schulz, B. (2002). The Dusty Circumstellar Environments of Ae/Be Protoplanetary Disk Candidates. *AJ* , 124:2207–2223.

Pudritz, R. E. and Norman, C. A. (1983). Centrifugally driven winds from contracting molecular disks. *ApJ* , 274:677–697.

Pudritz, R. E. and Norman, C. A. (1986). Bipolar Hydromagnetic Winds from Disks around Protostellar Objects. *ApJ* , 301:571.

Pudritz, R. E., Ouyed, R., Fendt, C., and Brandenburg, A. (2007). Disk Winds, Jets, and Outflows: Theoretical and Computational Foundations. In Reipurth, B., Jewitt, D., and Keil, K., editors, *Protostars and Planets V*, page 277.

Reipurth, B. (1997). Herbig-Haro jets and their role in star formation. *The Messenger*, 88:20–26.

Renard, S., Thiébaut, E., and Malbet, F. (2011). Image reconstruction in optical interferometry: benchmarking the regularization. *A&A* , 533:A64.

Romanova, M. M. and Owocki, S. P. (2015). Accretion, Outflows, and Winds of Magnetized Stars. *Space Sci. Rev.* , 191(1-4):339–389.

Romanova, M. M., Ustyugova, G. V., Koldoba, A. V., and Lovelace, R. V. E. (2004). Three-dimensional Simulations of Disk Accretion to an Inclined Dipole. II. Hot Spots and Variability. *ApJ* , 610(2):920–932.

Romanova, M. M., Ustyugova, G. V., Koldoba, A. V., and Lovelace, R. V. E. (2005). Propeller-driven Outflows and Disk Oscillations. *ApJ* , 635(2):L165–L168.

Romanova, M. M., Ustyugova, G. V., Koldoba, A. V., and Lovelace, R. V. E. (2009). Launching of conical winds and axial jets from the disc-magnetosphere boundary: axisymmetric and 3D simulations. *MNRAS* , 399(4):1802–1828.

Sanchez-Bermudez, J., Millour, F., Baron, F., van Boekel, R., Bourgès, L., Duvert, G., Garcia, P. J. V., Gomes, N., Hofmann, K.-H., Henning, T., Isbell, J. W., Lopez, B., Matter, A., Pott, J. U., Schertl, D., Thiébaut, E., Weigelt, G., and Young, J. (2018). Why chromatic imaging matters. *Experimental Astronomy*, 46(3):457–473.

Sauty, C. and Tsinganos, K. (1994). Nonradial and nonpolytropic astrophysical outflows III. A criterion for the transition from jets to winds. *A&A* , 287:893–926.

Scally, A. and Clarke, C. (2001). Destruction of protoplanetary discs in the Orion Nebula Cluster. *MNRAS* , 325:449–456.

Shu, F., Najita, J., Ostriker, E., Wilkin, F., Ruden, S., and Lizano, S. (1994a). Magnetocentrifugally driven flows from young stars and disks. 1: A generalized model. *ApJ* , 429:781–796.

Shu, F., Najita, J., Ostriker, E., Wilkin, F., Ruden, S., and Lizano, S. (1994b). Magnetocentrifugally Driven Flows from Young Stars and Disks. I. A Generalized Model. *ApJ* , 429:781.

Shu, F. H., Adams, F. C., and Lizano, S. (1987). Star formation in molecular clouds - Observation and theory. *ARA&A* , 25:23–81.

Smith, K., Pestalozzi, M., Güdel, M., Conway, J., and Benz, A. O. (2003). VLBI observations of T Tauri South. *A&A* , 406:957–967.

Smith, N., Bally, J., Licht, D., and Walawender, J. (2005). New Silhouette Disks with Reflection Nebulae and Outflows in the Orion Nebula and M43. *AJ* , 129:382–392.

Tambovtseva, L. V., Grinin, V. P., and Weigelt, G. (2014). Hydrogen lines as a diagnostic tool for studying multicomponent emitting regions in hot young stars: magnetosphere, X-wind, and disk wind. *A&A* , 562:A104.

Tambovtseva, L. V., Grinin, V. P., and Weigelt, G. (2016). Brackett γ radiation from the inner gaseous accretion disk, magnetosphere, and disk wind region of Herbig AeBe stars. *A&A* , 590:A97.

Tarantola, A. (1987). *Inverse problem theory. Methods for data fitting and model parameter estimation*.

Tarantola, A. and Valette, B. (1982). Generalized Nonlinear Inverse Problems Solved Using the Least Squares Criterion (Paper 1R1855). *Reviews of Geophysics and Space Physics*, 20:219.

Tatulli, E., Millour, F., Chelli, A., et al. (2007). Interferometric data reduction with AMBER/VLTI. Principle, estimators, and illustration. *A&A* , 464:29–42.

ten Brummelaar, T. A., McAlister, H. A., Ridgway, S. T., Bagnuolo, Jr., W. G., Turner, N. H., Sturmann, L., Sturmann, J., Berger, D. H., Ogden, C. E., Cadman, R., Hartkopf, W. I., Hopper, C. H., and Shure, M. A. (2005). First Results from the CHARA Array. II. A Description of the Instrument. *ApJ* , 628:453–465.

ten Brummelaar, T. A., Sturmann, J., Ridgway, S. T., Sturmann, L., Turner, N. H., McAlister, H. A., Farrington, C. D., Beckmann, U., Weigelt, G., and Shure, M. (2013). The Classic/climb Beam Combiner at the CHARA Array. *Journal of Astronomical Instrumentation*, 2:1340004.

Terebey, S., Shu, F. H., and Cassen, P. (1984). The collapse of the cores of slowly rotating isothermal clouds. *ApJ* , 286:529–551.

Thiébaut, É. and Young, J. (2017). Principles of image reconstruction in optical interferometry: tutorial. *Journal of the Optical Society of America A*, 34(6):904.

Thompson, A. R., Moran, J. M., and Swenson, G. W. (2017). *Van Cittert–Zernike Theorem, Spatial Coherence, and Scattering*, pages 767–786. Springer International Publishing, Cham.

Titterington, D. M. (1985). General Structure of Regularization Procedures in Image Reconstruction. *A&A* , 144:381.

Turner, N. J., Benisty, M., Dullemond, C. P., and Hirose, S. (2014). Herbig Stars' Near-infrared Excess: An Origin in the Protostellar Disk's Magnetically Supported Atmosphere. *ApJ* , 780:42.

van Cittert, P. H. (1934). Die Wahrscheinliche Schwingungsverteilung in Einer von Einer Lichtquelle Direkt Oder Mittels Einer Linse Beleuchteten Ebene. *Physica*, 1:201–210.

van den Ancker, M. E., Blondel, P. F. C., Tjin A Djie, H. R. E., Grankin, K. N., Ezhkova, O. V., Shevchenko, V. S., Guenther, E., and Acke, B. (2004). The stellar composition of the star formation region CMa R1 - III. A new outburst of the Be star component in Z CMa. *MNRAS* , 349:1516–1536.

van der Marel, N., van Dishoeck, E. F., Bruderer, S., Birnstiel, T., Pinilla, P., Dullemond, C. P., van Kempen, T. A., Schmalzl, M., Brown, J. M., Herczeg, G. J., Mathews, G. S., and Geers, V. (2013). A Major Asymmetric Dust Trap in a Transition Disk. *Science*, 340(6137):1199–1202.

Watson, D. M., Kemper, F., Calvet, N., Keller, L. D., Furlan, E., Hartmann, L., Forrest, W. J., Chen, C. H., Uchida, K. I., Green, J. D., Sargent, B., Sloan, G. C., Herter, T. L., Brandl, B. R., Houck, J. R., Najita, J., D'Alessio, P., Myers, P. C., Barry, D. J., Hall, P., and Morris, P. W. (2004). Mid-infrared Spectra of Class I Protostars in Taurus. *ApJS* , 154(1):391–395.

Weigelt, G., Grinin, V. P., Groh, J. H., Hofmann, K.-H., Kraus, S., Miroshnichenko, A. S., Schertl, D., Tambovtseva, L. V., Benisty, M., Driebe, T., Lagarde, S., Malbet, F., Meilland, A., Petrov, R., and Tatulli, E. (2011). VLTI/AMBER spectro-interferometry of the Herbig Be star MWC 297 with spectral resolution 12 000. *A&A* , 527:A103.

Weigelt, G., Hofmann, K.-H., Schertl, D., Clementel, N., Corcoran, M. F., Damineli, A., de Wit, W.-J., Grellmann, R., Groh, J., Guieu, S., Gull, T., Heininger, M., Hillier, D. J., Hummel, C. A., Kraus, S., Madura, T., Mehner, A., Mérand, A., Millour, F., Moffat, A. F. J., Ohnaka, K., Patru, F., Petrov, R. G., Rengaswamy, S., Richardson, N. D., Rivinius, T., Schöller, M., Teodoro, M., and Wittkowski, M. (2016). VLTI-AMBER velocity-resolved aperture-synthesis imaging of η Carinae with a spectral resolution of 12 000. Studies of the primary star wind and innermost wind-wind collision zone. *A&A* , 594:A106.

Weigelt, G., Kraus, S., Driebe, T., et al. (2007). Near-infrared interferometry of η Carinae with spectral resolutions of 1 500 and 12 000 using AMBER/VLTI. *A&A* , 464:87–106.

Wilking, B. A. (1989). The Formation of Low-Mass Stars. *PASP* , 101:229.

Williams, J. P. and Cieza, L. A. (2011). Protoplanetary Disks and Their Evolution. *Annual Review of Astronomy and Astrophysics*, 49:67–117.

Wolfire, M. G. and Cassinelli, J. P. (1987). Conditions for the Formation of Massive Stars. *ApJ* , 319:850.

Yen, H.-W., Takakuwa, S., Ohashi, N., Aikawa, Y., Aso, Y., Koyamatsu, S., Machida, M. N., Saigo, K., Saito, M., Tomida, K., and Tomisaka, K. (2014). ALMA Observations of Infalling Flows toward the Keplerian Disk around the Class I Protostar L1489 IRS. *ApJ* , 793(1):1.

Yorke, H. W., Bodenheimer, P., and Laughlin, G. (1995). The Formation of Protostellar Disks. II. Disks around Intermediate-Mass Stars. *ApJ* , 443:199.

Zernike, F. (1938). The concept of degree of coherence and its application to optical problems. *Physica*, 5(8):785–795.

Zhu, Z., Dong, R., Stone, J. M., and Rafikov, R. R. (2015). The Structure of Spiral Shocks Excited by Planetary-mass Companions. *ApJ* , 813:88.